

Copyright
by
Kirk William Madison
1998

QUANTUM TRANSPORT IN OPTICAL LATTICES

by

KIRK WILLIAM MADISON, B.S.E.

DISSERTATION

Presented to the Faculty of the Graduate School of

The University of Texas at Austin

in Partial Fulfillment

of the Requirements

for the Degree of

DOCTOR OF PHILOSOPHY

THE UNIVERSITY OF TEXAS AT AUSTIN

August 1998

QUANTUM TRANSPORT IN OPTICAL LATTICES

APPROVED BY
DISSERTATION COMMITTEE:

Supervisor: Markus Bunn
Daniel J. Hein
Robert E. Heath
Klemens Klenopp
L. J. Lind

To Mother and Father, who give me faith in myself and humanity, and to my
daughter Ana Eloísa, with whom I hope to share this faith.

Acknowledgements

I am deeply grateful to my advisor, Mark G. Raizen, for his guidance and support throughout my graduate career. Mark is not only an excellent scientist with a truly creative passion for physics but also a compassionate human with a genuine concern for the well being of his students. Mark's balanced leadership is perhaps equaled only by his ability to "make it rain" when the experiments run dry.

My four year sojourn in the Raizen Lab began in the company of Fred Moore, John Robinson, Pat Morrow, Cyrus Bharucha, and Bruce Klappauf. Fred and John provided solid guidance, a wealth of knowledge on experimental techniques, and an intellectually challenging atmosphere which were crucial to my early development. Pat and Cyrus provided the finer details in my initial training acting as patient sources for the relevant information and for general discussion. It was during this time that the group's first experiments in quantum chaos were being done, and I was fortunate to be a part of some of that research [1]. Bruce and I entered Mark's lab at the same time, and shared that initial baptism by fire. Since that time, Bruce, a persistent experimentalist and dancing machine, has continued to contribute to both my intellectual and personal development. For his friendship, I am grateful.

Also, I am especially grateful to Cyrus with whom I had the pleasure of realizing our first experiments in quantum transport [2, 3, 4]. Cyrus was a terrific partner in the laboratory, and I thoroughly enjoyed the tight camaraderie in our teamwork. In addition, Cyrus honed my analytic skills with a

never-ending stream of fascinating physics problems and bizarre brainteasers.

Steve Wilkinson, a postdoctoral fellow, arrived in the spring of 1996 and joined the transport experiments with enthusiasm and military savvy. At the same time, we recruited Daniel Steck, an excellent student and a great asset to the lab. Dan's astonishing efficiency, mathematical prowess, and willingness to help have been invaluable to us all. In the summer of 1996, Martin Fischer arrived and began working with me on the sodium experiment. I found Martin to be an excellent teammate, and together we realized the experiments on band spectroscopy and band collapse [5, 6]. In addition to offering his experimental intuition, honed by more than three years of prior graduate research, Martin also employed his penchant and skill for numerical simulations, providing the research with valuable, independent analyses.

The lab as a whole has benefited greatly from collaborations with Bala Sundaram and Qian Niu, who have provided strong theoretical support concurrent with much of our experimental work. Qian's graduate students Georgios Georgakis and Roberto Diener have also contributed to the work by performing numerical analyses. In particular, I would like to thank Qian for many fruitful discussions.

Windell Oskay was recruited in the spring of 1997 and since then has cultivated in the lab a renewed curiosity and aesthetic vision for our research. His wit and candor provide spice to our lab life. I would also like to acknowledge Valery Milner, a new postdoc who only recently arrived from Israel. Valery has aided me with this dissertation through a number of discussions. Also, he has proven himself to be a fine addition to the Raizen Lab, both in mind and in spirit.

For their help in the final editing of this dissertation, I am indebted to

Mark, Cyrus, Dan and Martin. Their vigilant attention to detail and careful corrections have greatly improved this document.

Finally, I would like to acknowledge fellowship support from the Office of Naval Research for my first three years of graduate study.

QUANTUM TRANSPORT IN OPTICAL LATTICES

Publication No. _____

Kirk William Madison, Ph.D.
The University of Texas at Austin, 1998

Supervisor: Mark G. Raizen

Recent advances in the field of cooling, trapping, and manipulation of atoms with laser light have created powerful experimental techniques for the study of fundamental quantum mechanics. Among the many fields of research made available by these advances are the study of quantum chaos and the study of quantum transport. This dissertation describes our experimental studies of quantum transport in optical lattices.

The study of quantum transport has traditionally been done in the context of electronic conduction in atomic lattices. The crucial advantage that optical lattices grant to this problem is an extremely long relaxation time. Since the study of any quantum mechanical effect demands the preservation of fragile interference effects, the relaxation time must be much longer than the characteristic coherence time scales of the effect in question. In this way optical lattices provide an almost ideal experimental system for this study.

The theory and experimental study of a stationary, one-dimensional cosine potential is presented. The spectral features of this potential are probed and Rabi oscillations between band states are observed.

The first direct observation of dynamical band suppression, an effect first predicted in the context of electronic conduction, is described. A theoretical analysis is provided which goes beyond the existing analyses to include the effect of higher bands on the phenomenon.

The third study is that of the Wannier-Stark ladder and Bloch oscillations. The first experimental evidence of the fractional Wannier-Stark ladder is also presented.

The final study is that of quantum tunneling. The lifetimes of the Wannier-Stark states are measured and compared with Landau-Zener theory. Deviations in the tunneling rates from the theoretical predictions are observed and are found to be due to resonant enhanced tunneling between the ladder states embedded in the continuum. Finally, the short time behavior of the atomic tunneling is studied, and deviations from the exponential decay law are observed. This is the first and only observation of non-exponential decay, a completely general and fundamental prediction of quantum mechanics.

Table of Contents

Acknowledgements	v
Abstract	viii
List of Figures	xiii
Chapter 1. Introduction	1
1.1 The interaction of atoms and light	1
1.2 Optical lattices	2
1.3 A two-level atom in a standing wave of light	4
1.4 Connections to solid-state physics	8
Chapter 2. Experimental Method	12
2.1 Overview	12
2.1.1 Computer control	14
2.2 Initial conditions	20
2.3 Experimental realization of the optical lattice	26
2.3.1 Form of the optical potential	26
2.3.2 Well depth characterization	27
2.3.3 Spontaneous emission rate in an optical lattice	29
2.3.4 Amplitude and phase modulation	30
2.4 Detection and measurement	41
Chapter 3. The time-independent cosine potential	43
3.1 Transformation to scaled quantities	43
3.2 Classical treatment: the pendulum	46
3.3 The quantum pendulum: Mathieu's equation	49
3.4 The linear periodic potential and the quantum rotor	50
3.5 Bloch's Analysis	54

3.5.1	Bloch's Theorem	54
3.5.2	Properties of Bloch states	55
3.6	Wannier Functions	64
3.7	Solving the Schrödinger equation for a time independent cosine potential	66
3.7.1	A weak periodic potential: Bragg scattering and avoided level crossings	67
3.8	An experimental study of the Bloch band spectrum	74
3.8.1	Observation of Rabi oscillations between Bloch bands	76
Chapter 4. Dynamical Bloch band suppression		85
4.1	Introduction	85
4.2	Single band calculation	86
4.3	Observation of Bloch band suppression	88
4.4	Multi-band analysis of band suppression	92
Chapter 5. Bloch oscillations and the Wannier-Stark Ladder		98
5.1	Bloch oscillations	99
5.1.1	The adiabatic approximation: a sufficiently weak acceleration	102
5.2	The Wannier Stark ladder	104
5.2.1	Wave interference: the spectral ladder and tunneling resonances	109
5.3	Observation of the Wannier-Stark ladder	111
5.4	Observation of the fractional Wannier-Stark ladder	117
Chapter 6. Quantum tunneling		119
6.1	Introduction: an atom accelerator	119
6.1.1	The classical limit for this atom accelerator	120
6.2	Observation of quantum tunneling: is the observed loss really due to tunneling?	123
6.3	Theoretical analysis of interband tunneling	126
6.3.1	Zener breakdown	126
6.3.2	Landau-Zener theory of non-adiabatic transitions	129
6.4	Observation of deviations from the Landau-Zener prediction	130
6.5	Non-exponential decay	136

Appendix	145
Appendix A. Unitary Transformations	146
A.1 The action of a unitary transformation on the Hamiltonian	146
A.2 A general one-dimensional coordinate transformation	147
A.3 Canonical Transformations	150
A.3.1 Transformation for a general time dependent phase: from lab frame to potential frame	150
A.3.2 Example I: An accelerating and modulating phase	152
Bibliography	153
Vita	162

List of Figures

2.1	Experimental sequence	13
2.2	Two dimensional image of atomic distribution	15
2.3	One-dimensional lineshape of atomic distribution	16
2.4	MOT timing diagram	17
2.5	Optical lattice timing diagram	18
2.6	Hybrid computer system	19
2.7	MOT Control Schematic	21
2.8	Optical lattice Control Schematic	22
2.9	Laser table	23
2.10	Term diagram for the sodium D ₂ line	25
2.11	Optical lattice setup	32
2.12	Heterodyne schematic	34
2.13	Tunneling velocity profile	35
2.14	AOM transfer function	38
2.15	AOM velocity response	39
2.16	AOM acceleration response	40
2.17	Molasses detection efficiency envelope	41
3.1	Pendulum phase portrait	48
3.2	Band edges versus well depth	51
3.3	Bloch band dispersion curves	52
3.4	Band structure with avoided crossings	70
3.5	Dispersion branches with Bragg resonances	72
3.6	Band structure showing spectroscopic probe	77
3.7	Calculated Rabi frequency and amplitude for three transition pairs	78
3.8	Measured Rabi oscillations for various probe strengths	79
3.9	Measured Rabi frequencies versus modulation amplitude	81

3.10	Rabi oscillations at various points in the Bloch band	83
4.1	Band collapse in the single band approximation	89
4.2	Measured band suppression spectra	91
4.3	Floquet spectra and calculated absorption spectra for band suppression	95
5.1	Illustration of Bloch oscillations and tunneling	101
5.2	Wannier-Stark resonances	112
5.3	Wannier-Stark ladder resonances	115
5.4	Wannier-Stark ladder fan chart	116
5.5	Fractional Wannier-Stark ladder	118
6.1	Classical Accelerator	122
6.2	Observation of tunneling	124
6.3	Schematic of tilted bands: Zener Breakdown	127
6.4	Schematic of resonance enhanced tunneling	131
6.5	Tunneling lifetime versus acceleration	133
6.6	Tunneling lifetime versus acceleration: resonance enhanced tunneling	134
6.7	Schematic of tunneling for large accelerations	135
6.8	Observation of non-exponential decay at 7000 m/s ²	139
6.9	Observation of non-exponential decay at 7000 m/s ² : close up .	140
6.10	Observation of non-exponential decay at 9000 m/s ²	141
6.11	Observation of non-exponential decay at 9000 m/s ² : close up .	142

Chapter 1

Introduction

In this first chapter, we introduce the idea of an optical lattice, a periodic structure formed by the wave interference of two or more modes of the electromagnetic field. We also discuss its use in the experimental study of quantum transport.

1.1 The interaction of atoms and light

When light interacts with atoms, both energy and momentum can be exchanged, and these exchange processes can be classified according to whether they are coherent (stimulated) or incoherent (spontaneous). The latter type is responsible for the radiation pressure force and the dissipative cooling and trapping forces used in this experiment to prepare a cold atomic sample. Since in all cases of spontaneous emission the scattered photon is equally likely to be in the mode $\hbar\vec{k}$ as $-\hbar\vec{k}$, on average there is no net momentum change on re-emission and therefore the incident photon recoil determines the motion of the atom.

Coherent scattering, in contrast to the random process of incoherent scattering, is an effect in which the re-emitted photon is *stimulated* out by the ambient electromagnetic field and, as a result, emerges in phase with this stimulating field. For this reason it is referred to as coherent. The momentum

imparted to the atom is simply the vector difference of the incident and outgoing photon momenta. It can be shown, using the “dressed state picture,” that the atomic energy levels are shifted due to these scatterings of the ambient field [7]. This modification of the level structure is called the AC Stark effect and results in a force referred to as the dipole force. The classical picture is that the laser field polarizes the atom and the atomic dipole has an associated energy related to its orientation with respect to the field polarization. This dipole interaction then produces an intensity-dependent energy shift that results in a force proportional to the intensity gradient. The dipole force dominates the spontaneous emission force when far detuned light (compared to the natural linewidth) is used, since the spontaneous force falls off quadratically with the detuning from resonance Δ_L , while the dipole force only falls off linearly in the limit of large detuning [7]:

$$F_{\text{dipole}} \propto \frac{\nabla I}{\Delta_L} \quad (1.1)$$

$$F_{\text{spont}} \propto \frac{I}{\Delta_L^2}. \quad (1.2)$$

Here, I is the laser intensity. From these scaling laws it is clear that with sufficient laser intensity, the spontaneous force can be negligibly small while still generating an appreciable dipole force. While the laser cooling and trapping required to prepare our atomic sample were accomplished with near resonant light, the optical lattice was composed of far-detuned light, so that only the dipole force interaction was important.

1.2 Optical lattices

An optical lattice is simply a periodic structure formed by the wave interference of two or more modes of the electromagnetic field. One particular lattice type is a spatially periodic variation in the intensity of the resultant electric field.

Since the internal energy structure of an atom depends on the time averaged electric field, the intensity profile acts like an external periodic potential. Another type of lattice is a periodic variation in the polarization, which produces different energy shifts for different hyperfine sublevels. Perhaps the simplest configuration for an optical lattice is a one-dimensional standing wave generated by two linearly polarized, counter-propagating traveling waves of equal frequency and amplitude. The electric field is of the form

$$\begin{aligned}\vec{E}(x, t) &= \hat{y}E_0 \cos(\omega_L t + k_L x) + \hat{y}E_0 \cos(\omega_L t - k_L x) \\ &= \hat{y}E_0 \cos(k_L x)(e^{-i\omega_L t} + \text{c.c.}),\end{aligned}\tag{1.3}$$

and the corresponding intensity is

$$\begin{aligned}I &\propto \langle \vec{E} \cdot \vec{E} \rangle \\ &\propto \cos^2(k_L x).\end{aligned}\tag{1.4}$$

Since it is only the gradient of the intensity that affects the dynamics, we may subtract a constant offset from the intensity, and we are left with an effective potential

$$V(x) \propto \cos(2k_L x),\tag{1.5}$$

which has a periodicity of

$$a = \frac{2\pi}{2k_L} = \frac{\lambda_L}{2}.\tag{1.6}$$

In general, the traveling waves need not be precisely counter propagating, and in the case where the wave vectors are at an angle θ , the resultant potential is

$$V(x) \propto \cos[2k_L x \sin(\theta/2)],\tag{1.7}$$

with a corresponding periodicity of

$$a = \frac{\lambda_L}{2 \sin(\theta/2)}.\tag{1.8}$$

The position of the standing wave can be controlled by varying the relative phase of the two beams. Equivalently, the optical potential will move at a constant velocity proportional to the frequency difference $\Delta\nu = \nu_1 - \nu_2$ between the two beams. This effect is most easily seen when one considers that there exists a reference frame moving at velocity v such that the Doppler shift cancels out the frequency difference:

$$v = \frac{\lambda_L}{2} \Delta\nu. \quad (1.9)$$

Since an atom with a kinetic energy much greater than the depth of the optical potential essentially moves “over hill and dale” as a free particle, equivalently, a standing wave composed of two beams with a large frequency difference will not affect the motion and can be treated as an average, spatially-uniform offset in the energy. Therefore, one could consider adding other beams (e.g., perpendicular to the first pair) that would generate periodic variations in more than one dimension. By adding a frequency offset between the beam pairs so that the interference pattern generated by two beams from differing pairs could be neglected due to its large effective velocity.

1.3 A two-level atom in a standing wave of light

In this section, we derive the effective Hamiltonian for a two-level atom in a standing wave of far-detuned light. In this derivation, we treat the electromagnetic field classically and derive the specific quantum mechanical form of the interaction for a one-dimensional optical lattice. This formulation closely follows the derivation by Graham *et al.* [8]. Alternatively, we could have derived the AC Stark energy shift by quantizing the field and using the dressed state picture, which involves solving for the eigenenergies of the combined atom-field states [7].

We begin by assuming that the atoms are isolated so that we can con-

sider just a single atom interacting with the optical field. In addition, we assume that the atom has a single ground state $|g\rangle$ and a single excited state $|e\rangle$ separated in energy by $\hbar\omega_0$ and with a transition dipole moment d . The full Hamiltonian energy will be a sum of the center of mass part, the internal energy, and the interaction term,

$$\hat{H} = \hat{H}_{\text{cm}} + \hat{H}_{\text{internal}} + \hat{H}_{\text{interaction}}, \quad (1.10)$$

where

$$\hat{H}_{\text{cm}} = \frac{\hat{p}^2}{2M}, \quad (1.11)$$

$$\hat{H}_{\text{internal}} = \hbar\omega_0 |e\rangle\langle e|, \quad (1.12)$$

and

$$\hat{H}_{\text{interaction}} = -e\hat{\mathbf{r}} \cdot \mathbf{E}(\mathbf{r}, t). \quad (1.13)$$

Using the *dipole approximation*, we replace the position of the electron \mathbf{r} with the center-of-mass position of the atom \mathbf{R} in the argument of the electric field amplitude. We have then

$$\hat{H}_{\text{interaction}} = -\hat{\mathbf{d}} \cdot \mathbf{E}(\mathbf{R}, t). \quad (1.14)$$

For the two-level atom, the the dipole matrix element projected along the electric field is

$$d = \left| \langle e | \hat{\mathbf{d}} \cdot \hat{\boldsymbol{\epsilon}} | g \rangle \right|. \quad (1.15)$$

Later, we will discuss the consequence of the fact that sodium is not a two-level atom, and we will find the correct form for the interaction term. Using a one-dimensional, linearly polarized standing wave as in Eq. (1.3) but allowing the field amplitudes and frequencies to differ,

$$\mathbf{E}(x, t) = \hat{\boldsymbol{\epsilon}} [E_1 \cos(\omega_1 t + k_1 x) + E_2 \cos(\omega_2 t - k_2 x)], \quad (1.16)$$

we find that the interaction term is

$$\begin{aligned}\hat{H}_{\text{interaction}} &= -d(|e\rangle\langle g|e^{i\omega_0 t} + |g\rangle\langle e|e^{-i\omega_0 t})E \\ &= -\frac{d}{2} \left[E_1 \sigma^+ e^{i(\omega_0 t - \omega_1 t - k_1 x)} + E_2 \sigma^+ e^{i(\omega_0 t - \omega_2 t + k_2 x)} + \text{H.c.} \right],\end{aligned}\tag{1.17}$$

where we are using the rotating wave approximation, ignoring the sum frequency terms of the form $e^{\pm i(\omega_0 t + \omega t)}$ [9]. Also, we are using the Pauli raising and lowering operators σ^\pm . Since the center of mass wave function is separable, we only consider motion along the x -axis. Without loss of generality, we write the atomic state as

$$|\Psi(x, t)\rangle = c_g(x, t)|g\rangle + c_e(x, t)e^{-i\Delta_L t}|e\rangle,\tag{1.18}$$

where the detuning from resonance is defined as

$$\Delta_L = \omega_1 - \omega_0.\tag{1.19}$$

If we insert $|\Psi\rangle$ into the Schrödinger equation

$$i\hbar \frac{\partial}{\partial t} |\Psi\rangle = \hat{H} |\Psi\rangle,\tag{1.20}$$

we find

$$\begin{aligned}i\hbar \left(\frac{\partial c_g}{\partial t} |g\rangle + \frac{\partial c_e}{\partial t} e^{-i\Delta_L t} |e\rangle - i\Delta_L c_e e^{-i\Delta_L t} |e\rangle \right) = \\ - \frac{\hbar^2}{2M} \frac{\partial^2 c_g}{\partial x^2} |g\rangle - \frac{\hbar^2}{2M} \frac{\partial^2 c_e}{\partial x^2} e^{-i\Delta_L t} |e\rangle \\ + \hbar\omega_0 c_e e^{-i\Delta_L t} |e\rangle \\ - \frac{d}{2} \left[E_1 e^{i(\omega_0 t - \omega_1 t - k_1 x)} + E_2 e^{i(\omega_0 t - \omega_2 t + k_2 x)} \right] |e\rangle c_g \\ - \frac{d}{2} \left[E_1 e^{-i(\omega_0 t - \omega_1 t - k_1 x)} + E_2 e^{-i(\omega_0 t - \omega_2 t + k_2 x)} \right] |g\rangle c_e e^{-i\Delta_L t}.\end{aligned}\tag{1.21}$$

Operating on the left with $\langle g|$ gives

$$i\hbar \frac{\partial c_g}{\partial t} = -\frac{\hbar^2}{2M} \frac{\partial^2 c_g}{\partial x^2} - \frac{d}{2} \left[E_1 e^{ik_1 x} + E_2 e^{i(\delta t - k_2 x)} \right] c_e,\tag{1.22}$$

and operating on the left with $\langle e|$ gives

$$i\hbar \frac{\partial c_e}{\partial t} = -\frac{\hbar^2}{2M} \frac{\partial^2 c_e}{\partial x^2} - \frac{d}{2} \left[E_1 e^{-ik_1 x} + E_2 e^{-i(\delta t - k_2 x)} \right] c_g - \hbar \Delta_L c_e, \quad (1.23)$$

where the frequency difference between the two constituent beams is $\delta = \omega_2 - \omega_1$. For a sufficiently large detuning from resonance, we can neglect spontaneous scattering and simplify these equations by adiabatically eliminating the excited state amplitude [8]. This procedure follows from a comparison of the time/energy scales represented by each of the terms in Eq. (1.23):

$$\begin{aligned} \frac{1}{\hbar} \frac{p^2}{2M} &\approx 1 \text{ MHz (several recoil energies)} \\ \Omega = \frac{\mathbf{d} \cdot \mathbf{E}_0}{\hbar} &\approx 500 \text{ MHz} \\ \Delta_L &\approx 100 \text{ GHz} \end{aligned} \quad (1.24)$$

We may safely discard the kinetic energy term and write c_e as a product of two time-dependent terms,

$$c_e(t) = c'_e(t) e^{-i\Delta_L t}. \quad (1.25)$$

Inserting this expression into Eq. (1.23) and taking $\frac{\partial^2 c_e}{\partial x^2} = 0$, we have that

$$c'_e(t) = \int_0^t \frac{d}{i2\hbar} \left[E_1 e^{-ik_1 x} + E_2 e^{-i(\delta t - k_2 x)} \right] c_g(t') e^{+i\Delta_L t'} dt', \quad (1.26)$$

where we have taken $c'_e(0) = 0$. The adiabatic assumption asserts that $c_g(t')$ varies much more slowly than $e^{+i\Delta_L t'}$ and can be taken outside the integral.

We now have

$$c_e = -\frac{d}{2\hbar\Delta_L} \left[E_1 e^{-ik_1 x} + E_2 e^{-i(\delta t - k_2 x)} \right] c_g. \quad (1.27)$$

Substituting this into Eq. (1.22) leaves us with

$$i\hbar \frac{\partial c_g}{\partial t} = -\frac{\hbar^2}{2M} \frac{\partial^2 c_g}{\partial x^2} + \frac{d^2}{4\hbar\Delta_L} \left[E_1^2 + E_2^2 + 2E_1 E_2 \cos(k_1 x + k_2 x - \delta t) \right]. \quad (1.28)$$

Shifting the overall energy by $(d^2/4\hbar\Delta_L)(E_1^2 + E_2^2)$ does not affect the dynamics, and we have the effective Hamiltonian for an atom in the ground state,

$$\hat{H} = \frac{\hat{p}^2}{2M} + V_0 \cos(2k_L \hat{x} - \delta t), \quad (1.29)$$

where k_L is the average wave vector, and the well depth is given by

$$V_0 = \frac{E_1 E_2 d^2}{2\hbar\Delta_L}. \quad (1.30)$$

None of the alkali atoms, including sodium, is a true two-level atom; however, by optically pumping our atomic sample, only one ground state F level is populated. Moreover, since all of the (nearly) degenerate m_F levels experience the same well depth in the far detuned regime, the entire sample experiences the same effective potential [7, 10]. This result is only true for linearly polarized light. For elliptically polarized light, the sum of the dipole matrix elements squared will in general depend on the hyperfine sublevel. In some cases we did not directly optically pump the sample, but the magneto-optic trap naturally produces a distribution which strongly favors the upper $F = 2$ ground state. The dipole matrix element can be determined from the Einstein A coefficient and will be done so in Chapter 2.

1.4 Connections to solid-state physics

The study of quantum transport began as early as the late 1920's when Felix Bloch applied the nascent ideas of quantum mechanics to the problem of electronic conduction in metallic crystals. He showed that because of the periodicity of the lattice, the eigenstates were plane waves modulated by periodic functions of position [11]. Moreover, he showed that due to the discrete translational symmetry, there was a new conserved quantity k , called the quasimomentum, that behaved like the free particle momentum. As for a free particle, the velocity of a Bloch state is related to the energy by the derivative with

respect to the momentum, and as for a free particle, the time rate of change of the quasimomentum is equal to the force from an applied field. These results led Bloch, and others, to the realization that electrons should *oscillate* instead of accelerate uniformly in response to an applied, static electric field [11, 12, 13]. This phenomenon of Bloch oscillations was predicted to produce a spectral feature called the Wannier-Stark ladder [14]. Additionally, the lifetime of the Wannier states was predicted to be governed by Landau-Zener tunneling [13, 15, 16]. These fundamental predictions concerning quantum transport in general periodic potentials waited decades before experimental science could provide supporting evidence. In 1972, optical absorption measurements of Gallium Arsenide performed by Koss and Lambert provided the first experimental observation of the Wannier-Stark resonances [17]. This experiment followed fourteen years of debate in the community about their very existence. In the years that followed, spurred on by the hope of harnessing the Bloch oscillator for the generation of terahertz radiation, improvements were made in the purity of the materials as well the structure. Namely, researchers developed superlattices that shortened the Bloch oscillation period below the electronic relaxation time, and this technique produced much cleaner results [18, 19, 20].

Somewhat in parallel, advances were being made in the field of laser cooling and trapping. In 1985, the first demonstration of laser cooling of a room temperature atomic vapor (300 K) to 50mK was made, and only three years later a magneto-optic trap was realized in which a the atomic sample could be cooled and confined [21]. Then in 1996, Ben-Dahan *et al.* observed Bloch oscillations for the first time using a laser cooled sample of Cesium atoms in a far detuned accelerating optical lattice [22]. Almost simultaneously, we made our measurements of the Wannier-Stark ladder using optical lattices [2]. These two experiments marked the beginning of the study of quantum

transport with optical lattices [23, 24]. Since those first experiments, we have studied tunneling [3], non-exponential decay [4], Rabi oscillations between Bloch bands [5], and the phenomenon of band collapse [6] using optical lattices.

The crucial advantage that optical lattices grant to this problem is an extremely long (infinite by comparison) relaxation time. In solids, relaxation happens because of electron scattering from lattice phonons, impurities, lattice dislocations, or other electrons. In our optical lattice, the relaxation time was determined by the spontaneous emission rate. Although phase instabilities were present, they were at a very low level. Moreover, although they are random, they preserve the lattice periodicity and are hence inherently non-dissipative. To be fair, the figure of merit for decoherence, or the lack thereof, is given by the ratio of the relaxation time to the characteristic coherent time scale. This ratio for the study of Bloch oscillations in optical lattices is presently over 2500 while for superlattices it is on the order of 1 (see Table 1.1).

Some excellent work on cooling and wave packet manipulation has been done with near resonant optical lattices [25, 26]; however, it must be stressed that the phenomena studied and presented in this dissertation rely on the uninterrupted coherent evolution associated with the conservative dipole potential. These coherent effects are destroyed by the dissipative, incoherent scattering of spontaneous photons which occurs when the atomic resonance is approached.

In Table 1.1 a comparison of the parameters for atomic superlattices and optical lattices is given. One major difference between these two systems is that in the atomic system, there is no significant particle-particle interaction since the sample is so dilute and the collisional cross section is small. This is very unlike the electronic case where there is both a long range electrostatic interaction and an exchange interaction due the half integer elec-

Table 1.1: Comparison of physical parameters

	Superlattices	Optical lattices	
Particles	electrons	^{133}Cs atoms	^{23}Na atoms
Type	fermions	bosons	bosons
Lattice constant	10 nm	426 nm	295 nm
Bloch bandwidth	250 GHz	2 kHz	25 kHz
Free-particle density	$10^{18}/\text{cm}^3$	$10^{10}/\text{cm}^3$	$10^{10}/\text{cm}^3$
Particles per lattice site	1	0.1	0.06
Thermal velocity (in 1 dim.)	10 km/s	0.8 mm/s	59 mm/s
Bloch period (τ_B)	0.4 ps	0.1 ms	25 μs
Relaxation time (τ_r)	0.35 ps	250 ms	10 ms
τ_r/τ_B	~ 1	~ 2500	~ 400

tron spin. Future studies of quantum transport with optical lattices will most probably include the use of a Bose condensate to study collective effects, and, although it has not yet been achieved with laser cooling, a degenerate Fermi gas could be studied as well. It has been predicted that the fermionic particle density in a lattice has a quantized response to a dilation of the period [27]. It has also been suggested that quantized adiabatic particle transport could be studied with optical lattices [28]. Finally, there are a number of interesting phenomena predicted for quantum transport in quasiperiodic lattices [29, 30].

Chapter 2

Experimental Method

2.1 Overview

This experimental study of optical lattices consisted of three important components: the preparation of the initial conditions, the generation of the interaction potential, and the measurement of the final state of the atoms. A schematic of the entire experimental sequence is shown in Fig. 2.1, and the timing diagrams for the resonant trapping light and the optical lattice light are provided in Figs 2.4 and 2.5.

The initial conditions were a spatially localized ensemble of atoms prepared in the fundamental band of the optical lattice. This ensemble was prepared by first trapping and cooling a room temperature vapor in a magneto-optic trap. Then the optical lattice was turned on and the subset of atoms projected into the fundamental band was separated in velocity from those atoms in higher bands by an acceleration of the lattice. By a careful choice of the well depth $V_{\text{transport}}$ and acceleration $a_{\text{transport}}$ (see Fig. 2.5), the tunneling rate from the first to the second band was very small while the rate across all other band gaps was large. This situation allows only those atoms in the first band to be accelerated by the lattice while leaving all other atoms unaffected. After this preparation stage, the optical lattice position and amplitude were varied to realize the potential under study. During this stage a subset of the prepared atoms were excited to higher bands. This step was followed by the

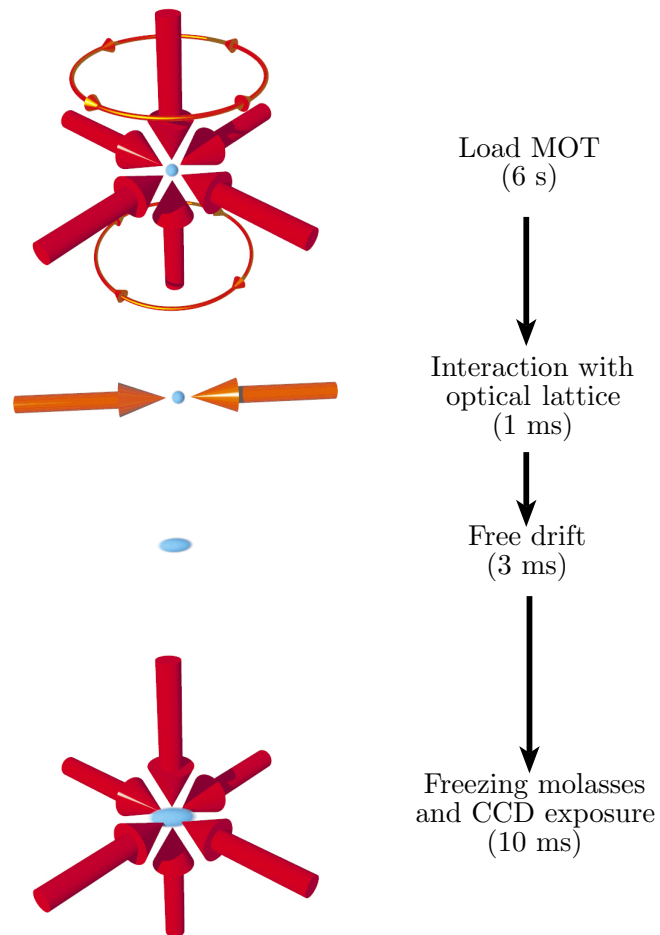


Figure 2.1: Schematic of the experimental sequence. First the atoms are collected and cooled in the MOT. The trapping fields are extinguished and the the optical lattice is introduced. After interacting with the optical lattice, the atoms are allowed to drift freely in the dark. Finally, the cooling beams are turned on freezing the atoms in place and the flurorescence is imaged on a CCD camera.

measurement of the survival probability of the lowest band. As was done for the preparation of the initial conditions, an acceleration was imposed which transported those atoms which were in the lowest band, survivors of the interaction, to a higher velocity. The timing diagram for this sequence is shown in Fig. 2.5. The atoms were finally allowed to drift freely in the dark for a few milliseconds, and a “freezing” molasses was turned on to image their spatial distribution on a charge coupled device camera (CCD) [21]. An example of a two dimensional CCD image obtained is shown in Fig. 2.2. This image consists of three distributions: (1) atoms that were not initially trapped in the lowest band and immediately tunneled out of the well during the initial acceleration, (2) atoms that were trapped in the first band at the beginning of the interaction but were driven out, and (3) atoms that remained in the first band during the entire sequence. The normalized population of the fundamental band was then calculated by dividing the fluorescence of group (3) by the sum of that from groups (2) and (3). Typically, these images were integrated along the vertical axis to produce a one-dimensional line-shape along the optical lattice axis since the motion in the other two dimensions was essentially free and therefore contained no information other than the initial MOT temperature. An example of this one dimensional lineshape is provided in Fig 2.3.

2.1.1 Computer control

The experimental sequence is shown in Fig. 2.1. The timing of the experimental steps required great precision (100 ns resolution) and was completely automated. Although functional, the computer system, shown in Fig. 2.6, was a hybrid of PC and Mac platforms. The PC was used to trigger the experiment and program the external function and arbitrary waveform generators while the Mac collected the CCD images from the Princeton Instruments camera controller. The PC also analyzed the photodiode-signal records of the optical

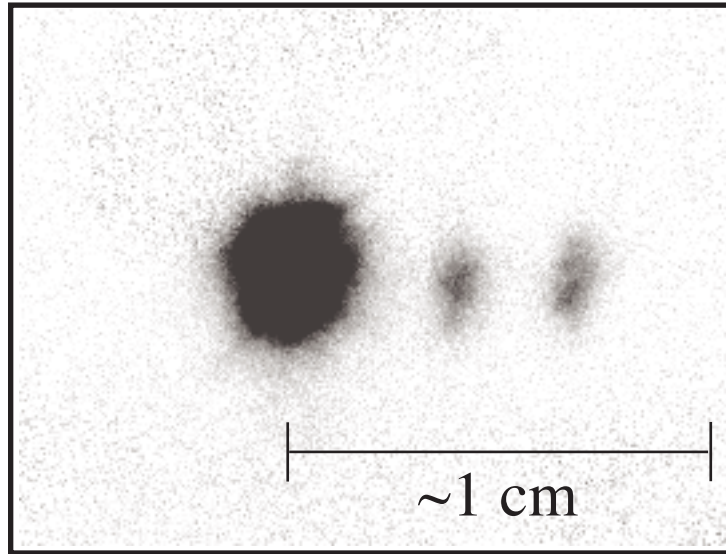


Figure 2.2: Image of resonance fluorescence from an atomic distribution acquired by the CCD camera. This exposure is taken during the freezing molasses period following a free drift. It consists of three distributions: (1) atoms that were not initially trapped in the lowest band and immediately tunneled out of the well during the initial acceleration are located in the left group, (2) atoms which were trapped in the first band at the beginning of the interaction but were driven out are the middle bunch, and (3) atoms that remained in the first band during the entire sequence are found in the right group. The normalized population of the fundamental band was then calculated by dividing the total fluorescence of group (3) by the sum of that from groups (2) and (3).

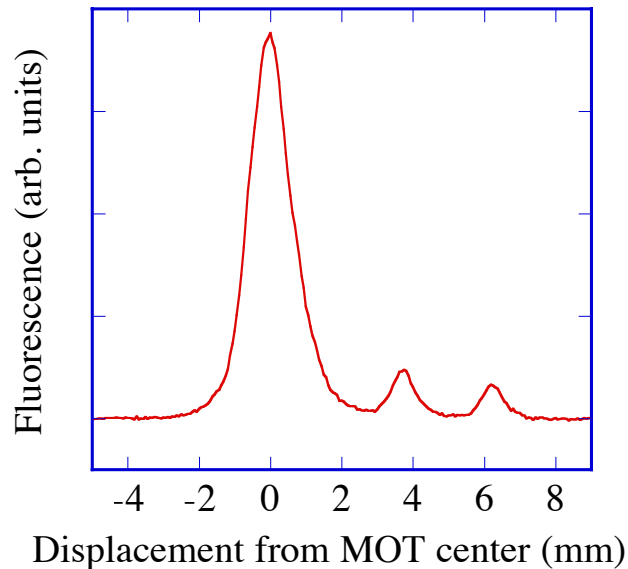


Figure 2.3: The one-dimensional lineshape of the atomic distribution obtained by integrating along the optical lattice axis a two dimensional image (as in Fig 2.2) acquired by the CCD camera.

lattice intensity captured by an external digitizing oscilloscope.

The 486-33 MHz PC was fitted with two general purpose National Instrument I/O boards: a PC-DIO-24 board with TTL ports for generating timing triggers, and a GPIB-PCIIA board for high-level control of other devices. The National Instruments Lab Windows-DOS compiler/debugger was used to code the programs, which were then compiled with Microsoft C 6.0 into stand-alone executables. Since the output of the I/O boards was interrupt driven, the timing was slow (with a resolution of about $20 \mu\text{s}$) and random at the level of its resolution. Therefore, the PC-DIO-24 board was used essentially to start the experiment. All of the critical timing was provided by Fluke-Philips PM 5712/5715 pulse generators and by Stanford Research Systems DS345 and Tektronix AWG5105 programmable arbitrary waveform generators. The control hierarchy for the trapping and measurement electronics is given in Fig. 2.7,

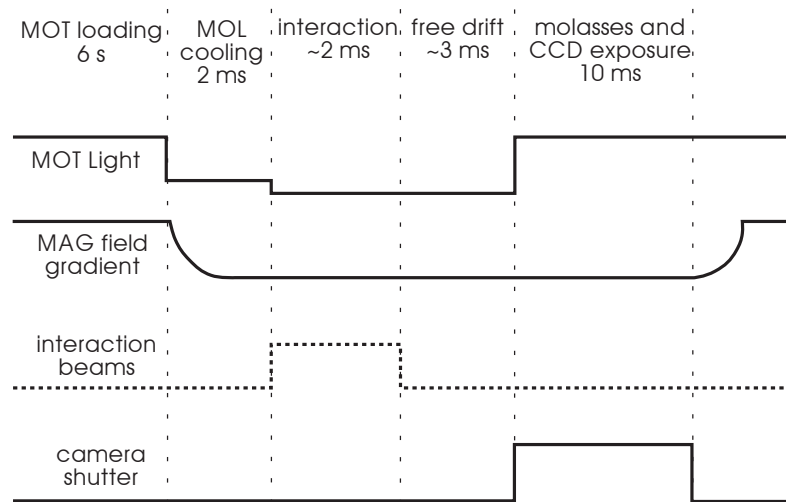


Figure 2.4: Timing diagram for the trapping and cooling sequence as well as the exposure following the interaction. First the atoms are collected and cooled in the MOT. The magnetic fields are then turned off for 2 ms of cooling. Then the resonant light is turned off and the optical lattice is introduced. After interacting with the optical lattice, the atoms are allowed to free drift in the dark. Finally, the cooling beams are turned on, freezing the atoms in place, and the fluorescence is imaged on a CCD camera.

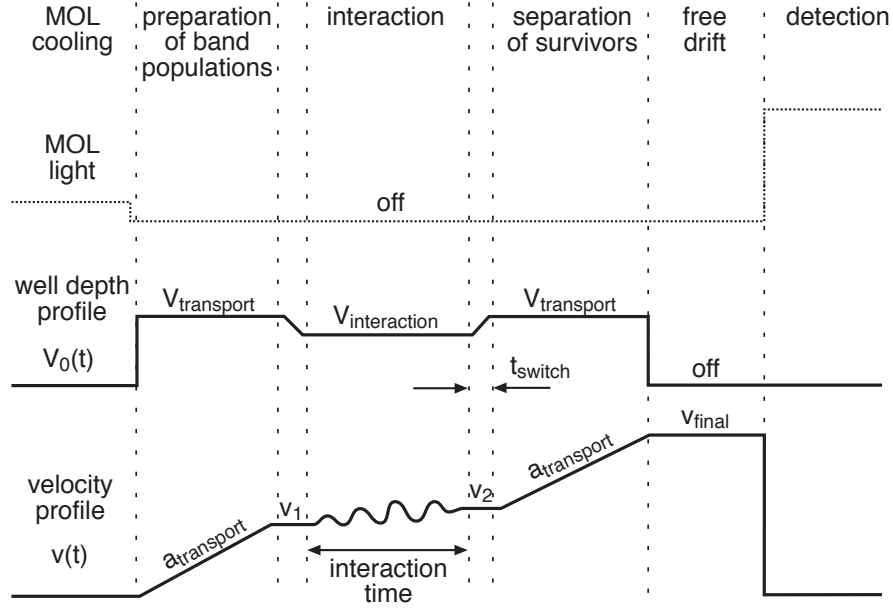


Figure 2.5: Timing diagram for the interaction sequence. Both the optical lattice well depth and velocity are shown. After the cooling stage the resonant light is turned off and the optical lattice was turned on. A subset of atoms is projected into the fundamental band and separated in velocity by an acceleration $a_{\text{transport}}$. After this preparation stage, the optical lattice position and amplitude were varied to realize the potential under study. This step was followed by separating the atoms in the lowest band from those in higher bands by the same acceleration $a_{\text{transport}}$. The atoms are then allowed to free drift in the dark and the spatial distribution is illuminated with the resonant molasses light.

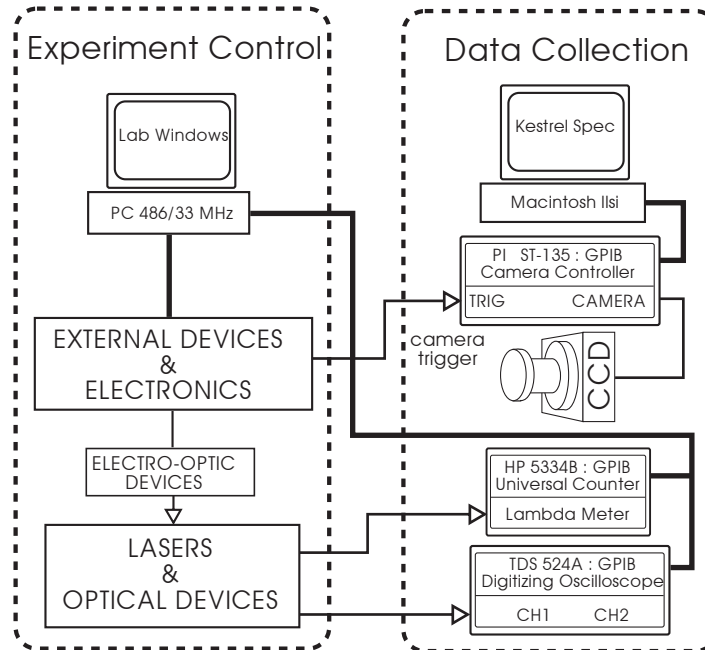


Figure 2.6: The programming and control of the experimental devices was handled by a 486/33 MHz PC running Lab Windows while the data collection from the CCD camera was performed by a Mac IIsi. This hybrid system, although functional, had certain disadvantages. The main drawback was that data analysis required information from both systems and so could not be done on line without using a third system (typically a unix based mainframe for variety).

and the hierarchy for the optical lattice electronics is shown in Fig. 2.8. In both cases, RF signals are tailored, amplified, and sent to acousto-optic modulators that send the proper beams with the proper amplitudes and frequency offsets to the atoms.

2.2 Initial conditions

The collection and cooling of the sodium was accomplished by a standard $\sigma^+ - \sigma^-$ magneto-optic cell trap (MOT) [21, 31]. Approximately 10^5 atoms were trapped in a Gaussian distribution with a width of $\sigma_x = (0.20 \pm 0.06)$ mm in position and $\sigma_p = (4.5 \pm 0.5) \hbar k_L$ in momentum, where $\hbar k_L$ is the momentum of a single photon of resonant light (589 nm). The atoms were cooled from a room temperature vapor of sodium at a pressure of about 10^{-10} Torr contained in a glass cell. The cell was attached to a 20 l/s ion pump that maintained the low pressure, while a small sodium ampoule in a copper tube attached to the chamber replenished the sodium lost due to adsorption. The trap was formed by three pairs of counter-propagating, circularly polarized laser beams that intersected at the center of the glass cell. In addition, there were two current-carrying coils in an anti-Helmholtz configuration that provided a magnetic field gradient and a zero point in the magnetic field that coincided with the intersection of the six beams. The earth's magnetic field and stray fields from the optical table were nulled to a level of 50 mG by three Helmholtz pairs aligned along three orthogonal directions.

The light for the MOT was provided by a Coherent 899-21 single mode cw dye laser pumped by a Coherent Innova 200 argon ion laser as shown in Fig. 2.9. The D_2 transition ($3S_{1/2}, F = 2$) \rightarrow ($3P_{3/2}, F' = 3$) for sodium at 589 nm was found with the aid of a NIST wavemeter with a resolution of 50 MHz, and the laser was actively locked 65 MHz to the blue of this line using saturated-absorption FM spectroscopy. Before entering the optical fiber, the

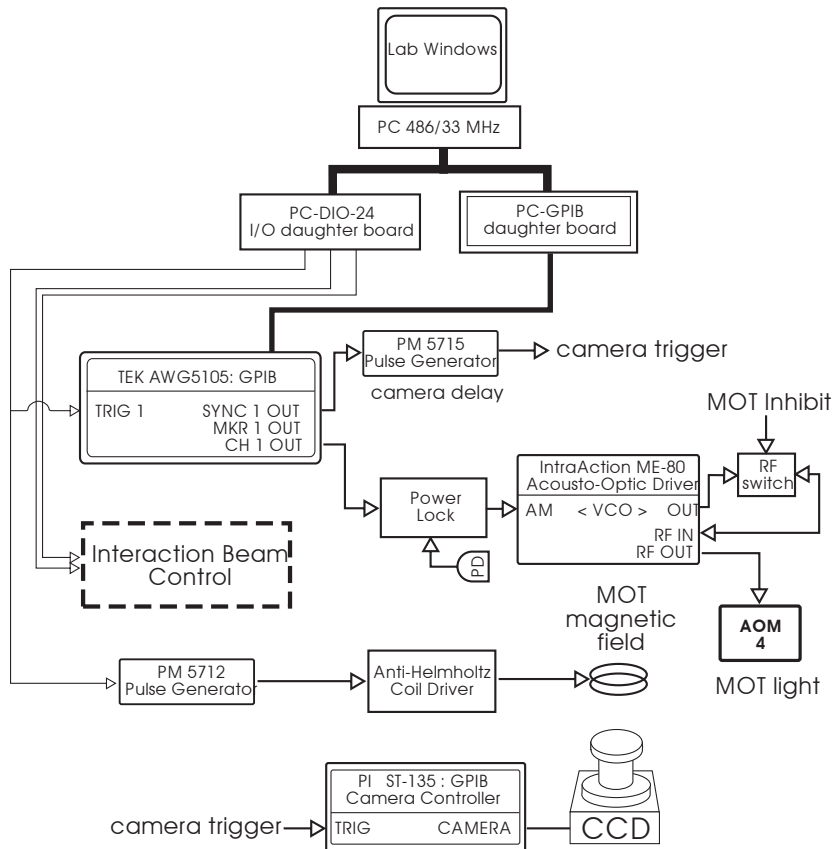


Figure 2.7: The MOT intensity was controlled via AOM4 by the TEK AWG5105 arbitrary waveform generator. It was intensity stabilized by an external lock box. The AWG also triggered the CCD controller to acquire an image.

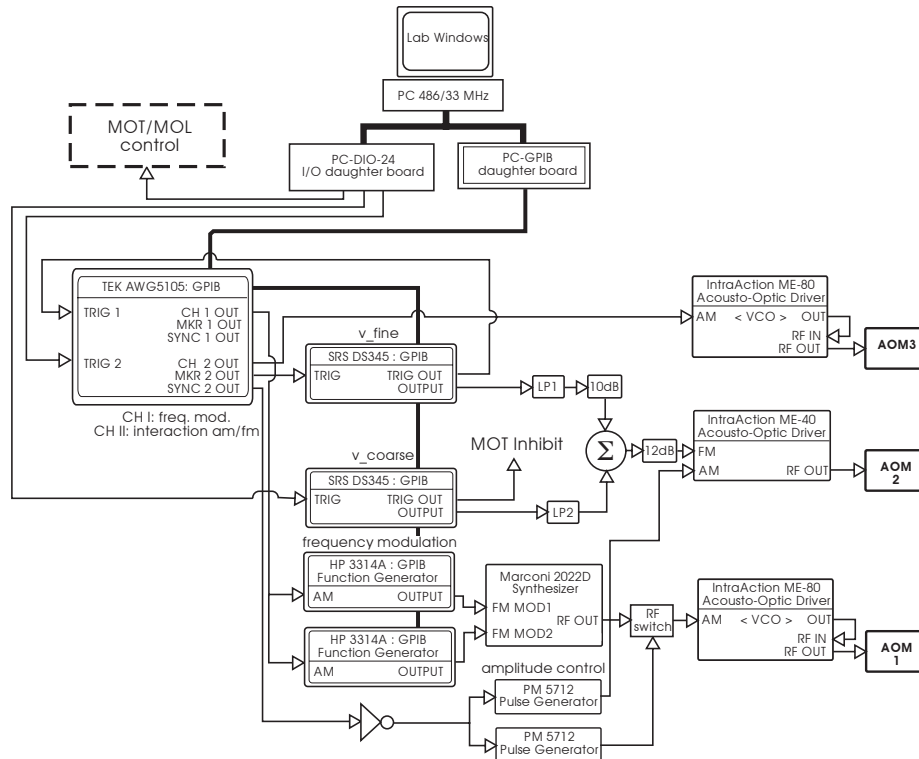


Figure 2.8: The overall intensity of the optical lattice beams was controlled through AOM3. AOM2 was double passed and produced a variable frequency offset. It was driven by two DS345s (v_{fine} and v_{coarse}) which were summed together so that extremely fine time (100 ns) and velocity (.25 recoil) resolution over the optical lattice could be achieved during the interaction time. AOM1 was driven by a stable Marconi synthesizer which could also be frequency modulated to generate the spectroscopic probe.

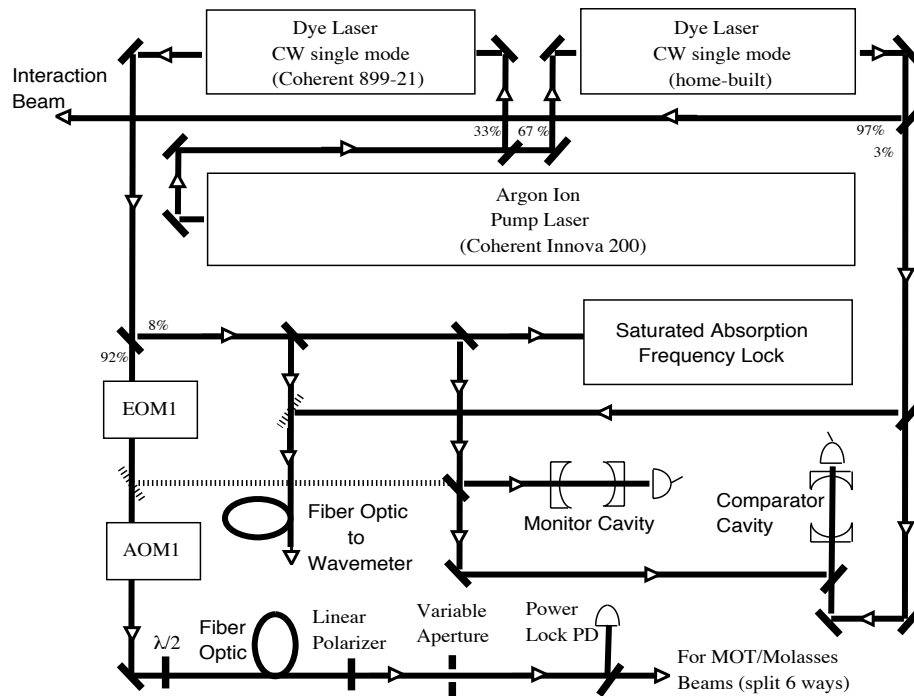


Figure 2.9: Schematic of the laser table. A single argon-ion laser pumps two cw single-mode dye lasers. The commercial dye laser (Coherent 899-21) provides the cooling and trapping beams. The home-built laser provides the optical lattice interaction beams.

light was deflected by an acousto-optic modulator (AOM1) which shifted it down by 80 MHz so that the light incident on the atoms was 15 MHz to the red of the transition. This near resonant light is tuned for the $F = 2$ ground to $F' = 3$ excited state *cycling* transition; however, it also can populate the $F' = 2$ excited state. If this happens, the atom can either decay back to the $F = 2$ ground state or fall to the $F = 1$ ground state (see Fig. 2.10). If it falls to the lower ground state, the interaction with this light stops abruptly since it is now 1.772 GHz (the ground state splitting) away from resonance. In order to prevent this optical pumping into the “dark” ground state, the MOT light was passed through an electro-optic modulator that shifted 15% of the optical power into each sideband at 1.712 GHz. The upper sideband was then resonant with the $F = 1$ ground to the $F' = 2$ excited state transition. Atoms that fell into the lower ground state were re-excited to the $F' = 2$ excited state where they could fall back to the $F = 1$ state or back to the “correct” $F = 2$ ground state. The time for optical pumping out of the cycling transition was measured to be approximately $\tau_{\text{pump}} = 30 \mu\text{s}$ by measuring the decay of MOT fluorescence with a photomultiplier tube after switching the repump sideband off. By extinguishing the repump sideband 100 μs before the cooling step ended, more than 95% of the distribution was optically pumped into the lower ground state. In most cases we did not directly optically pump the atoms; however, the repumping sideband naturally produces a distribution which strongly favors the upper $F = 2$ ground state. In either case, the vast majority of the atoms were prepared in a known ground state. A rough estimate of the steady-state populations of the two ground states can be made if we first note that the repump sideband is roughly equal to the saturation intensity 36 mW/cm^2 for the $F = 1 \leftrightarrow F' = 2$ transition for isotropic pump, and therefore the re-excitation time is on the order of twice the lifetime, $2\tau = 33 \text{ ns}$ [32]. If we assume that the atom will decay from the $F' = 2$ to the

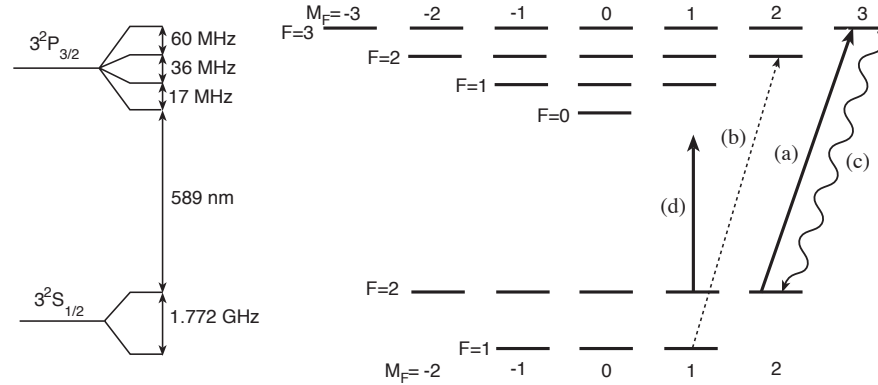


Figure 2.10: Term diagram for the sodium D₂ line. The nuclear spin of sodium is $I = 3/2$, and so the ground state of sodium $3S_{1/2}$ has two hyperfine levels $F = J + I = 1, 2$. For the $3P_{3/2}$ excited state $J = 3/2$ so $F = 0, 1, 2, 3$. The $2F + 1$ magnetic sublevels are also shown. Representative examples of (a) the cooling and trapping light, (b) the optical pumping sideband, (c) the spontaneous decay, and (d) the far-detuned optical lattice light are shown.

$F = 2$ ground state with a 50% probability, then the effective repump time is approximately four times the lifetime, $\tau_{\text{repump}} = 60$ ns. One minus the ratio of this rate with the optical pumping rate out of the $F = 2$ ground state gives the fraction occupying the upper $F = 2$ ground state:

$$P_{F=2} = 1 - \frac{\tau_{\text{repump}}}{\tau_{\text{pump}}} = 1 - \frac{60 \text{ ns}}{30 \mu\text{s}} = 99.8\%. \quad (2.1)$$

The MOT light was turned on and off and was intensity stabilized by the acousto-optic modulator (AOM1) mentioned above. The frequency-downshifted beam was aligned through a polarization-preserving fiber, which acted as a spatial filter, producing a clean gaussian spot. The MOT light emerging from the fiber was monitored continuously on a photodiode (Power Lock PD) and the signal provided the feedback necessary to stabilize the intensity. Residual fluctuations were less than 1% of the average intensity. When the far-detuned optical lattice was on and the MOT light was off, a *MOT*

inhibit signal (see Figures 2.7 and 2.8) disconnected the driver from the modulator (AOM1) to prevent any residual RF leakage that would allow resonant light to reach the atoms during the interaction.

In order to optimize the size and temperature of the atomic distribution, we would load the MOT at our highest intensity (200 mW total split between six beams) for about 3 to 4 s, and then we would extinguish the magnetic field gradient while leaving the resonant light on to maximize the polarization gradient cooling rate [33]. This final 2 ms of “improved cooling” at a detuning of (15-20) MHz reduced the momentum width by a factor of 2 from $\sigma_p = 10 \hbar k_L$ to $\sigma_p = (4.5 \pm 0.5) \hbar k_L$ without an appreciable amount of spatial spreading.

2.3 Experimental realization of the optical lattice

The optical lattice beams were provided by a home-built dye laser based on a design by Jim Bergquist at NIST in Boulder, CO [34]. This laser was also pumped by the Coherent Innova 200 argon ion laser as shown in Fig. 2.9. Typical output power was 1 W single mode with 66% of the 19 W multi-line visible pump power. The wavelength was monitored by a NIST LM-11 wavemeter and was stabilized using the Hänsch-Couillaud lock scheme [35]. The invar reference cavity used in this locking scheme drifted less than 100 MHz per hour, which was very small amount compared to the typical 30 GHz detuning.

2.3.1 Form of the optical potential

The optical potential was formed by two linearly polarized, spatially filtered, Gaussian traveling waves from the same laser. The frequencies of the two arms of the standing wave were controlled independently by two acousto-optic modulators as described in Section 2.3.4. It was very important that the beams were spatially filtered, since any higher order modes can produce transverse

interference fringes, resulting in local variations in the well depth. The spatial filtering was accomplished by focusing the light through a 50 micron pinhole. After the pinhole, a lens recollimated the beam, and a variable iris blocked all but the center lobe. The beam is then a linearly polarized, traveling Gaussian beam which we approximate with the form

$$\vec{E}_{\text{Gauss}} = \hat{y}E_0 e^{-(z^2+y^2)/w_0^2} \cos(\omega_L t + k_L x). \quad (2.2)$$

The time-averaged intensity has the form

$$\langle I \rangle = \frac{1}{2} c \epsilon_0 E_0^2. \quad (2.3)$$

The integrated power is calculated over the cross section

$$\langle P \rangle = \int \langle I \rangle dA = \pi w_0 c \epsilon_0 E_0^2 \int_0^\infty dr e^{-2r^2/w_0^2} = \frac{\pi c \epsilon_0 w_0^2 E_0^2}{4}. \quad (2.4)$$

This gives an expression for the field strength at the center of the Gaussian beam in terms of experimentally measured quantities:

$$E_0 = \sqrt{\frac{4\langle P \rangle}{c \epsilon_0 \pi w_0^2}}. \quad (2.5)$$

The average power $\langle P \rangle$ was measured with a Coherent Fieldmaster power meter which was calibrated with respect to a NIST traceable Newport model 1825-C powermeter and model 818-UV head, which has an accuracy of $\pm 5\%$. The width w_0 of the beam was measured by photographing the diffuse transmitted spot through a thin sheet of paper with our CCD camera. The typical beam width used in the experiment was 2 mm, with an absolute uncertainty of $\pm 1\%$.

2.3.2 Well depth characterization

In Section 1.3 the well depth was calculated for a two-level atom and found to be

$$V_0 = \frac{E_1 E_2 d^2}{2\hbar \Delta_L}, \quad (2.6)$$

where $\Delta_L = \omega_L - \omega_0$ is the laser detuning from the atomic resonance ω_0 , and d is the dipole matrix element between the ground and excited state. However, the D_2 transition $J = 1/2 \rightarrow J' = 3/2$ of sodium shown in Fig. 2.10 is not a two-level system. In fact, there are two ground states $F = 1$ and $F = 2$ and four excited states $F' = 0, 1, 2, 3$, each with a $2F' + 1$ degeneracy. Therefore, the actual dipole coupling for a particular ground state sublevel $|F m_F\rangle$ is obtained from summing over its couplings to all of the available excited states. When the detuning is large compared to the excited state frequency splittings, all of the excited states participate, and the detuning for each excited state is approximately the same. In addition, the dipole coupling summed over all excited states and all polarizations is independent of the m_F sublevel considered [10]. Because of the spherical symmetry of the dipole operator, the three Cartesian components in this sum are equal and therefore the effective dipole coupling for the case of linearly polarized light and large detuning regardless of the ground state population is one third the square of the dipole matrix element for the full D_2 ($J = 1/2 \leftrightarrow J' = 3/2$) transition.

$$|d_{\text{effective}}|^2 = \frac{e^2 |D_{12}|^2}{3}. \quad (2.7)$$

This result is only true for linearly polarized light. For elliptically polarized light, the sum of the dipole matrix elements squared will in general depend on the hyperfine sublevel. The dipole matrix element $e^2 |D_{12}|^2$ can be obtained from the Einstein A coefficient, which is related to the radiative lifetime [36]

$$A_{21} = \Gamma = \frac{1}{\tau} = \frac{\omega_0^3 e^2 |D_{12}|^2}{3\pi\epsilon_0 \hbar c^3} \frac{2J + 1}{2J' + 1}, \quad (2.8)$$

where $J = 1/2$ is the ground state and $J' = 3/2$ is the excited state. The radiative lifetime $\tau = 16.6$ ns is known empirically. Using Eqs. (2.7) and (2.8), the effective dipole moment is then

$$d_{\text{effective}} = \sqrt{\frac{\epsilon_0 \hbar \lambda_L^3}{4\pi^2 \tau}} = 1.71 \times 10^{-29} \text{Cm}. \quad (2.9)$$

Using this relationship, Eq. (2.5) for the field strengths, and Eq. (2.6), we find that the well depth is

$$V_0 = \frac{\sqrt{P_1 P_2}}{w_1 w_2 \Delta_L} \cdot \frac{4c^2}{\tau \omega_0^3} \quad (2.10)$$

where P_1 and P_2 are the average powers of the two beams. By some cosmic coincidence, the factor on the right is numerically very similar to h :

$$\frac{4c^2}{\tau \omega_0^3} \approx 6.62 \times 10^{12} \frac{\text{s}}{\text{kg}} \quad (2.11)$$

so that if the optical power is expressed in mW, the beam sizes in mm, and the detuning in GHz/ 2π , the expression for the well depth has a very simple form

$$V_0 \approx \frac{\sqrt{\tilde{P}_1 \tilde{P}_2}}{\tilde{w}_1 \tilde{w}_2 \tilde{\Delta}_L} \cdot \hbar \text{ MHz} \quad (2.12)$$

where this formula is accurate to three significant digits. There is nothing significant about this coincidence, but I point it out here merely for amusement.

If we write this using our natural energy unit, we get

$$V_0 \approx \frac{\sqrt{\tilde{P}_1 \tilde{P}_2}}{\tilde{w}_1 \tilde{w}_2 \tilde{\Delta}_L} \cdot 0.795 \cdot E_u \quad (2.13)$$

where $E_u = h \cdot 200 \text{ kHz}$ (see Section 3.1).

2.3.3 Spontaneous emission rate in an optical lattice

In this section, we calculate the rate of spontaneous emission induced by the far-detuned beams of the optical lattice. This quantity is very important since spontaneous emission is the dominant decohering process in these experiments. The total photon scattering rate is given by the product of the lifetime and the (steady state) excited-state population, $\Gamma \rho_{ee}$. Ignoring collisional relaxation we have for the scattering rate [32]

$$R_{\text{sc}} = (\Gamma) \frac{(\Omega/\Gamma)^2}{1 + 4(\Delta_L/\Gamma)^2 + 2(\Omega/\Gamma)^2} \quad (2.14)$$

where the resonant Rabi frequency is defined in terms of the dipole moment and electric field amplitude

$$\Omega := \frac{\mathbf{d} \cdot \mathbf{E}_0}{\hbar}. \quad (2.15)$$

Eq. (2.14) is sometimes written in terms of the *saturation intensity* I_{sat}

$$R_{\text{sc}} = \left(\frac{\Gamma}{2}\right) \frac{(I/I_{\text{sat}})}{1 + 4(\Delta_L/\Gamma)^2 + (I/I_{\text{sat}})} \quad (2.16)$$

where

$$\frac{I}{I_{\text{sat}}} = 2 \left(\frac{\Omega}{\Gamma}\right)^2 \quad (2.17)$$

and

$$I_{\text{sat}} = \frac{c\epsilon_0\Gamma^2\hbar^2}{4|\hat{\epsilon} \cdot \mathbf{d}|^2} = 9.17 \text{ mW/cm}^2 \quad (2.18)$$

for the case of large detuning (i.e., we are using the effective dipole moment defined in Eq. (2.7)) Using Eq. (2.6) we can conveniently express Ω in terms of the well depth

$$\Omega^2 = \frac{2\Delta_L V_0}{\hbar}. \quad (2.19)$$

Using this relationship we can approximate R_{sc} in the large detuning limit $\Delta \gg \Omega$ as

$$R_{\text{sc}} \approx \frac{2\pi\Gamma V_0}{2\Delta_L \hbar}. \quad (2.20)$$

For typical experimental parameters of $V_0 = 0.4E_u$ and $\Delta_L = 2\pi \cdot 30 \text{ GHz}$ $R_{\text{sc}} = 200 \text{ s}^{-1}$ or one event every 5 ms. For the tunneling experiments of Chapter 6, the large acceleration duration was at most $100 \mu\text{s}$ and in this time approximately 2% of the atoms scattered a spontaneous photon.

2.3.4 Amplitude and phase modulation

The amplitude and phase of the optical lattice were controlled using acousto-optic modulators (AOM's). Electro-optic modulators can also be used and are in general much faster than AOM's; however, AOM's have a distinct advantage in that an overall frequency difference between the two beams of the optical

lattice is easily obtained. EOM's can only provide a finite phase shift of a traveling wave while an AOM actually frequency shifts the beam. Piezo driven mirrors can also be used to change the total path length and therefore the phase of the standing wave. However, piezos are limited to finite phase shifts and moreover are orders of magnitude slower than either EOM's or AOM's.

The optical lattice setup with the details of the double-pass configuration are shown in Fig. 2.11. One of the constituent beams of the optical lattice was passed through a single AOM operating at a frequency of 80 MHz. The other was passed twice through an AOM operating at a frequency of 40 ± 5 MHz producing a frequency shift of 80 ± 10 MHz. Therefore, the frequency difference of the beams could be scanned in the range ± 10 MHz, corresponding to a velocity range of ± 100 recoils = ± 3 m/s. The slew rate of the AOM was limited to approximately $1 \text{ MHz}/\mu\text{s}$, which limited the accelerations to below $600,000 \text{ m/s}^2$. The largest acceleration we studied was $20,000 \text{ m/s}^2$. The reason for double-passing the AOM is to minimize the beam deflection as the frequency of the AOM is scanned. Such wide frequency shifts would grossly misalign the beam if done in a single-passed configuration.

Double-passed AOM

The secret to getting good efficiency through a double-passed system is to provide the AOM with a spot small enough to fit through the crystal with a long Rayleigh length (the beam should be as “flat” as possible). The focus of the beam should be centered in the AOM crystal, and one should ideally use a curved mirror with a focal length matched to that of the input lens for the retro-reflection. In our case, we used a lens and a flat mirror placed fairly close together.

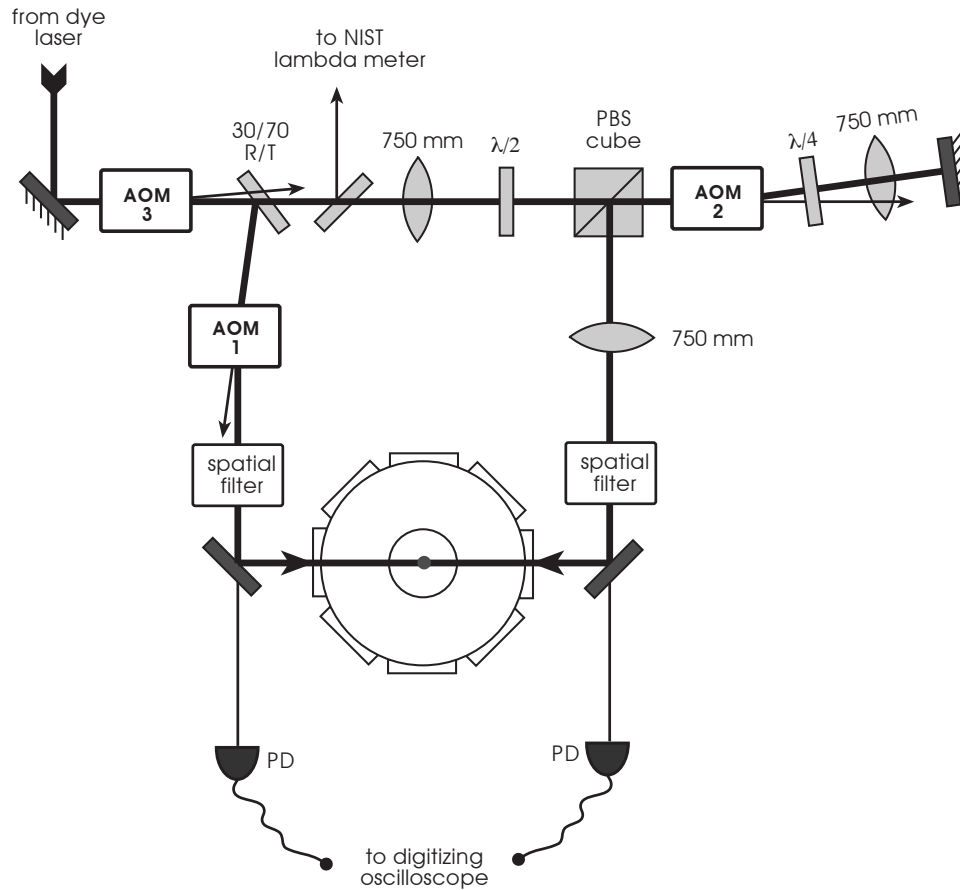


Figure 2.11: Schematic of the optical lattice setup. AOM3 provides global control of the intensity. AOM1 is a single passed 80 MHz AO shifting the beam down by this amount. AOM2 is a double passed 40 MHz AO shifting the beam down by twice its frequency without leading to an appreciable angular deflection.

Characterization of the AOM performance

In order to characterize the phase evolution of the standing wave, we performed a heterodyne measurement using a Michelson interferometer as seen in Fig. 2.12. The intensity of the light striking the photodiode is proportional to the cosine of the integrated phase difference. Therefore, by measuring the beat-note frequency of the photodiode signal, we could determine the exact frequency difference of the two beams $\Delta\nu$ and therefore the velocity of the standing wave:

$$v = \frac{\lambda}{2}\Delta\nu. \quad (2.21)$$

The photodiode signal was captured by a Tektronix TDS 524A digitizing scope and uploaded to a PC where the instantaneous frequency of the signal could be determined. A crude estimate of the instantaneous frequency $\Delta\nu(t)$ was obtained by measuring the zero crossings of the signal. This function was then used as a first guess for a least-squares fitting program that refined the guess further. An example of the beat note signal determined by this fitting routine is shown in Fig. 2.13. This velocity profile was used in a tunneling experiment where the acceleration switches from a low level ($a_{\text{transport}}$) to a higher level (a_{tunnel}) for which the tunneling rate from the first band is large.

For the experiments studying non-exponential decay in Chapter 6, the deviations from exponential decay were predicted to occur in the first few microseconds. For this reason, we had to know precisely what was the behavior of the standing wave velocity at this level. Specifically, we needed to know what the instantaneous acceleration was as a function of time with a resolution of tens of nanoseconds. Since our calculated fit of the frequency difference was limited due to the finite sampling time of the oscilloscope, we decided to determine the response of the double-pass system with a spectrum analyzer.

The logic of this analysis is as follows. A DC voltage V applied to the FM modulation input of the AOM driver produces a constant shift in the

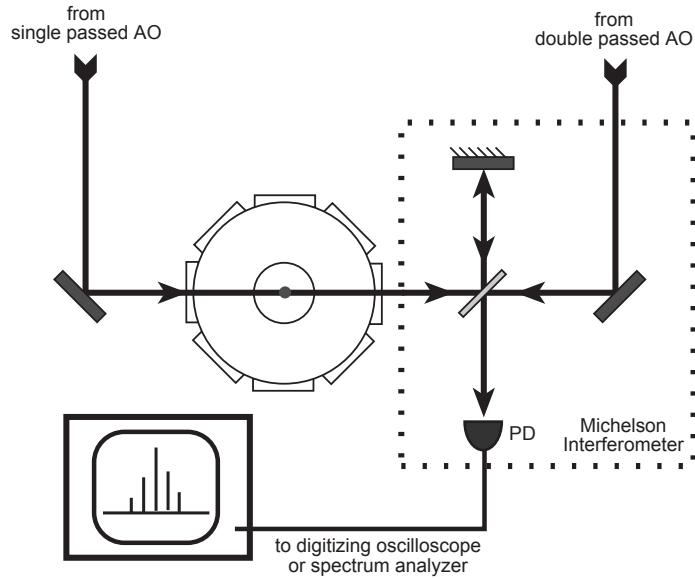


Figure 2.12: Schematic of the Michelson interferometer used to measure the time dependent phase evolution of the standing wave.

frequency $\Delta\omega$ of the double-passed beam and therefore a constant velocity for the standing wave. The light after passing through the AOM has the form

$$\vec{E}(\vec{r}, t) = \vec{E}(\vec{r})e^{i\omega_L t} \cos\left(\omega_0 t + \int_0^t \Delta\omega(V)dt\right), \quad (2.22)$$

where ω_0 is the carrier frequency of the AOM and the frequency shift $\Delta\omega$ is a linear function of the applied voltage V . A time dependent voltage $V(t)$ at the FM input will produce a time dependent frequency shift and therefore a time dependent velocity for the standing wave. In fact, the velocity is simply proportional to the applied voltage $V(t)$. However, at some level the double-passed system should not produce an instantaneous frequency shift exactly proportional to the input voltage because of electronic or optical delay. The limiting factor is the time required for the acoustic wave in the AOM crystal to propagate across the beam diameter. Typically, this time was on the order of 100 ns, as determined by a measurement of the diffracted order intensity

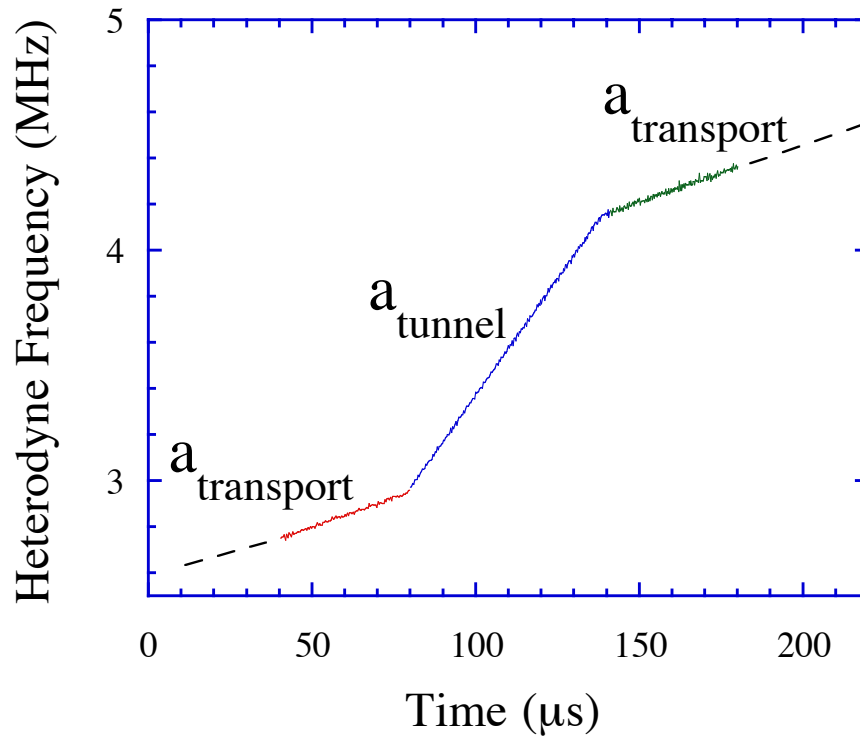


Figure 2.13: Three-stage acceleration process used to study tunneling. This figure displays the beat note frequency of the counter-propagating pair as a function of time determined from a digitized heterodyne signal. The velocity of the standing wave is proportional to this frequency, and therefore the acceleration is proportional to the instantaneous slope. The vertical axis is in units of MHz, and the horizontal axis is in units of μs . During the smaller acceleration the velocity slope is $5.1 \text{ kHz}/\mu\text{s}$ which corresponds to an acceleration of $a_{\text{transport}} = 1500 \text{ m/s}^2$.

response to switching off the RF. As was mentioned before, the slew rate of the voltage-controlled oscillator (VCO) limits the maximum rate of change of the frequency. Therefore, there is some maximum slope of the voltage $V(t)$ (some acceleration) that cannot be followed by the VCO. However, as was said above, the slew rate limit for the acceleration is $600,000 \text{ m/s}^2$, 30 times the largest acceleration we imposed. In order to predict the resulting velocity profile given some control voltage $V(t)$, we must also know the maximum rate of change of the acceleration, the second derivative of $V(t)$. In order to characterize the exact behavior of the standing wave velocity $v(t)$ as a function of an arbitrary input voltage $V(t)$, we measured the response of the velocity to a sinusoidally varying voltage at many different frequencies. In this way, a transfer function was determined which could then be used to reconstruct the actual velocity profile given an arbitrary input voltage.

Our measurement was done in the following way. We applied a sinusoidal signal to the FM input of the VCO of the form

$$V(t) = U_0 \sin(\omega_m t), \quad (2.23)$$

which modulated the frequency of the VCO and produced a first order diffracted spot with an electric field \vec{E}_1 of the form given by Eq. (2.22)

$$\vec{E}_1(\vec{r}, t) = \vec{E}_1(\vec{r}) e^{i\omega_L t} \cos\left(\omega_0 t + \frac{A \Delta\omega}{\omega_m} \cos \omega_m t\right), \quad (2.24)$$

where the DC frequency excursion $\Delta\omega$ is proportional to the amplitude of the input voltage U_0 , and the *attenuation factor* A depends on the frequency ω_m . The DC frequency excursion was measured directly with an EIP 548A microwave frequency counter and found to be

$$\Delta\omega = 40.40 \frac{\text{MHz}}{\text{Volt}} \cdot U_0. \quad (2.25)$$

The frequency-shifted beam was heterodyned with the unshifted zeroth-order beam E_0 passing through the AOM, and the mixed signal was detected with

a photodiode. The photodiode current was of the form

$$I_{\text{photodiode}} \propto E_1^* E_0 \propto \cos \left(\omega_0 t + \frac{A \Delta \omega}{\omega_m} \cos \omega_m t \right). \quad (2.26)$$

We expand the right hand side in terms of ordinary Bessel functions and have

$$I_{\text{photodiode}} = I_0 \sum_{n=-\infty}^{\infty} J_n \left(\frac{A \Delta \omega}{\omega_m} \right) \cos [(\omega_0 + n \omega_m) t]. \quad (2.27)$$

This current was injected into a spectrum analyzer that mixes it with a local oscillator and displays the *power* in dBm. In order to extract the attenuation factor A , we must measure the ratio of two sideband amplitudes. The difference in power of the n^{th} sideband from the carrier is

$$P_n - P_0 = 20 \log_{10} \left[\frac{J_n(\lambda)}{J_0(\lambda)} \right] \quad (2.28)$$

where $\lambda = \frac{A \Delta \omega}{\omega_m}$. We solved Eq. (2.28) for λ at various values of the modulation frequency. Knowing the amplitude of the control voltage U_0 , the proportionality constant for the DC frequency excursion $\Delta \omega$ (given by Eq. (2.25)), and the value of the modulation frequency, we were able to determine the attenuation function $A(\omega_m)$. The results of this measurement are shown in Fig. 2.14. Since the size of the first order sideband scales inversely with the modulation frequency, at very high frequencies, the sideband peak becomes buried in the noise of the spectrum analyzer. At this point, the determination of A is difficult, and the modulation amplitude must be increased to proceed to higher frequencies. In this figure, six sets of data are shown for six different values of the control voltage amplitude. Our assumption is that A depends only on the modulation frequency and not on the modulation amplitude, and Fig. 2.14 confirms this assumption. With the transfer function A determined, we were able to reconstruct the actual velocity profile given an arbitrary input voltage. Fig. 2.15 shows an ideal trapezoidal velocity function and the actual standing wave velocity calculated by expanding the ideal function into a Fourier sum,

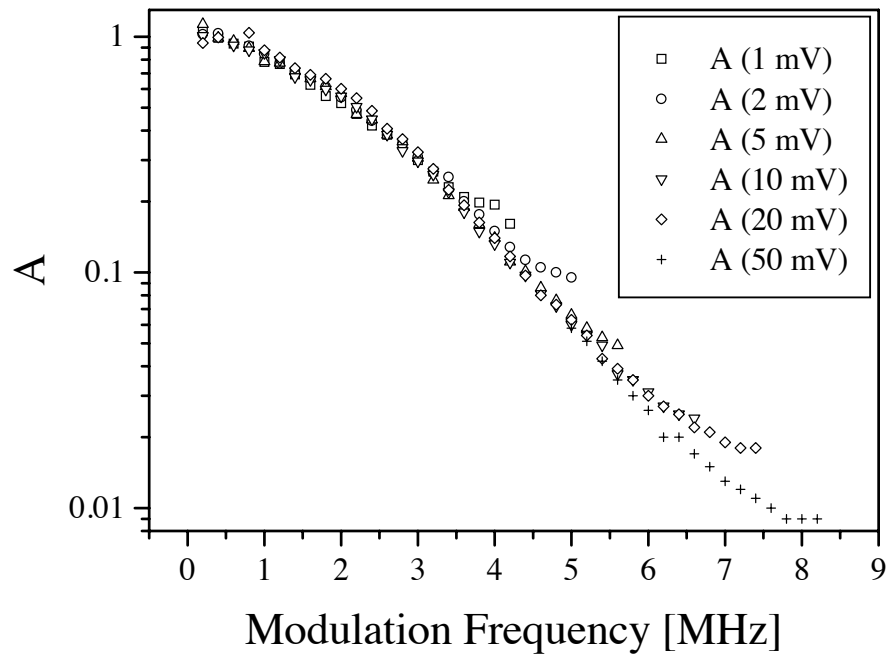


Figure 2.14: The AOM transfer function $A(\omega_m)$ measured for six different modulation amplitudes. Since the size of the first order sideband scales inversely with the modulation frequency, at very high frequencies, the sideband peak becomes buried in the noise of the spectrum analyzer and the value of A is overestimated.

multiplying each term with the corresponding value of A , and then resummation the series. The thin line is the ideal function. The dashed line is the ideal function with only 29 terms, and the thick line is the resulting velocity profile. By taking the derivative of this function, we can calculate the instantaneous acceleration as a function of time with a resolution of a few tens of nanoseconds. This derivative is shown in Fig. 2.16, and we see that the standing wave acceleration switches from zero to 80% of the total within 220 ns.

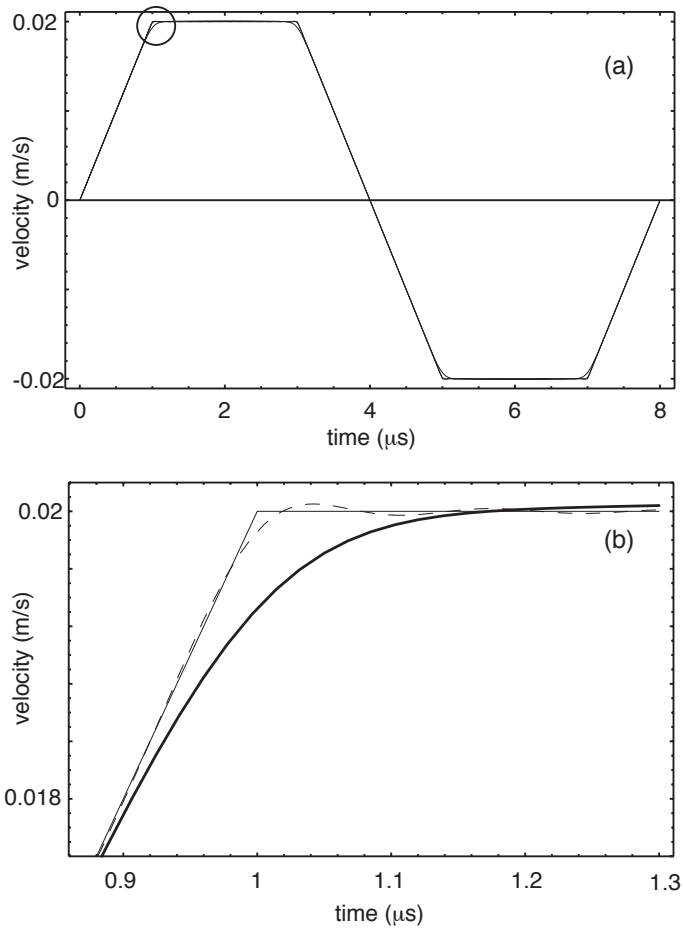


Figure 2.15: The resulting standing wave velocity response to an ideal trapezoidal profile. This velocity profile was calculated by expanding the ideal function into a Fourier sum, multiplying each term with the corresponding value of A , and then resumming the series. Only 29 terms of the infinite sum were kept. The thin line is the ideal function. The dashed line is the ideal sum with only 29 terms, and the thick line is the resulting velocity profile.

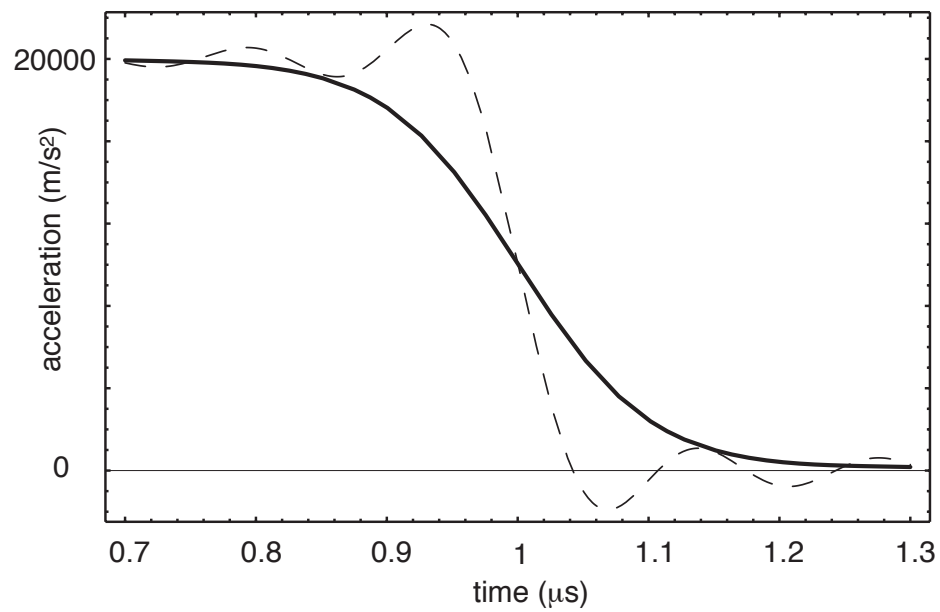


Figure 2.16: A plot of the standing wave acceleration response to an abrupt switch. This graph was obtained by taking the derivative of the results found in Fig. 2.15. The dashed line is the ideal acceleration with only 29 Fourier components kept, and the thick line is the resulting acceleration profile. From this graph, the acceleration is seen to change by 80% of the total within 220 ns.

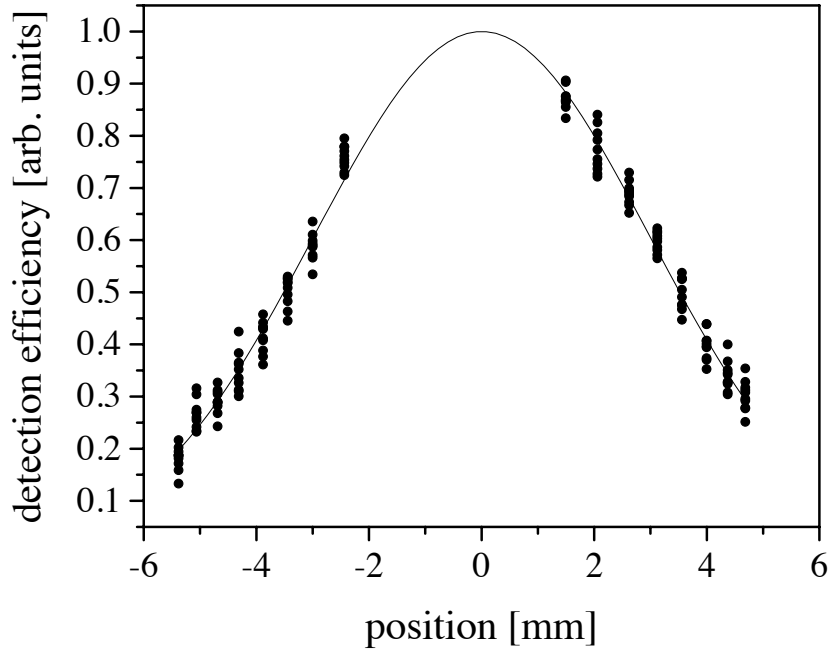


Figure 2.17: A typical detection efficiency envelope of the freezing molasses. The horizontal scale denotes the distance from the center of the MOT. The line represents a gaussian fit which was then used to scale the one dimensional lineshapes before the accelerated peaks were integrated and the survival probability was determined.

2.4 Detection and measurement

As was described in Section 2.1, after the free drift the resonant light was turned on to produce a viscous, optical molasses that halted the ballistic motion of the atoms and provide spontaneously scattered resonant light for detection. The determination of the survival probability of the fundamental band was accomplished by dividing the integrated fluorescence of the survivor peak by the total fluorescence for the two accelerated peaks.

Although the atomic cloud expansion in the optical molasses can be made (with a careful optical alignment and a balancing of the beam intensities) to be spherically symmetric and slow compared to the exposure time,

the MOT beams have a Gaussian profile with a finite size (typically 2 cm in diameter). For this reason, the molasses intensity decreases with the distance from the center of the chamber, and therefore the atomic fluorescence will also decrease. In order to correct for this position-dependent fluorescence, we imaged the atoms with the largest intensity possible (trying to reach the saturation intensity across the cloud), and we characterized the fluorescence as a function of position. This characterization was done by launching a certain fraction of the atoms to a particular velocity so that it would travel to a particular position during a fixed drift time and then recording the integrated fluorescence normalized by the fluorescence of the subset not accelerated. The fixed drift time insured that the launched subset was the same size for each measurement, and the normalization reduced the error introduced by shot-to-shot fluctuations in the total number of atoms loaded in the MOT. In this way, we obtained an empirical measure of the detection efficiency averaged over the size of a small launched distribution. The one-dimensional fluorescent profiles were then scaled by this function before the integration of the peaks and the determination of the survival probability. An example of a typical detection efficiency envelope is shown in Fig. 2.17.

Since the survival probability information is contained in the velocity distribution of the ensemble, other methods for velocimetry could have been used. The group of Christophe Salomon in Paris studying optical lattices used Doppler shifts of stimulated Raman transitions for velocity detection [22, 37]. This method has a high detection efficiency and a subrecoil velocity resolution; however, it is complicated to implement and only a single velocity class can be measured at a time, not the entire distribution. The method of recoil induced resonances provides information about the entire distribution but has a much lower quantum efficiency [38].

Chapter 3

The time-independent cosine potential

In this chapter we consider the behavior of atoms in the presence of a one-dimensional time-independent optical lattice. We will first review some results of the theoretical study of the cosine potential and then present the experimental measurements of the energy distribution and the spectral characteristics of this system.

3.1 Transformation to scaled quantities

Throughout this dissertation, every physical quantity will be measured either in MKS units or in “natural units.” It will be clear, or made so, which units are being used in each situation. The reason for this seemingly schizophrenic practice is that experimental measurements are usually made in MKS units, while expressing quantities such as momentum or position in natural units greatly simplifies the notation and facilitates the formulation of computer simulations [39, 30] as well as the analytic, mathematical analysis. Moreover, the natural units reflect the natural scales of the system.

We start with the effective Hamiltonian, defined in Chapter 1,

$$H_{\text{lab}}(x, p) = \frac{p^2}{2M} - V_0 \cos(2k_L x), \quad (3.1)$$

and we define our new units by the following relationships. The parameters measured in MKS are unprimed and their counterpart measured in the natural

units are primed:

$$H' = \frac{H}{E_u} \quad (3.2)$$

$$V'_0 = \frac{V_0}{E_u} \quad (3.3)$$

$$t' = \frac{t}{t_u} \quad (3.4)$$

$$p' = \frac{p}{p_u} \quad (3.5)$$

$$x' = \frac{x}{x_u}, \quad (3.6)$$

where

$$E_u = 8\hbar\omega_r = h \cdot 200 \text{ kHz} \quad (3.7)$$

$$t_u = (8\omega_r)^{-1} = 0.795\mu\text{s} \quad (3.8)$$

$$p_u = 2\hbar k_L = M \cdot 0.0589 \text{ m/s} \quad (3.9)$$

$$x_u = (2k_L)^{-1} = 47 \text{ nm}. \quad (3.10)$$

The unit of momentum $2\hbar k_L$ is twice the momentum of a single photon, and $1/2k_L$ is the periodicity of the potential l divided by 2π . The recoil energy $\hbar\omega_r$ is defined as the kinetic energy of an atom moving with the momentum imparted to it by the emission of a single photon of resonant light,

$$\omega_r = \frac{\hbar k_L^2}{2M} = 2\pi \cdot 25.003 \text{ kHz}, \quad (3.11)$$

where $k_L = 2\pi/\lambda$, and M is the atomic mass. Another useful quantity is the scaling for an acceleration, defined by

$$a' = \frac{a}{a_u} \quad (3.12)$$

$$a_u = x_u/t_u^2 = \frac{47\text{nm}}{0.795\mu\text{s}^2} = 74.0357 \text{ km/s}^2. \quad (3.13)$$

With this change of units, the Hamiltonian of Eq. (3.1) becomes, after dropping the primes,

$$H(x, p) = \frac{p^2}{2} - V_0 \cos(x), \quad (3.14)$$

and the Schrödinger equation becomes

$$i\frac{\partial}{\partial t}|\psi\rangle = H|\psi\rangle, \quad (3.15)$$

where the commutator is now

$$[x, p] = i. \quad (3.16)$$

3.2 Classical treatment: the pendulum

For the low temperatures achieved with laser cooling the atoms are moving at only a few recoil velocities so that their de Broglie wavelength is on the order of the lattice periodicity π/k_L . If an atom is moving at a velocity corresponding to N double photon recoils then

$$\lambda_{dB} = h/p = h/2N\hbar k_L = l/N \quad (3.17)$$

Roughly speaking, when the particle has a de Broglie wavelength that is large compared with the feature size of the potential, it can no longer be approximated as a classical particle and its wavelike nature will become apparent. Although the atoms are moving slowly and therefore must be treated quantum mechanically, it is nonetheless useful to recall the results of a classical treatment of this problem.

We take Eq. (3.14)

$$H(x, p) = \frac{p^2}{2} - V_0 \cos(x) \quad (3.18)$$

and apply Hamilton's equations, with the result

$$\dot{p} = -\frac{\partial H}{\partial x} = -V_0 \sin(x) \quad (3.19)$$

$$\dot{x} = \frac{\partial H}{\partial p} = p. \quad (3.20)$$

These equations can be rewritten as the second order differential equation

$$\ddot{x} + V_0 \sin(x) = 0. \quad (3.21)$$

This equation is equivalent to the equation of motion for a pendulum. It should be noted here that it is precisely this mathematical equivalence that has allowed the experimental realization of the δ -kicked rotor, a paradigm system for the study of quantum chaos [40, 41, 42]. At first it might seem that a

particle moving linearly in a periodic potential is fundamentally different from a rotor since, unlike the particle, a rotor is precisely where it started after a rotation of 2π . However, this difference is dissolved once we define a winding number for the rotor. For the quantum rotor, there exists no mechanism which would break the aforementioned symmetry, and therefore the situation is slightly different (see Section 3.3).

Since the Hamiltonian is independent of time, the total energy of the system is a constant and the system will move in phase space along paths of constant E . Solving Eq. (3.18) with $H = E$ for p , we have

$$p = \pm\sqrt{2[E + V_0 \cos(x)]}. \quad (3.22)$$

A plot of the phase portrait is shown in Fig 3.1. For $E < V_0$ the motion is oscillatory in x and bounded between $\pm x_{\text{tp}}$ where

$$\cos(x_{\text{tp}}) = -\frac{E}{V_0}. \quad (3.23)$$

For small values of E , the amplitude of the excursion x_{tp} is small, and we can approximate $\sin(x)$ with just x . In this case, we have a harmonic oscillator

$$\ddot{x}(t) + V_0 x(t) = 0 \quad (3.24)$$

with a frequency

$$\nu_{\text{HO}} = \frac{\sqrt{V_0}}{2\pi}. \quad (3.25)$$

Typically, our experiments were performed with well depths on the order of $V_0 = 0.4$, which gives a frequency of $\nu_{\text{HO}} = 0.1$. Remembering from Section 3.1 that our unit of time is $t_u = 0.795\mu\text{s}$, we find that ν_{HO} is approximately 130 kHz in this regime.

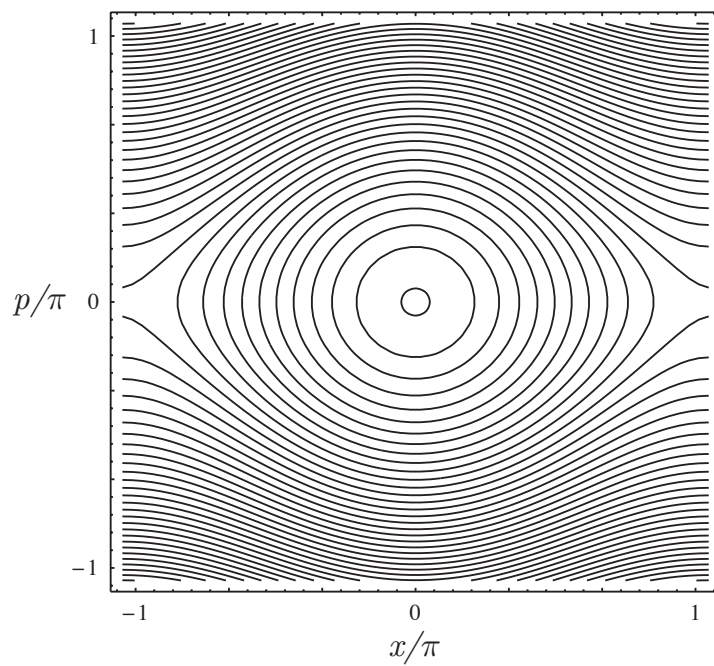


Figure 3.1: Phase portrait for a classical pendulum. The contours shown are trajectories of constant energy, given by the relation $p = \pm\sqrt{2[E + V_0 \cos(x)]}$. This portrait, like the potential, is periodic in x but not in p .

3.3 The quantum pendulum: Mathieu's equation

The problem of finding the energy eigenstates of H , solving $H|\psi\rangle = E|\psi\rangle$, is simply Mathieu's equation, whose properties and solutions can be found in most handbooks of mathematical functions [43]. We take Eq. (3.14) and, to help with the identification, we invert ($V_0 \rightarrow -V_0$) and shift the potential so that the minima are at zero. Then, the Schrödinger equation becomes

$$\left[\frac{1}{2} \frac{\partial^2}{\partial x^2} + (E - V_0) - V_0 \cos(x) \right] y(x) = 0, \quad (3.26)$$

where we have taken

$$\langle x | \psi(x, t) \rangle = e^{-iEt} y(x). \quad (3.27)$$

By making the identifications

$$a = 8(E - V_0) \quad (3.28)$$

$$q = 4V_0 \quad (3.29)$$

$$2z = x, \quad (3.30)$$

Eq. (3.26) can be written in the “canonical form” cited by Abramowitz and Stegun [43]:

$$\frac{\partial^2 y}{\partial z^2} + (a - 2q \cos 2z)y = 0. \quad (3.31)$$

As will be shown in Section 3.5 the solutions $y(x)$ have the form

$$y(z) = e^{ikz} w(z) \quad (3.32)$$

where $w(z)$ is π periodic. *Mathematica* has in its library of mathematical functions a set of routines (for example `MathieuCharacteristicA`) for calculating the characteristic values a (which correspond to the energies) for a given characteristic exponent k and well depth q [44]. Using these routines, the dispersion curves (the energy a versus the exponent k) and the band edges (the energy evaluated at the band edge $k/k_L = \pm 1$ as a function of the well

depth q) are calculated and plotted in Figs. 3.2 and 3.3. For comparison with the real potential

$$V(x) = \cos(2k_L x) \quad (3.33)$$

the quasimomentum k is displayed in units of k_L .

From Fig. 3.2 one can see that the allowed energy bands approach the linearly spaced harmonic-oscillator states in the limit of large well depth. Although we have here at our disposal the solutions to the time-independent problem, we will nevertheless develop the approach to calculating these solutions in Section 3.7 since this will elucidate the structure of these solutions and will prove useful when we consider the time-dependent problems of the following chapters.

3.4 The linear periodic potential and the quantum rotor

Although a classical particle moving linearly in a periodic potential is not fundamentally different from a classical rotor, the situation in quantum mechanics is notably different. The fact that there is no mechanism which breaks the rotational periodicity, that a rotor is precisely where it started after a rotation by 2π , leads to a discrete point set p -space for the rotor. More specifically, the condition

$$\psi(x) = \psi(x + 2\pi) \quad (3.34)$$

forces a quantization condition of the characteristic exponent k appearing in the solutions Eq. (3.32)

$$k = 0, \pm 1, \pm 2, \dots \quad (3.35)$$

while for the optical lattice, the range of k is continuous. In both cases, the potential only couples states on a *momentum ladder* where the ladder spacing is $2k_L$; however, for the optical lattice, there are many momentum ladders while for the rotor there is only one, centered at $p = 0$. As was mentioned

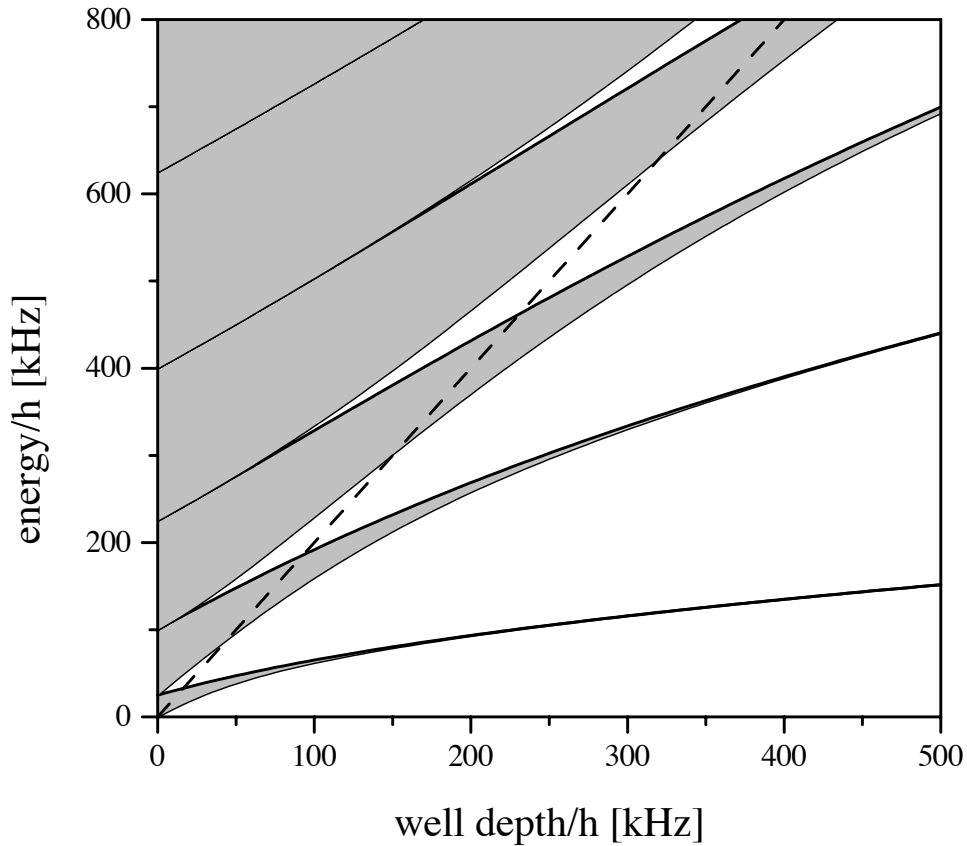


Figure 3.2: Using Mathematica's built-in routine for finding the characteristic values of Mathieu's equation, the band edges are calculated and plotted as a function of the well depth V_0 . To facilitate the use of this figure with experimental quantities, both axes are scaled by h so that they appear in units of s^{-1} . The bands of allowed energies are colored grey and the band gaps are white. The dotted line represents the top of the well at $2V_0$. Notice that the average spacing between bands approaches a linear (harmonic oscillator) spacing in the limit of large well depth

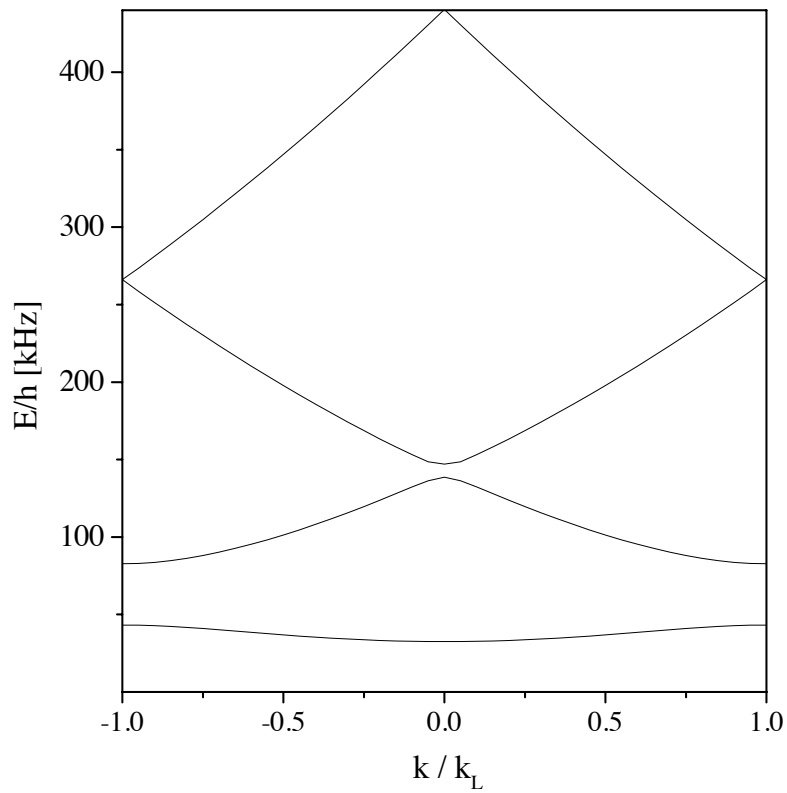


Figure 3.3: Using Mathematica's built-in routine for finding the characteristic values of Mathieu's equation, the energy as a function of k is calculated and plotted in the first Brillouin zone, for a well depth of $V_0 = 0.2 = h \cdot 40\text{kHz}$. For an optical lattice, $\cos(2k_L x)$, the first Brillouin zone extends from $-k_L$ to $+k_L$.

earlier, the δ -kicked rotor has been experimentally realized and studied using a pulsed optical lattice [40, 41, 42, 45]. Since all values of k are admitted for the optical lattice, the quantum resonances observed by Moore *et al.* in the optical lattice realization for the quantum δ -kicked rotor possessed a very different signature than that predicted for states restricted to lie just on the ladder centered at $p = 0$ [45].

3.5 Bloch's Analysis

In his seminal paper on the theory of electronic motion in crystals, Felix Bloch presented a number of fundamental results pertaining to a general periodic potential [11]. The first result, the so-called “Bloch’s theorem”, states that if ψ is a solution of the time-independent Schrödinger equation with a periodic potential $V(x) = V(x + a)$, then ψ can be written as a plane wave times a function with the same periodicity as V . This theorem, which was proved in three dimensions, is equivalent to Floquet’s theorem concerning the solution of periodic differential equations in one dimension presented in 1883 [46].

3.5.1 Bloch’s Theorem

We present here a proof of Bloch’s theorem in one dimension, which is useful for understanding the form of solutions for spatially periodic as well as temporally periodic potentials, as we will see in Chapter 4.

First, we define a translation operator T_a such that

$$T_a\psi(x) = \psi(x + a). \quad (3.36)$$

Now, we apply T_a to the Schrödinger equation.

$$T_a \left(\frac{p^2}{2M} + V(x) \right) \psi = T_a(E\psi) \quad (3.37)$$

Since the potential is periodic (with period a) and the momentum is unchanged by a shift in the coordinates, H is unchanged by the application of T_a , and Eq. (3.37) becomes

$$\left(\frac{p^2}{2M} + V(x) \right) (T_a\psi) = E (T_a\psi) \quad (3.38)$$

Thus, if ψ is a solution (an eigenvector of H) then so is $T_a\psi$. Moreover, it has the same eigenvalue E , and therefore T_a and H must have simultaneous

eigenvalues. Let λ be the eigenvalue of T_a

$$T_a\psi(x) = \lambda\psi(x) = \psi(x+a). \quad (3.39)$$

Now we multiply both sides of (3.39) by $e^{-iK(x+a)}$

$$e^{-iKx}e^{-iKa}\lambda\psi(x) = e^{-iK(x+a)}\psi(x+a) \quad (3.40)$$

and choose K so that $\lambda e^{-iKa} = 1$. Here $|\lambda|^2 = 1$ since T_a is unitary. Then we have

$$e^{-iKx}\psi(x) = e^{-iK(x+a)}\psi(x+a) \equiv u_K(x), \quad (3.41)$$

where we see that $u_K(x)$ is a periodic and, by definition,

$$\psi(x) = e^{iKx}u_K(x). \quad (3.42)$$

From this result, we see that Ka is defined up to an integer multiple of 2π . If we let $K = k + \frac{2\pi}{a}n$ then we can write Eq. (3.42) as

$$\psi(x) = e^{ikx}u_{n,k}(x), \quad (3.43)$$

where $u_{n,k}(x)$ is still an a -periodic function and the quasimomentum k is now restricted to the interval $[\pi/a, -\pi/a]$. The functions $u_{n,k}(x)$ are real and symmetric, as we shall see in Section 3.7.

3.5.2 Properties of Bloch states

In addition to showing the form of the solutions for a periodic potential (referred to as Bloch states), Bloch also showed that these solutions had a number of interesting properties. Many of his results were later reviewed and proved in general by Jones and Zener [13]. A thorough discussion of this subject is provided by Ashcroft and Mermin [47]. We list here a few of the most important properties of the Bloch states.

Symmetries of Bloch states

As we saw in Section 3.5.1, Bloch states have the form

$$\psi_{n,k}(x) = \langle x|n, k\rangle = e^{ikx}u_{n,k}(x), \quad (3.44)$$

where n is a discrete band index and the quasimomentum k is a continuous variable. These states are energy eigenstates satisfying

$$H_0|n, k\rangle = E_n(k)|n, k\rangle, \quad (3.45)$$

where

$$|n, k + 2\pi/a\rangle = |n, k\rangle \quad (3.46)$$

$$E_n(k + 2\pi/a) = E_n(k). \quad (3.47)$$

The Bloch states have the additional property [13]

$$\psi_{n,k}^*(x) = \psi_{n,-k}(x). \quad (3.48)$$

Because of this redundancy, k is typically restricted to one Brillouin zone $k \in [\pi/a, -\pi/a]$ where the end points of this interval are equivalent. These functions are orthogonal,

$$\int_{-\infty}^{+\infty} \psi_{n',k'}\psi_{n,k} dx \propto \frac{1}{2\pi}\delta(k' - k)\delta_{n',n}, \quad (3.49)$$

and usually taken to be normalized over a unit cell so that

$$\int_{-a/2}^{+a/2} \psi_{n',k}\psi_{n,k} dx = \delta_{n',n}. \quad (3.50)$$

Velocity of a Bloch particle

Another property of interest is the average velocity of a particle in a Bloch state $\psi_{n,k}$. It was first shown by Bloch and then proved in general by Jones and Zener that this quantity is related to the energy of the state by

$$\langle v_n(k) \rangle = \frac{1}{\hbar} \frac{\partial E_n(k)}{\partial k}. \quad (3.51)$$

This result is remarkable in that it is identical to that for a free particle, remembering that $\hbar k$ is the momentum. It also implies that there exist states whose energy is well below the potential energy maxima; these states would therefore be bound classically but quantum mechanically would move ballistically without any change in their mean velocity. This phenomenon, known as *Bloch tunneling*, will be discussed in the following section.

The original derivation of Eq. (3.51) was performed in three dimensions; however, for simplicity we will restrict our attention to the one-dimensional case [11, 13]. The velocity is defined as the time derivative of the expectation of the position, and it can be shown that this is equal to the integrated probability current divided by the normalization of the state provided that ψ “vanish sufficiently fast at infinity” [48]. We have then

$$\langle v_n(k) \rangle = \frac{d}{dt} \langle x \rangle = \int j dx / \int \rho dx \quad (3.52)$$

where the probability current j and the probability density ρ are given by

$$j = \frac{\hbar}{2Mi} \left[\psi^* \frac{\partial}{\partial x} \psi - \psi \frac{\partial}{\partial x} \psi^* \right] \quad (3.53)$$

$$\rho = \psi^* \psi. \quad (3.54)$$

Implicit in this use of the expectation value of x as well as the relationship between the velocity and probability current is the assumption that ψ is normalizable. Strictly speaking, a Bloch wave function or even a simple plane wave violates this condition. It is therefore assumed that the Bloch wave function is the limiting form of a finite but broad wave packet. This point is relevant since much of the controversy regarding the theoretical prediction of the Wannier-Stark ladder was related to the use of the Born-von Karman periodic boundary conditions, a device employed to justify the use of plane-wave functions for finite crystals. These issues are addressed in Chapter 5. Following Jones and Zener we prove Eq. (3.51) by first differentiating the Schrödinger

equation with respect to k . To simplify the notation, we define the operator L_k

$$L_k = \frac{p^2}{2M} + E_k - V. \quad (3.55)$$

Differentiating $L_k\psi_k = 0$ with respect to k gives

$$\frac{\partial E_k}{\partial k}\psi_k + L_k(ix)\psi_k + L_k \left[e^{ikx} \frac{\partial u_k}{\partial k} \right] = 0, \quad (3.56)$$

where we are suppressing the band index n . The second term is

$$L_k(ix)\psi_k = ixL_k\psi_k + [L_k, ix]\psi_k \quad (3.57)$$

$$= \frac{i\hbar^2}{M} \frac{\partial}{\partial x} \psi_k, \quad (3.58)$$

where we have used that $L_k\psi_k = 0$. If we now premultiply by ψ_k^* and integrate over one lattice period, we have

$$\frac{\partial E_k}{\partial k} \int_{-a/2}^{a/2} \psi_k^* \psi_k dx + \frac{i\hbar^2}{M} \int_{-a/2}^{a/2} \psi_k^* \frac{\partial}{\partial x} \psi_k dx + \int_{-a/2}^{a/2} \psi_k^* L_k \left[e^{ikx} \frac{\partial u_k}{\partial k} \right] dx = 0, \quad (3.59)$$

where we integrate by parts the last term twice to obtain

$$\int \psi_k^* L_k \left[e^{ikx} \frac{\partial u_k}{\partial k} \right] dx = \int \left[e^{ikx} \frac{\partial u_k}{\partial k} \right] L_k \psi_k^* dx. \quad (3.60)$$

The boundary terms vanish because the integrands are periodic over the interval of integration. Since L_k is a real operator, $L_k\psi_k^* = 0$, and therefore this last term vanishes identically. Finally, the second term of Eq. (3.59) can be shown using integration by parts to be equivalent to the current:

$$\int \psi_k^* \frac{\partial}{\partial x} \psi_k dx = \frac{1}{2} \int \left(\psi_k^* \frac{\partial}{\partial x} \psi_k - \psi_k \frac{\partial}{\partial x} \psi_k^* \right) dx. \quad (3.61)$$

Using this relation, we have finally the desired result

$$\frac{\partial E_k}{\partial k} = \hbar \int_{-a/2}^{a/2} j(x) dx \quad / \quad \int_{-a/2}^{a/2} \rho(x) dx \quad (3.62)$$

for which Eq. (3.51) is an immediate consequence, since both of these integrands are periodic over the range of integration. In fact, the current is *independent* of x . This is because the Bloch wave functions are stationary states $\frac{\partial \rho}{\partial t} = 0$. The generalized, three-dimensional probability density and current satisfy a continuity equation of the form

$$\frac{\partial \rho}{\partial t} + \nabla \cdot \mathbf{j} = 0. \quad (3.63)$$

Therefore, a general, one-dimensional stationary state has a constant current independent of position.

Bloch Tunneling

As was mentioned before, an immediate consequence of Eq. (3.51) is that there exist states whose energy is well below the potential energy maxima and therefore would be bound classically but which propagate forever without any change in their mean velocity. This behavior results in a phenomenon known as Bloch tunneling, the ballistic spreading of an initially localized wave packet.

It is well known that the peak of a spatially localized, Gaussian wave packet in free space will move at the group velocity, and its width will grow linearly in time according to

$$(\Delta x)_t^2 = (\Delta x)_0^2 \left[1 + \frac{\hbar^2 t^2}{4(\Delta x)_0^4 M^2} \right], \quad (3.64)$$

so that for long times and/or small initial widths,

$$(\Delta x)_t \simeq t \frac{\Delta p}{M} = t \Delta v, \quad (3.65)$$

where we have assumed an initially minimum uncertainty initial wave packet:

$$(\Delta x)_0 (\Delta p)_0 = \frac{\hbar}{2}. \quad (3.66)$$

Since we saw in Section 3.5.2 that each Bloch state evolves essentially as a free particle with an associated average velocity given by Eq. (3.51),

$$\langle v_n(k) \rangle = \frac{1}{\hbar} \frac{\partial E_n(k)}{\partial k}, \quad (3.67)$$

a localized superposition of Bloch states will also spread in x according to Eq. (3.65). The only difference between the free particle case and this case is the form of E_k . From Fig. 3.2 it is clear that the widths of the bands all decrease monotonically with increasing V_0 . In the limit of large well depth V_0 , the states at the bottom of the potential are localized, experiencing only the quadratic term of the cosine. The bands are flattened out into discrete harmonic oscillator-like states. In this limit, v_k clearly approaches zero. However, in the limit of shallow well depth the bands essentially follow the free particle energies deviating only at the band edges and as a result, an initially localized wave packet will spread ballistically. This phenomenon of Bloch tunneling is intimately related to the the width (and curvature) of the band, which gives a measure of the effective lifetime of a localized wave packet.

To obtain an estimate of the rate of spreading in the shallow-well-depth limit, we can approximate the dispersion curve with the quadratic, free-particle energy. In Section 3.7.1 we find that this approximation is valid to second order in V_0 except at the band edges where a gap proportional to V_0 forms. A minimum-uncertainty wave packet prepared in the first band of an optical lattice would have a width in momentum of

$$\Delta p = 2\hbar k_L \quad (3.68)$$

where

$$\Delta p \Delta x = \hbar/2. \quad (3.69)$$

This wave packet would spread according to Eq. (3.65) at a rate given by the double-photon-recoil velocity (see Section 3.1)

$$\Delta v = \frac{2\hbar k_L}{M} = p_u/M = 0.0589 \text{ m/s}. \quad (3.70)$$

The wave packet spreading expressed in units of the lattice period $\pi/k_L = 294.5$ nm is

$$(\Delta x)_t = 200 \text{ periods/ms.} \quad (3.71)$$

Although the amount of spreading during one millisecond corresponds to an increase of 2500 from the initial size, the final width is still quite small, only $59 \mu\text{m}$. Observing such spreading would have been difficult in our system since our interaction times were limited to about 1 ms, and our spatial resolution was $63 \mu\text{m}$. Aside from direct imaging, there exist other methods for measuring the position spread of an atomic wave packet. One method relies on the fact that the Bragg scattering cross section depends on the atomic position spread, referred to as the Debye-Waller factor [49].

Response of a Bloch particle to a uniform field: Bloch oscillations

In addition to investigating the strictly periodic potential, Bloch considered the response of an electron in a lattice to the application of an external, uniform electric field. Since the field breaks the symmetry of the potential, the Bloch wave functions are no longer eigenstates. Nevertheless, one can still use them as a basis set, and it can be shown that the effect of the external field is to produce a translation in k of constant velocity. This result was proved by Bloch in the tight-binding limit and then proved in general by Jones and Zener, given that transitions to higher bands are negligible. A striking consequence of this result is that particles are predicted to *oscillate* in space rather than conduct (accelerate uniformly) in response to the external field. Since E_k is periodic in k , the velocity is also periodic, and a constant translation of k produces a time-dependent oscillation of the velocity. These oscillations, termed “Bloch oscillations,” and their spectral signature, called the “Wannier-Stark ladder,” are the subject of Chapter 5.

The wave equation for a Bloch particle in a uniform field is

$$i\hbar \frac{\partial}{\partial t} \Psi = (H_0 - Fx)\Psi, \quad (3.72)$$

where H_0 is the unperturbed, 2π -periodic Hamiltonian. We write Ψ as a linear superposition of Bloch states,

$$\Psi = \sum_n \int_{-\pi/a}^{\pi/a} g_n(k, t) \psi_{n,k} dk, \quad (3.73)$$

where $\psi_{n,k} = e^{ikx} u_{n,k}(x)$. What we want to show is that the function $|g_n(k, t)|^2$ satisfies the advection equation,

$$\left(\hbar \frac{\partial}{\partial t} + F \frac{\partial}{\partial k} \right) |g_n(k, t)|^2 = 0, \quad (3.74)$$

which would mean that

$$|g_n(k, t)|^2 = G(\hbar k - Ft), \quad (3.75)$$

where G is an arbitrary function of its argument. In this case, each piece of the superposition in Eq. (3.73) would move through k space with a uniform velocity F/\hbar .

Following Jones and Zener we project out the evolution of one component of Ψ by premultiplying the wave equation Eq. (3.72) by $\psi_{n',k'}$ and integrating over x . Using the orthonormal property of the Bloch functions, Eqs. (3.50) and (3.49), as well as the fact that they are eigenstates of H_0 we have

$$i\hbar \frac{\partial g_{n'}(k', t)}{\partial t} = E_{n',k'} g_{n'}(k', t) - F \langle \psi_{n',k'} | x | \Psi \rangle. \quad (3.76)$$

In the last term, the product $x\Psi$ can be cleverly rewritten as

$$x\Psi = \sum_n \int dk \left[-i \frac{\partial}{\partial k} (e^{ikx} u g) + i \frac{\partial u}{\partial k} e^{ikx} g + i \frac{\partial g}{\partial k} e^{ikx} u \right] \quad (3.77)$$

where the first term is zero since $\psi_{n,k+2\pi/a} = \psi_{n,k}$. The orthogonality condition projects out the value of the integrands at k' and kills all but one sum over n .

Since all the k 's are equal, we will suppress this variable, and to save ink, we will exchange the indices n and n' . Eq. (3.76) then becomes

$$\left(\hbar\frac{\partial}{\partial t} + F\frac{\partial}{\partial k}\right)g_n = -iE_n g_n - F\sum_{n'}\langle u_n|\frac{\partial}{\partial k}|u_{n'}\rangle g_{n'}. \quad (3.78)$$

To simplify this equation further, we will use both the fact that the eigenenergies are real and the following property of the last term. By differentiating the orthogonality condition Eq. (3.49) by k we see that

$$\langle u_n|\frac{\partial}{\partial k}|u_{n'}\rangle^* = -\langle u_{n'}|\frac{\partial}{\partial k}|u_n\rangle. \quad (3.79)$$

Now we multiply Eq. (3.78) on the left by g_n^* and add the resulting equation to its complex conjugate. We have

$$\left(\hbar\frac{\partial}{\partial t} + F\frac{\partial}{\partial k}\right)|g_n|^2 = -F\sum_{n'}(Z_{n,n'} - Z_{n',n}) \quad (3.80)$$

where

$$Z_{n,n'} = \langle u_n|\frac{\partial}{\partial k}|u_{n'}\rangle g_{n'} g_n^*. \quad (3.81)$$

If we introduce a sum over n , the right hand side vanishes and we arrive at the advection equation

$$\left(\hbar\frac{\partial}{\partial t} + F\frac{\partial}{\partial k}\right)\sum_n |g_n|^2 = 0. \quad (3.82)$$

If we now assume that transitions to higher bands are negligible, a particle initially in the lowest band will remain there, and because all the g_n are zero except g_1 , we have finally the desired result that

$$|g_1(k, t)|^2 = G(\hbar k - Ft). \quad (3.83)$$

where G is an arbitrary function of its argument. We note here that just as we found for the velocity of the Bloch particle, this result, that the applied force produces a constant translation in k , is identical to the result for a free

particle, $\dot{p} = F$. This is because the quasimomentum k truly plays the role of a *free particle* momentum in that it is the new preserved quantity resulting from translational invariance, albeit with a discrete rather than a continuous symmetry.

The effective mass of a Bloch particle

Although the external field dramatically modifies the behavior of the solutions and the dispersion relation between E and k , Jones and Zener state that Eq. (3.51) relating the velocity and energy of the particle is still valid. Using this relation, we can define an acceleration for a particle in band n with quasimomentum k

$$a = \frac{\partial \langle v_n(k) \rangle}{\partial t} = \frac{1}{\hbar} \frac{\partial^2 E_n(k)}{\partial k^2} \frac{\partial k}{\partial t}, \quad (3.84)$$

and knowing the force exerted by the external field we can calculate the effective mass M^* of a Bloch particle.

$$M^* = \hbar^2 \left[\frac{\partial^2 E_n(k)}{\partial k^2} \right]^{-1}. \quad (3.85)$$

Thus the effective mass M^* depends implicitly on M through $E_n(k)$.

3.6 Wannier Functions

In his analysis of the effect of homogeneous fields, Wannier introduced a complementary set of basis functions to the Bloch basis [50]. These functions, unlike Bloch states, are normalizable over all space and are often used when describing localized particles.

Because the Bloch functions and energies are periodic in k with period $2\pi/a$, they can be written as a sum over lattice sites (a Fourier series) as

$$E_n(k) = \sum_l w_n(la) e^{ikla} \quad (3.86)$$

and

$$\psi_{n,k}(x) = \psi_n(x; k) = \sum_l \phi_n(x; la) e^{ikla}. \quad (3.87)$$

Using the result from Section 3.5.1 that ψ is an eigenvector of the lattice translation operator,

$$\psi(x + a) = T_a \psi(x) = e^{ika} \psi(x), \quad (3.88)$$

it is easy to show that the functions ϕ_n only depend on the difference of the two arguments. We rewrite Eq. (3.87) as

$$\psi_n(x; k) = \sum_l \phi_n(x - la) e^{ikla}. \quad (3.89)$$

These functions $\phi_n(x - la)$ are the *Wannier functions* and they are the dual functions of the Bloch states, each one containing all the information about the n^{th} band, in the sense that

$$\phi_n(x - la) = \int \psi_n(x; k) e^{-ikla} dk. \quad (3.90)$$

Additionally, it can be shown that if the Bloch function is normalized to unity over a lattice site, then the Wannier functions are normalized to unity over all space.

3.7 Solving the Schrödinger equation for a time independent cosine potential

In Section 3.5.1 we saw that the solutions of the Schrödinger equation for a periodic potential are of the form

$$\psi(x) = e^{ikx}u(x), \quad (3.91)$$

where $k \in [-\pi/a, \pi/a)$ and $u(x) = u(x+a)$. The dependence of the function u on the band index n is temporarily neglected, but it will reappear naturally as a consequence of solving the resultant eigenvalue equation. Since u is periodic, we can write it as a Fourier series,

$$\psi(x) = e^{ikx} \sum_m c_m e^{i(2\pi m/a)x}. \quad (3.92)$$

The energy of the state ψ will in general depend on the value of k as well as the function $u(x)$. Substituting (3.92) into the Schrödinger equation and using our scaled Hamiltonian (3.14) (period $a = 2\pi$) we get

$$\left[\frac{p^2}{2} + V_0 \cos x \right] \sum_m c_m e^{i(m+k)x} = E \sum_m c_m e^{i(m+k)x}, \quad (3.93)$$

In order to project out one of the Fourier components of $u(x)$ we premultiply by $\frac{1}{2\pi} e^{-i(m'+k)x}$ and integrate over x . Using the property

$$\frac{1}{2\pi} \int_0^{2\pi} e^{-im'x} e^{imx} dx = \delta_{m',m}, \quad (3.94)$$

where m and m' are both integers, we get

$$\begin{aligned} \frac{1}{2\pi} \int_0^{2\pi} \sum_m c_m e^{-i(m'+k)x} \left[\frac{1}{2} \left(-i \frac{\partial}{\partial x} \right)^2 + \frac{V_0}{2} (e^{ix} + e^{-ix}) \right] e^{i(m+k)x} \\ = E c_{m'} e^{i(m'+k)x}. \end{aligned} \quad (3.95)$$

After some algebra and suppressing the primes, we have

$$\frac{(m+k)^2}{2} c_m + \frac{V_0}{2} (c_{m+1} + c_{m-1}) = E c_m. \quad (3.96)$$

To solve this set of equations, we fix k and solve for the eigenvalues and eigenvectors of

$$\mathbf{A}\mathbf{c} = E\mathbf{c}, \quad (3.97)$$

where

$$A_{m,m} = \frac{(m+k)^2}{2} \quad (3.98)$$

$$A_{m,m+1} = A_{m+1,m} = \frac{V_0}{2}. \quad (3.99)$$

Since \mathbf{A} is both real and symmetric, the eigenvalues and eigenvectors (the functions $u_{n,k}(x)$) will also be real and symmetric. For each value of the quasimomentum $k \in [-1/2, 1/2)$ there will be many possible eigenvalues E , all the roots of the characteristic equation

$$\det |\mathbf{A} - E\mathbf{I}| = 0. \quad (3.100)$$

These roots are labeled (in order) by n , which corresponds to n^{th} band.

3.7.1 A weak periodic potential: Bragg scattering and avoided level crossings

In this section, we will investigate the behavior of the solutions to Eq. (3.97) in the shallow-well-depth limit. In doing so, the origin of the band gaps will become clear, and the concept of avoided level crossings will be reviewed. This very important concept from degenerate perturbation theory will also be crucial in the analyses of Bloch-band suppression in Chapter 4 and tunneling in Chapter 6.

Although this method fails when there are degenerate states, we will nonetheless begin by following the recipe of Rayleigh-Schrödinger perturbation theory to find the approximate solutions in the limit of small V_0 . We write our Hamiltonian as a sum of the unperturbed, free particle term and the periodic potential times the small parameter g ,

$$H = H^{(0)} + gV, \quad (3.101)$$

where in this case $V = \cos(x)$. The eigenenergies can then be written as a power series in g ,

$$E_n = E_n^{(0)} + gE_n^{(1)} + g^2E_n^{(2)} + \dots, \quad (3.102)$$

where $E_n^{(0)}$ is the free particle energy for the unperturbed plane wave state in the n^{th} band

$$H^{(0)}\psi_n^{(0)} = E_n^{(0)}\psi_n^{(0)} = \frac{(n+k)^2}{2}e^{i(n+k)x}. \quad (3.103)$$

The k index on the energies and eigenvectors is suppressed since we are solving the Schrödinger equation for a single, fixed value of k . The first- and second-order corrections to the energy are given by

$$E_n^{(1)} = V_{n,n} \quad (3.104)$$

and

$$E_n^{(2)} = \sum_{m \neq n} \frac{|V_{n,m}|^2}{E_n^{(0)} - E_m^{(0)}} \quad (3.105)$$

where the matrix elements are

$$V_{n,m} = \langle \psi_n^{(0)} | \cos(x) | \psi_m^{(0)} \rangle = \frac{1}{2}(\delta_{n,m+1} + \delta_{n,m-1}). \quad (3.106)$$

In general, the n^{th} Fourier component of the potential couples states n bands removed. In the case of a pure cosine potential, we see that the first order correction to the energy is zero, since there is no DC term, and that there is coupling only between neighboring bands. This feature and its relevance to Bragg scattering will be discussed shortly. So far the results have been reasonable; however, there is a problem with this approach when

$$k = -\frac{1}{2}(m+n) \pmod{1} \quad (3.107)$$

since then $E_n^{(0)} = E_m^{(0)}$ and the denominator in Eq. (3.105) vanishes. If, in addition, $V_{n,m} \neq 0$, this approach fails, and we must resort to degenerate perturbation theory at these points in k .

The result of coupling two degenerate states ψ_n and ψ_m is that two new eigenstates ψ_+ and ψ_- are created with energies

$$E_{\pm} = E^{(0)} + gE_{\pm}^{(1)} + \dots \quad (3.108)$$

where

$$E_{\pm}^{(1)} = \frac{1}{2} \left[V_{n,n} + V_{m,m} \pm \sqrt{(V_{n,n} - V_{m,m})^2 + 4|V_{n,m}|^2} \right]. \quad (3.109)$$

The first order correction to the energy includes the DC coupling as before as well as the coupling between the two states, and it reduces to Eq. (3.104) when $V_{n,m} = 0$. So we see that to first order in the well depth the degeneracy is lifted by the coupling term. For the case at hand the pure cosine potential only couples states that differ by one, so that only the degeneracies at $k = \pm\frac{1}{2}$ are lifted. Using Eq. (3.106) we have that

$$E_{\pm}^{(1)} = \pm\frac{1}{2}. \quad (3.110)$$

In summary, to first order in the well depth $g = V_0$, the bands are completely unchanged from the free particle result except at the band edges $k = \pm\frac{1}{2}$ where a *single* gap of width V_0 forms between the first ($n = 0$) and second ($n = 1$) bands. From Eq. (3.109) it is clear that higher order gaps would form with a term linear in V_0 if the corresponding Fourier component of the potential were present. However, with a pure cosine potential, each successively higher gap forms at the next higher power of V_0 so that, for example, the gap between the second and third bands is proportional to V_0^2 . This situation is depicted in Fig. 3.4, where the band structure is plotted for a well depth of $V_0 = 0.2$. Comparing this with Fig. 3.5, it is clear that the band gaps form at the points of degeneracy.

This phenomenon, known as an “avoided level crossing,” occurs whenever two coupled states are degenerate at some parameter value. If the parameter is time dependent, then there are two limiting regimes for the dynamics. There is the slow or “adiabatic” regime in which the level crossing

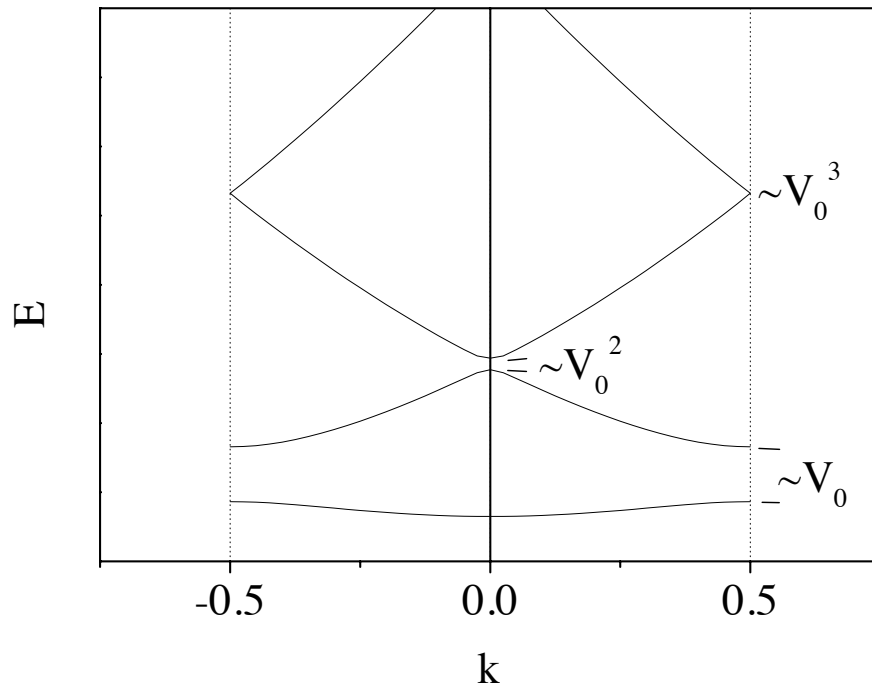


Figure 3.4: Band structure for a well depth of $V_0 = 0.2$. The potential breaks the degeneracy at the band edges and creates a band gap proportional to V_0^m , where the exponent is given by the gap number or, equivalently, the Bragg order.

remains avoided, and there is the fast passage regime in which the coupling is negligible during the time that the levels are degenerate, and the crossing is not avoided. In Chapter 6 the phenomenon of interband tunneling is understood as a non-adiabatic transition through the band gap as a result of a time-dependent quasimomentum.

Bragg scattering

The coupling that creates the band gaps produces a time-dependent effect, known as Bragg scattering, in which the particle's momentum along the standing wave is inverted but its kinetic energy is conserved. Essentially, the state of the particle oscillates between the two coupled momentum states. The condition for m^{th} order Bragg scattering is that the atomic de Broglie wavelength projected along x be m -fold commensurate with twice the lattice periodicity

$$m\lambda_{dB} = 2a = 4\pi. \quad (3.111)$$

This condition is clearly satisfied at the band edges $k_0 = (-1/2, 0, 1/2)$, where

$$\lambda_{dB} = h/p = 2\pi/(n + k_0), \quad (3.112)$$

and the Bragg order is

$$m = 2(k_0 + n). \quad (3.113)$$

In Fig. 3.5, the dispersion curves are plotted in the repeated zone scheme and the Bragg conditions are circled.

The strength of the Bragg coupling is simply equal to the band gap and determines the rate of the *Pendellösung* oscillations between the coupled states. In this way, we see that a pure cosine potential is not limited to just first-order Bragg scatterings since higher band gaps also form; however, as was mentioned before, the strength of the m^{th} order process scales as V_0^m . This is because an m^{th} order scattering requires m exchanges of two field photons. If,

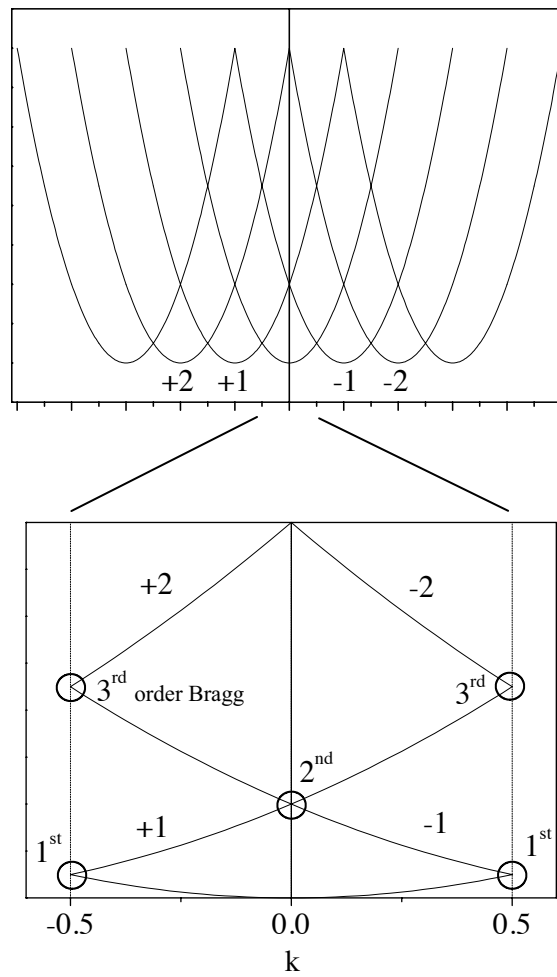


Figure 3.5: Dispersion branches plotted in the repeated zone scheme for a vanishingly small V_0 . The branches are labeled by the band index $n = 0, 1, 2, \dots$, and the points of degeneracy are circled and labeled by the corresponding Bragg order.

on the other hand, the potential had higher order Fourier components, then higher order Bragg scatterings could be satisfied with just one exchange, and these processes would then scale linearly with V_0 as well.

The phenomenon of atomic beam scattering by a standing wave of light has been studied extensively and is useful in the construction of atom interferometers [51, 52]. Moreover, repeated scatterings from a pulsed standing wave produces dynamics equivalent to the kicked pendulum, a paradigm system for Hamiltonian chaos. To this end, the use of this system in study of the quantum signatures of chaos has created a new experimental testing ground with a fertile past [53, 54, 45, 1, 42, 55, 40, 41] and a very bright future [56].

Another symmetry for optical lattices

In a paper by Wilkens *et al.* the authors pointed out that the “more obvious” translational invariance $x \rightarrow x + a$ for an optical lattice should be amended due to the observation that a translation by half the lattice periodicity $\frac{a}{2}$ plus an inversion in the atomic polarization $\sigma_1 \rightarrow -\sigma_1$ leaves the Hamiltonian

$$H = \frac{p^2}{2M} - \hbar\delta|e\rangle\langle e| + 2\hbar g\sigma_1 \cos(2\pi x/a) \quad (3.114)$$

invariant [57]. The authors develop the analysis with this symmetry operator and find that the dispersion curves of allowed energies develop avoided crossings both due to Bragg resonances and “Doppleron” resonances. The latter are velocity-tuned transitions associated with inversions of σ_1 . Although the results are quite reasonable, the authors neglected the issue of spontaneous emission which would greatly complicate the observation of these coherent, resonant effects. The detuning proposed was $\delta = -6\omega_r$ which is for sodium $2\pi \cdot 150$ KHz well within the natural linewidth $\Gamma/2\pi = 9.8$ MHz of the $3P_{3/2}$ state.

3.8 An experimental study of the Bloch band spectrum

In order to probe the structure of the Bloch bands, we introduced a weak, time-dependent modulation of the standing wave position to drive interband transitions. The modulation of position was accomplished by introducing a phase modulation on one of the constituent beams as described in Chapter 2. By first preparing the atoms in the lowest band and then measuring the fraction that remained after some interaction time, we observed Rabi oscillations of the population between the first and second band as a function of the modulation amplitude and frequency [5, 58]. A relatively weak modulation was chosen so that it would only couple but not modify the spectral features. In Chapter 4 we study the effect of a strong AC drive on the band structure and find that under certain conditions the bands undergo a dynamical suppression, effectively turning off Bloch tunneling [6].

Since the modulation strictly preserves the symmetry of the lattice, it couples states in different bands that have the same value of k . From the rate of the Rabi oscillations for a given modulation amplitude, the matrix elements coupling the states can be determined, and from the depth of the oscillations, an estimate of the density of states as a function of frequency can be made. Using this information, a fairly complete “map” of the bands can be constructed. A complimentary study of an optical lattice band structure was performed by Christophe Salomon’s group in Paris at ENS [37]. In this experiment, an acceleration was imposed, resulting in a time dependent quasi-momentum and consequently Bloch oscillations. By measuring the evolution of the velocity of a distribution localized in k , they were able to reconstruct the fundamental band energy using the relation Eq. (3.51).

The form of our potential with the added time-dependent modulation was

$$V(x, t) = V_0 \cos [2k_L x - \delta \cos(2\pi\nu t)], \quad (3.115)$$

where ν is the modulation frequency and δ is the dimensionless modulation amplitude. Since the amplitude is small, we expand the potential in powers of δ , and keeping terms to first order we have

$$V(x, t) = V_0 \cos(2k_L x) + V_0 \delta \sin(2k_L x) \cos(2\pi\nu t). \quad (3.116)$$

The stationary cosine term is recovered, and the modulation, to first order, produces a single frequency driving term that manifestly preserves the lattice periodicity and therefore couples states with the same value of k . Fig. 3.6 shows the energy bands in the reduced zone scheme within the first Brillouin zone for a well depth of $V_0 = 0.35E_u = h \cdot 70$ kHz. As indicated in Fig. 3.6, the drive frequency ν can be chosen to be resonant with the transition between the first two bands ($1 \leftrightarrow 2$), but far from resonance for transitions between successive bands [arrows (a) and (b)] at the same value of k . In this case, only two eigenstates of the atoms need to be considered. For such a driven two-level system the analytic solution is known and the population evolution exhibits Rabi oscillations. Given that the initial state of the system is in the lower band at some value of k , the expectation value of the state at the same value of k in the second band evolves according to

$$|a_2(t)|^2 = \frac{\Omega^2}{\Omega_{\text{eff}}^2} \sin^2(\Omega_{\text{eff}} t), \quad (3.117)$$

where Ω is the on-resonant Rabi frequency and Ω_{eff} is called the effective or off-resonant Rabi frequency. The resonant Rabi frequency is proportional to the matrix element of the driving term between the two coupled Bloch states,

$$\Omega = 1/\hbar |\langle \Psi_{0,k} | V_0 \delta \sin(2k_L x) | \Psi_{1,k} \rangle|, \quad (3.118)$$

and the effective Rabi frequency is given by

$$\Omega_{\text{eff}} = \sqrt{\frac{\Delta^2}{4} + \Omega^2}, \quad (3.119)$$

where the difference between the drive frequency $\omega = 2\pi\nu$ and the transition frequency ω_0 appears as $\Delta = \omega - \omega_0$. In Fig 3.7 the effective Rabi frequency Ω_{eff} as well as the amplitude of the oscillations $\Omega^2/\Omega_{\text{eff}}^2$ is plotted as a function of the probe frequency ω and k for the transition between the band pairs: $1 \leftrightarrow 2$, $2 \leftrightarrow 3$ and $1 \leftrightarrow 3$. It is interesting to note that the amplitude of the $1 \leftrightarrow 3$ transition falls to zero at the band edges $k = 0$ and $k = \pm\frac{1}{2}$ (not shown). At these values, the wave function possesses the same parity in the two bands and the overlap integral vanishes. In the deep well limit, one would expect this selection rule to suppress all transitions to the third band from the first since it would approach the selection rule for a harmonic oscillator, $\Delta n = \pm 1$. In order to compare this calculation with the experimentally measured population evolution, one must average the evolution over the entire band. Each state k will evolve with its own Rabi frequency and amplitude. If the drive frequency is close to resonance for both $1 \leftrightarrow 2$ and $2 \leftrightarrow 3$ [arrow (c) in Fig. 3.6] more than two levels participate in the interaction and more complicated dynamics are to be expected.

3.8.1 Observation of Rabi oscillations between Bloch bands

Fig. 3.8 compares the evolution of the first band survival probability for increasing modulation amplitude. The data was recorded for $V_0/h = 71$ kHz and $\nu = 70$ kHz, corresponding to a drive resonant with states near the band edge as indicated by arrow (a) in Fig. 3.6. All graphs clearly show damped Rabi oscillations of the population in the first band. The damping can be explained by taking off-resonant transitions into account. Atoms with a quasimomentum close to the value for which the resonance occurs can undergo Rabi oscillations with different frequencies and different amplitudes. Summing over the distribution of quasimomenta leads to a dephasing of the oscillations and therefore to a decrease of the oscillation amplitude. It is important to note that this

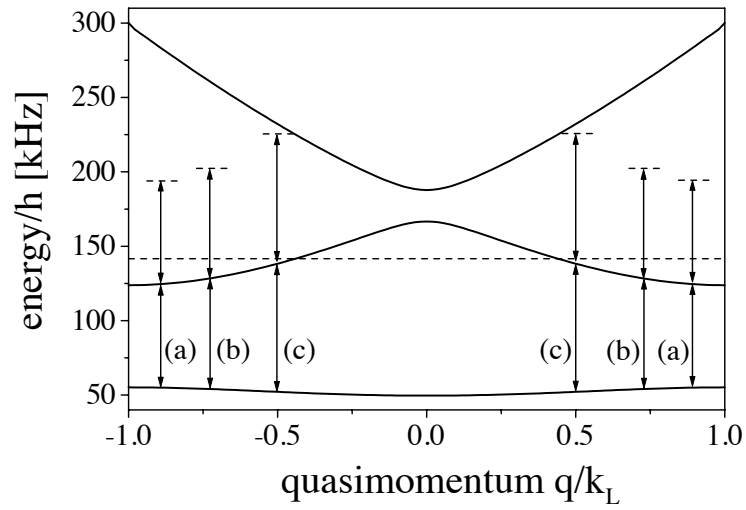


Figure 3.6: Band structure for an atom in a far-detuned standing wave. The energies are calculated relative to the bottom of the potential for a well depth of $V_0/h = 70$ kHz. In the reduced zone scheme the quasimomentum q is limited to the first Brillouin zone $[-k_L, +k_L]$. The arrows correspond to a modulation frequency of (a) 70 kHz, (b) 75 kHz, and (c) 85 kHz. The dashed line indicates the top edge of the potential ($2V_0$).

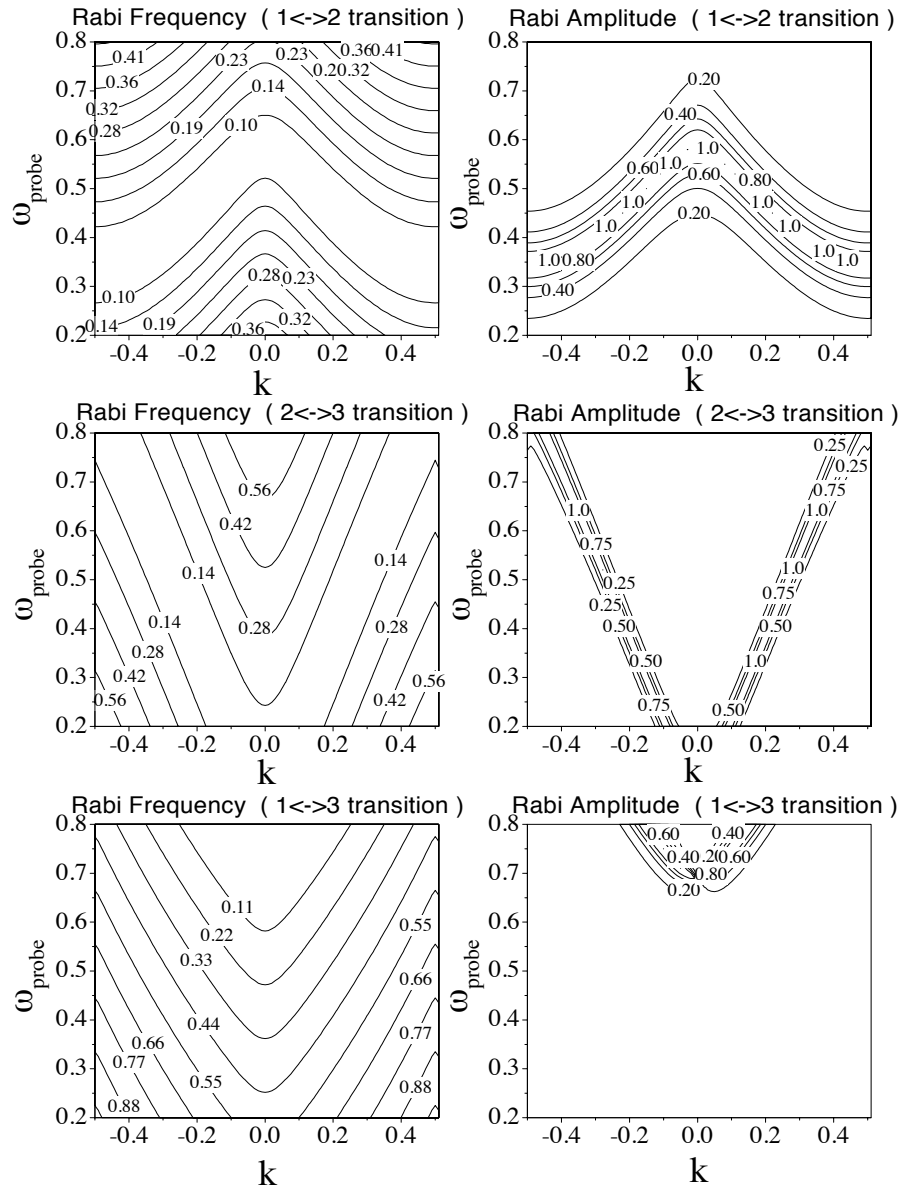


Figure 3.7: Contours of equal Rabi frequency and amplitude as a function of quasimomentum (abscissa) and probe frequency (ordinate) for transitions between the three band pairs: $1 \leftrightarrow 2$, $2 \leftrightarrow 3$ and $1 \leftrightarrow 3$. The calculations are performed at a well depth of $V_0 = 0.355$ and a modulation index of $\delta = 0.3$. The Rabi frequency associated with each contour is indicated in scaled units. In order to convert this or any other scaled, angular frequency to hertz simply multiply by 200 kHz (see Section 3.1).

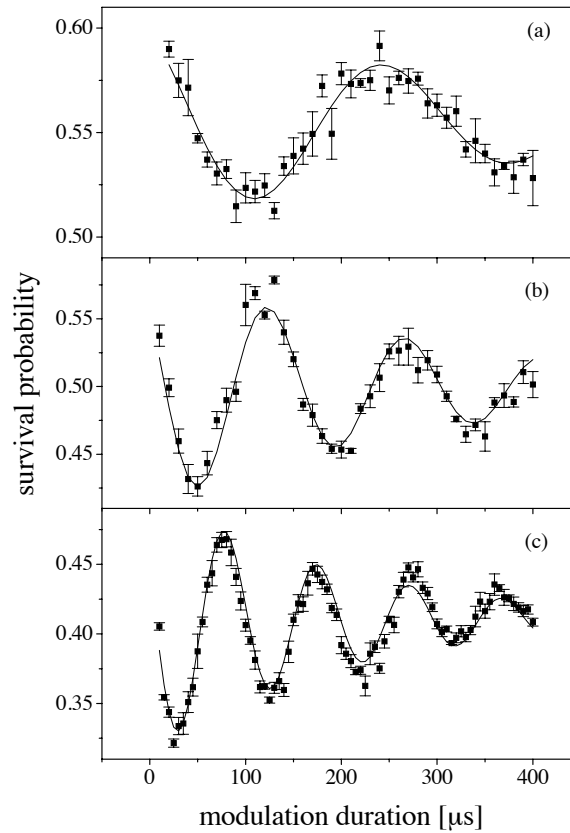


Figure 3.8: Measured survival probability in the lowest band as a function of modulation duration. The modulation amplitude was set to be (a) $\delta = 0.1$, (b) $\delta = 0.2$, and (c) $\delta = 0.3$. The data were taken at a well depth of $V_0/h = 71$ kHz and a modulation frequency of $\nu = 70$ kHz, corresponding to a drive near the band edge [as indicated in Fig. 3.6, arrow (a)]. Each run was repeated several times, and the error bar denotes the one-sigma error of the mean. The solid line displays the fit of an exponentially damped cosine function to the data.

damping effect is not caused by level decay, since the Bloch states involved are stable. The plots of the survival probability in the first band in Fig. 3.8 show an overall offset from unity at zero modulation duration. We attribute this offset to residual phase modulation of our standing wave, caused by electronic leakage of the modulation signal to the Marconi synthesizer, which drives transitions to higher bands. This residual modulation introduces a constant loss independent of the chosen modulation duration and does not affect the curve shape. Because the strength of the residual modulation depends on the set modulation amplitude δ , the curve offset changes with increasing δ .

As is evident from Fig. 3.8, the frequency of the Rabi oscillation increased with modulation amplitude. By fitting an exponentially damped cosine function to the experimental data, the value for the oscillation frequency can be extracted. The solid squares in Fig. 3.9 show the result of the least-square fits. The error bars denote the uncertainty in the frequency fitting parameter. The plot in Fig. 3.9 shows a Rabi frequency that varies linearly with the modulation amplitude δ . As was discussed above, one expects this linear relationship for the case of exact resonance. To compare to the experimental data we calculated the Rabi oscillation frequency for a modulation that drives transitions only at the band edge (i.e. we calculated Ω at $k = \frac{1}{2}$). Although 70 kHz is not precisely at the band edge, our assumption is that the matrix element at the edge is dominant. The resulting frequencies are displayed as hollow dots in Fig. 3.9. The calculation results are in good overall agreement with the experimental data. The slight deviation in frequency of the measured versus calculated data can be attributed to the experimental uncertainty in the determination of the well depth V_0 . As described in Chapter 2, we can measure the intensity of the interaction beams to within $\pm 10\%$, leading to the same relative error in the value for the well depth. To check the validity of restricting the range of quasimomenta to the band edge, we

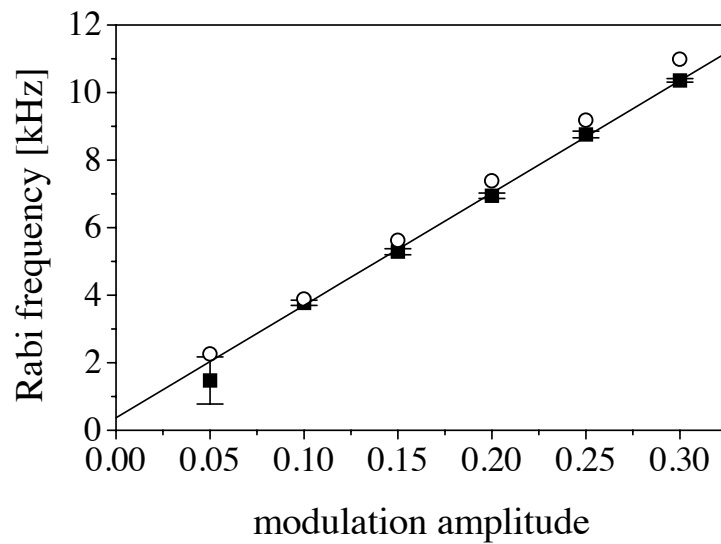


Figure 3.9: The solid squares show the measured Rabi frequency versus modulation amplitude for a well depth of $V_0/h = 71$ kHz and a drive frequency of $\nu = 70$ kHz. Uncertainties in the least square fit of the frequency are indicated as error bars. The line depicts the result of a linear least square fit through the experimental data. The hollow dots are the calculated Rabi frequencies for a drive at the band edge corresponding to the experimental parameters.

performed a numerical integration of Schrödinger's equation including the full potential in Eq. (3.115) with an initial condition that was taken to be a uniform distribution of atoms in the first band. The frequencies of the resulting population oscillations are not plotted in Fig. 3.9 because on the scale used they are indistinguishable from the calculated values. The calculation and the numerical integrations were performed using experimental values for the well depth and drive frequency with no adjustable parameters.

Driving transitions at the band edge has several advantages, one of which is the high density of states in that region. This situation results in a large number of atoms that can participate in the population transfer, therefore yielding a large detection signal. Another advantage is the slow damping rate of the Rabi oscillations. Since there is a large fraction of atoms contributing to the oscillation with the same frequency, the small number of off-resonantly driven atoms will not significantly decrease the amplitude of the averaged oscillation. Away from the band edge, however, the relative weight of the resonant oscillation frequency becomes less dominant and the off-resonant drives lead to an increased damping rate. The evolution of the first band population for three different drive frequencies is depicted in Fig. 3.10. The data were recorded at a well depth of $V_0/h = 71$ kHz and a modulation amplitude of $\delta = 0.3$. The insets show the result of the numerical integrations, for which the well depth was adjusted to $V_0/h = 72$ kHz in order to produce matching damping rates. The modulation frequencies in Fig. 3.10(a) through (c) match the corresponding arrows in Fig. 3.6 [(a) 70 kHz, (b) 75 kHz and (c) 85 kHz]. Larger damping rates for increasing modulation frequencies are clearly visible. In addition, we observed a decrease in oscillation amplitudes due to a smaller density of states at the center of the band. At the opposite side of the energy band, lower damping rates are recovered. Modulating the potential with frequencies beyond the band edges lead to Rabi oscillations with higher

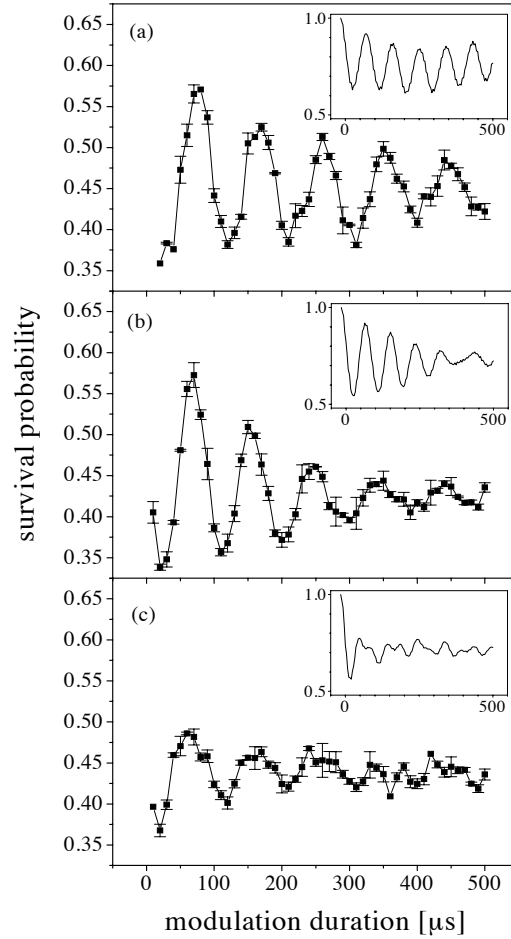


Figure 3.10: Measured survival probability in the lowest band as a function of modulation duration for three different frequencies. All data were recorded at a well depth of $V_0/h = 71$ kHz and a modulation amplitude of $\delta = 0.3$. The points are connected by solid lines for clarity. The insets show the result of numerical simulations at $V_0/h = 72$ kHz and $\delta = 0.3$. Note that the modulation duration does not include the $16 \mu\text{s}$ turn-on and turn-off time. The modulation frequency was set to be (a) $\nu = 70$ kHz, (b) $\nu = 75$ kHz, and (c) $\nu = 85$ kHz, corresponding to drives indicated by the arrows in Fig. 3.6

frequency and lower amplitude, as expected for off-resonantly driven systems (not shown).

Chapter 4

Dynamical Bloch band suppression

4.1 Introduction

In Chapter 3 we considered the behavior of particles in the presence of a time-independent cosine potential and saw that the energy distributions are characterized by bands of allowed energies separated by band gaps. The corresponding eigenstates are delocalized Bloch states that are freely propagating and hence result in Bloch tunneling. In this chapter, we examine the resultant behavior when a single frequency AC field is added to the periodic potential. The original analysis of this problem in the context of electronic motion in crystals was carried out by Dunlap and Kenkre, who showed that the system could be driven into an insulating state by the application of an AC electric field [59]. Specifically, they showed that in the tight-binding approximation, the mean squared displacement of the wave function becomes *bounded* for a particular choice of the AC field strength and frequency. Associated with this phenomenon of “dynamical localization” (not to be confused with dynamical localization in quantum chaos) is a collapse of the Bloch band widths [60, 61]. A great deal of complimentary experimental work was done with superlattices [62]. However, this phenomenon is obscured in these systems by multi-photon assisted tunneling and can only be inferred from a suppression of the conductance at low field strengths [63, 64]. In this experiment, we observed the evolution of the quasienergy band spectrum from the wide unperturbed case

to a flattened but splintered band at the condition for band collapse [6].

4.2 Single band calculation

The origin of band suppression is most easily seen in a calculation using the single band approximation, where one can derive an analytic result for the dispersion. We provide here the results of this calculation done by Zhao [61]. He begins with the Hamiltonian

$$H(x, t) = H_0(x) - Fx \cos(\omega t), \quad (4.1)$$

where H_0 is the field-free, spatially periodic part. Since the full Hamiltonian is periodic in time with period $T = 2\pi/\omega$, one knows from Floquet's theorem (see Section 3.5.1) that the solutions will be of the form

$$\psi(x, t) = e^{-i\epsilon t} u_\epsilon(x, t), \quad (4.2)$$

where

$$u_\epsilon(x, t) = u_\epsilon(x, t + T). \quad (4.3)$$

Since the Hamiltonian is time-dependent, the energy is no longer conserved; however, because the time dependence is periodic, there is a conserved quantity ϵ that is associated with the energy, and it is typically referred to as the quasienergy, in analogy with the quasimomentum for spatially periodic solutions. The functions $u_\epsilon(x, t)$ satisfy the Schrödinger equation

$$\left[H(x, t) - i\hbar \frac{\partial}{\partial t} \right] u_\epsilon(x, t) = \epsilon u_\epsilon(x, t). \quad (4.4)$$

By writing this wave function as a linear superposition of *single-band* Wannier functions (see Section 3.6)

$$u_\epsilon(x, t) = \sum_l u_{\epsilon l} \phi(x - la), \quad (4.5)$$

where the sum is over lattice sites, Zhao finds that the amplitudes satisfy

$$i\hbar \frac{d}{dt} u_{\epsilon l} = \sum_j R_j u_{\epsilon(j+l)} - [\epsilon + laF \cos(\omega t)] u_{\epsilon l} \quad (4.6)$$

where R_j is the hopping term given by the matrix element

$$R_j = \langle 0 | H_0 | j \rangle = \int_{-\infty}^{\infty} \phi^*(x) H_0 \phi(x - ja). \quad (4.7)$$

After employing a discrete Fourier transform to obtain the equations in reciprocal space, Zhao solves for the quasienergy

$$\epsilon(k) = R_0 + 2 \sum_{l=1}^{\infty} R_l J_0(laF/\hbar\omega) \cos(lk), \quad (4.8)$$

where J_0 is the ordinary Bessel function of order zero. In the limit that $F \rightarrow 0$ this reduces to the result for the undriven system,

$$\epsilon(k) = R_0 + 2 \sum_{l=1}^{\infty} R_l \cos(lk). \quad (4.9)$$

We note that in analogy with spatially periodic solutions, where the energies are periodic in k ($\epsilon(k) = \epsilon(k + 2\pi/a)$), the energies are repeated at integer multiples of the drive frequency $\omega = 2\pi/T$. There is an associated quasienergy Brillouin zone $(-\pi/T, \pi/T)$ as well. From Eq. (4.8) we see that the temporal modulation produces an effective hopping term

$$R_l^{\text{eff}} = R_l J_0(laF/\hbar\omega). \quad (4.10)$$

When only nearest-neighbor interactions are counted, one term in the sum is kept and Eq. (4.8) reduces to

$$\epsilon(k) = R_0 + 2R_1^{\text{eff}} J_0(aF/\hbar\omega) \cos(k). \quad (4.11)$$

Therefore, when the argument is a root of J_0 ,

$$J_0(aF/\hbar\omega) = 0, \quad (4.12)$$

the dispersion “collapses” to a constant value R_0 , the on-site energy. If the other terms are kept, the band width is suppressed as F is increased but does not collapse to zero since there is no value of $aF/\hbar\omega$ for which all of the terms in the sum of Eq. (4.8) are zero. In Fig. 4.1, Eq. (4.8) is plotted for several values of $aF/\hbar\omega$. The values of R_l were not calculated but rather were extracted from the Fourier decomposition of the bands as calculated in Section 3.3.

In Chapter 3, we saw that the spreading of an initially localized wave packet is due to Bloch tunneling, and the band width is indicative of the lifetime of this localized state. Associated with the suppression of the band widths is then a suppression of Bloch tunneling, and it was shown by Dunlap and Kenkre that in the tight-binding case the mean-squared displacement of the wave function is bounded at the band collapse condition.

4.3 Observation of Bloch band suppression

To experimentally realize the external AC field, a phase modulation was imposed on one of the standing wave component fields, producing a sinusoidal variation in the position of the optical lattice. In the lab frame, the potential has the form $V_0 \cos[2k_L x + \lambda_s \sin(\omega_s t)]$ where λ_s and ω_s are the modulation index and frequency. In the co-moving frame of the lattice, the Hamiltonian has the form

$$H_{\text{latt}} = \frac{p^2}{2M} + V_0 \cos(2k_L x) + x \frac{M\lambda_s\omega_s^2}{2k_L} \sin(\omega_s t), \quad (4.13)$$

where the mass of the atom M appears, revealing the inertial origin of this term. In this case the amplitude of the AC force is

$$F = M\lambda_s\omega_s^2/2k_L, \quad (4.14)$$

and the lattice periodicity is

$$a = \pi/k_L. \quad (4.15)$$

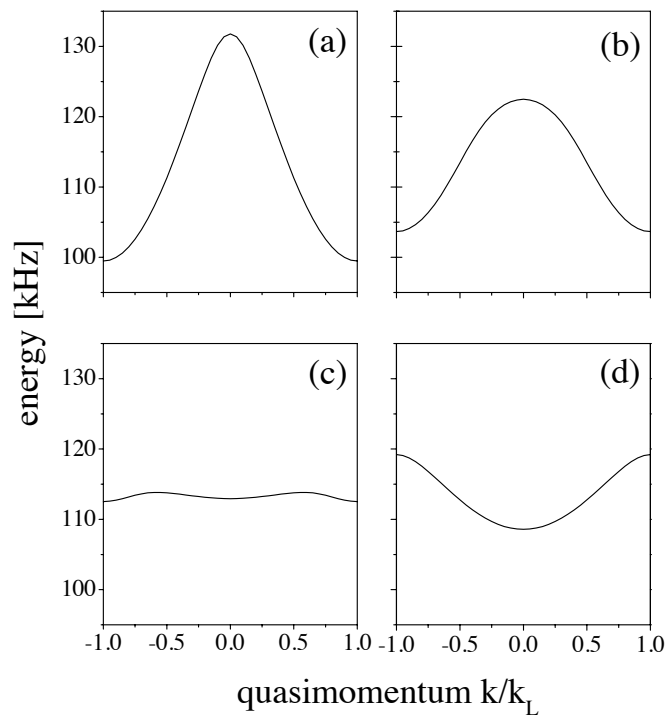


Figure 4.1: The single band quasienergies for the second band plotted as a function of k at four different values of $aF/\hbar\omega$. In (a)-(d) the values of this ratio were 0, 1.25, 2.38, and 3.14. Plot (a) is the unperturbed band. As this ratio is increased, the band width shrinks and in (d) reaches a minimum when equal to a root of J_0 .

Inserting this into Eq. (4.12) the condition for band suppression becomes

$$J_0\left(2\pi\lambda_s\frac{\omega_s}{8\omega_r}\right) = 0 \quad (4.16)$$

where ω_r is the recoil frequency given by Eq. (3.11).

As was done in Chapter 3 to observe the spectral characteristics of this system we introduced an additional weak modulation that could resonantly drive transitions between states of the potential without significantly modifying their energies. By preparing the atoms in the first band and measuring the depletion of its population as a function of the probe frequency, a spectrum was obtained. Both the strong and weak phase modulations were turned on smoothly during 16 μ s to avoid phase jumps that could drive transitions between bands. The total time that the atoms were exposed to the phase modulations was 500 μ s. For each spectrum, the strong drive amplitude was fixed, and the probe modulation frequency was scanned in the range (50–200) kHz. The modulation index of the weak probe was $\lambda_s = 0.05$. In order that the strong drive only modify the band structure without driving transitions, its frequency was chosen to be $\omega_s/2\pi = 20$ kHz, far less than the width of the first band gap.

Fig. 4.2 shows a series of measured spectra for various AC field strengths. When there is no strong field present ($\lambda_s = 0$) we obtain a spectrum of the unperturbed Bloch band structure (Fig. 4.2a). Although the spectrum maps the transition from the first to second band ($1 \leftrightarrow 2$), the spectrum width represents that of the second band since, for the chosen well depth, the first band is only 3 kHz wide. As the modulation strength is increased, the second band flattens and side peaks spaced at multiples of the strong field frequency grow in size. For a modulation index of $\lambda_s = 3.8$, the condition for band collapse is fulfilled. For this case, the central peak is at its narrowest, with a half width of approximately 15 kHz. As the modulation index is increased past the band

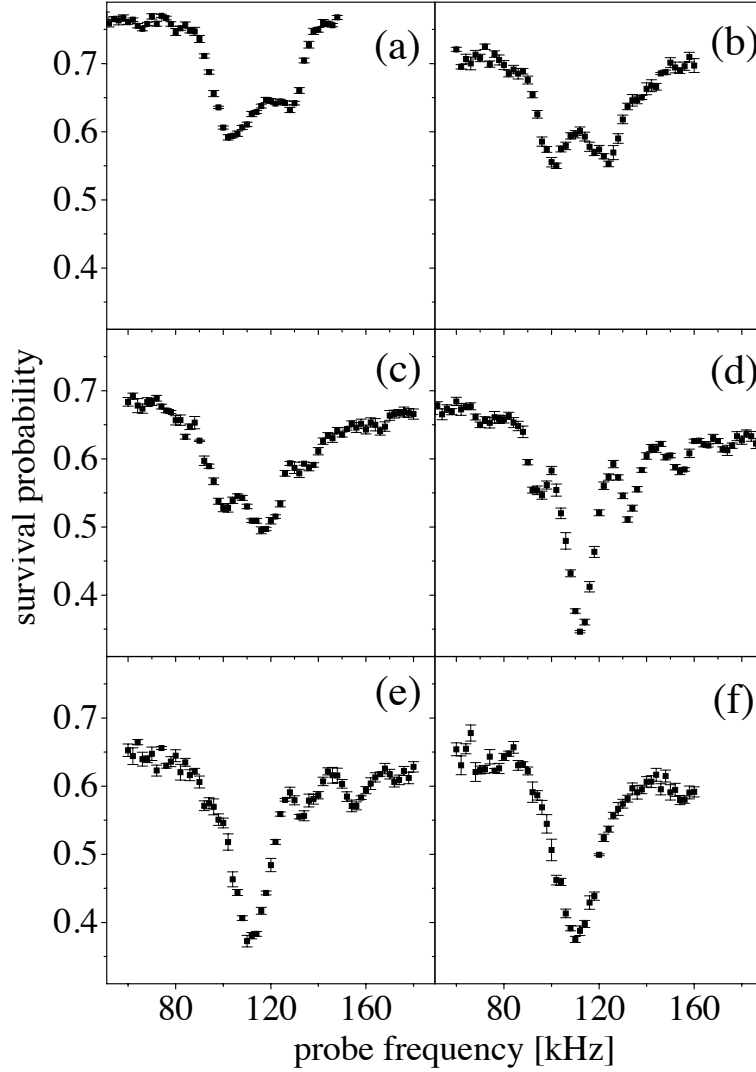


Figure 4.2: Measured survival probability in the lowest band as a function of probe frequency for six different strong field modulation strengths. In (a)-(f) the values for λ_s were 0, 1, 2, 3.8, 4.3, and 5. Spectrum (a) corresponding to the unperturbed Bloch band, and spectrum (d) corresponding to the system at the band collapse condition. The side peaks that develop are separated by the strong AC modulation frequency (20 kHz), and correspond to multi-photon transitions. Each point is an average of several runs, and the error bar denotes the one-sigma error of the mean.

collapse condition, the central peak broadens and the previously distinct side peaks overlap producing broad tails on the central resonance.

Mirror vibration and frequency instabilities of our electronic drivers caused a low frequency fluctuation of the standing wave position that excited atoms out of the lowest band at a constant rate. This loss, which was constant for each run, resulted in a background of lost atoms and prevented the survival probability from approaching unity even when the probe was far from resonance. An additional complication arose from the fact that although the strong AC modulation frequency was far from resonance for the ($1 \leftrightarrow 2$) transition, its amplitude was nevertheless large enough to drive off-resonant transitions. This explains the drop of the baseline for larger values of λ_s .

4.4 Multi-band analysis of band suppression

To gain further insight into the effect of higher bands on band suppression we have solved numerically the Schrödinger equation for the quasienergies and the corresponding wave functions, in collaboration with Professor Qian Niu and his student Roberto Diener. In addition, the coupling strengths between the first and higher bands for each quasienergy were calculated in order to generate a prediction for the experimental spectral distributions of Fig. 4.2. For convenience, we used the scaled units described in Section 3.1. A unitary transformation of the Hamiltonian (see Appendix A) in Eq. (4.13) yields

$$H = \frac{[p - \lambda_s \omega_s \cos(\omega_s t)]^2}{2} + V_0 \cos(x). \quad (4.17)$$

In this form the spatial periodicity is preserved, and we have $H(x + 2\pi, t) = H(x, t) = H(x, t + T)$, where $T = 2\pi/\omega_s$. As before, we use Floquet's theorem and write the wave function in the form

$$\Psi_{\epsilon, k}(x, t) = e^{i(kx - \epsilon t)} u_{\epsilon, k}(x, t), \quad (4.18)$$

where the function u is the periodic part

$$u_{\epsilon,k}(x, t + T) = u_{\epsilon,k}(x, t) = u_{\epsilon,k}(x + 2\pi, t). \quad (4.19)$$

Since the function $u_{\epsilon,k}$ is periodic, we can expand it as a Fourier series and write the wave function as

$$\Psi_{\epsilon,k}(x, t) = e^{i(kx - \epsilon t)} \sum_{n,m} c_{n,m} e^{i(nx - m\omega_s t)}. \quad (4.20)$$

Inserting this expression into Schrödinger's equation

$$H\Psi_{\epsilon,k} = i\dot{\Psi}_{\epsilon,k}, \quad (4.21)$$

we obtain a set of equations for the coefficients $c_{n,m}$ and the quasienergy ϵ

$$\begin{aligned} \left[\frac{(k+n)^2}{2} + \frac{\lambda_s^2 \omega_s^2}{4} - m\omega_s - \epsilon \right] c_{n,m} = \\ (k+n) \frac{\lambda_s \omega_s}{2} (c_{n,m+1} + c_{n,m-1}) - \frac{\lambda_s^2 \omega_s^2}{8} (c_{n,m+2} + c_{n,m-2}) \\ + \frac{V_0}{2} (c_{n+1,m} + c_{n-1,m}). \end{aligned} \quad (4.22)$$

The most general representation of the spectrum is the repeated-zone scheme, in which each quasienergy is represented by all of its possible values $\epsilon + j\omega_s$, for integer values of j . For this reason, even if we restrict our attention to one quasienergy brillouin zone $(-\omega_s/2, \omega_s/2]$, we are faced with a dense spectrum since every band has a copy inside this region. In order to interpret this spectrum and to connect this analysis to our experimental observations, we considered the case of transitions between these states induced by a second, weak AC field of frequency ω . The full Hamiltonian is

$$H'(t) = H(t) - p\lambda\omega \cos(\omega t), \quad (4.23)$$

where $H(t)$ is given by Eq. (4.17) and $\lambda \ll \lambda_s$. We assume that an atom is in the quasienergy state $\Psi_{\epsilon_1,k} = |1\rangle$ corresponding to the first band and that the

perturbation only drives transitions to one other quasienergy state $\Psi_{\epsilon_2, k} = |2\rangle$ (this approximation is valid as long as the frequency ω is close to resonance). Given the state vector of the atom, $\Psi = a_1|1\rangle + a_2|2\rangle$, the equations of motion for a_1 and a_2 are:

$$\begin{aligned} i\dot{a}_1 &= -\lambda\omega \cos(\omega t)[a_1\langle 1|p|1\rangle + a_2\langle 1|p|2\rangle] \\ i\dot{a}_2 &= -\lambda\omega \cos(\omega t)[a_1\langle 2|p|1\rangle + a_2\langle 2|p|2\rangle]. \end{aligned} \quad (4.24)$$

For short times the second state is not significantly populated, so that $|a_2| \ll |a_1| \approx 1$. To lowest order, $\dot{a}_2 = -i\lambda\omega \cos(\omega t)\langle 2|p|1\rangle$. Since the quasienergy states are not stationary the time dependence of the matrix element $\langle 2|p|1\rangle$ contains many frequencies,

$$\langle 2|p|1\rangle = \sum_j e^{i(\epsilon_2 - \epsilon_1 + j\omega_s)t} \Gamma_j(k), \quad (4.25)$$

where $\Gamma_j(k) = \sum_{n,m} (k+n)c_{n,m}^{(1)}(c_{n,m+j}^{(2)})^*$. Resonant transitions occur whenever $\omega \approx \pm(\epsilon_2 - \epsilon_1 + j_0\omega_s)$ for some value of j_0 . In analogy with the rotating wave approximation, where only the nearly resonant term is kept, we approximated the matrix element Eq. (4.25) by just one term of the sum,

$$\langle 2|p|1\rangle = e^{i(\epsilon_2 - \epsilon_1 + j_0\omega_s)t} \Gamma_{j_0}(k). \quad (4.26)$$

The quasienergies were calculated numerically for the cases in which $\lambda_s = 0, 3.8$, and 5.2 . The values $\omega_s = 0.10$ and $V_0 = 0.510$, corresponding to $\omega_s/2\pi = 20$ kHz and $V_0/h = 102$ kHz in real units, were chosen to match the parameters used in the experiment. We restricted the values of $\epsilon_1(k)$ to the interval $(-0.2, -0.1)$, corresponding to the location of the first band in the absence of the strong AC field. The results, which were plotted in the repeated-zone scheme, are shown in the left three panels of Fig. 4.3. The three values of λ_s chosen correspond to (a) no strong AC field, (b) at, and (c) past the condition for band collapse. The plot of $\epsilon_2(k) + j_0\omega_s$ was gray-scaled by the

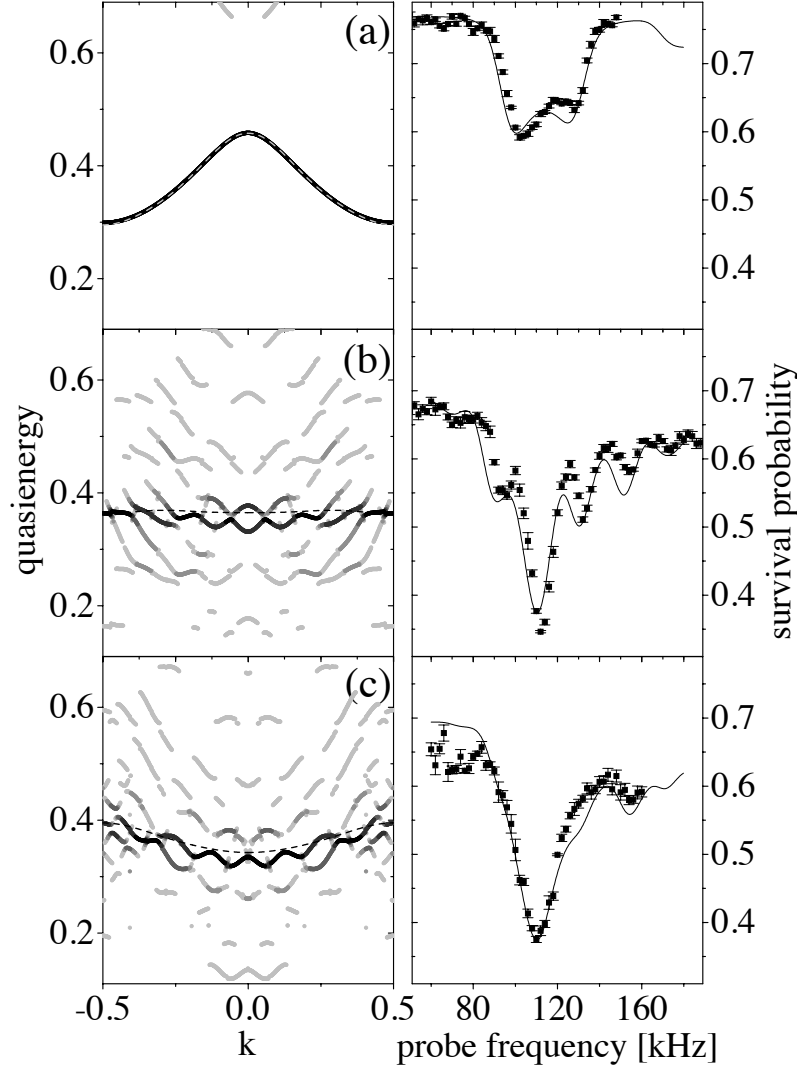


Figure 4.3: The left three panels are plots of the calculated quasienergies versus k for three values of λ_s (0, 3.8, and 5.2). We restricted our attention to the energy range $[0.1, 0.7]$ which corresponds to energies accessed by our probe. In addition, the quasienergies were plotted using a gray scale to differentiate their on-resonant coupling strengths $\Gamma_{j_0}(k)$. For comparison, the single-band approximation result is shown by the dashed line. To the right of each panel is the experimentally measured spectrum (points with error bars) and the theoretical spectrum (thin line) predicted from the calculated quasienergy bands.

value of $[\Gamma_{j_0}(k)]^2$, which determines the transition probability and therefore the quasienergies that are important.

For comparison, the second band was calculated using the single band approximation, and the result, Eq. (4.8), is plotted with dashed lines. Although it does not show the detailed structure present in the spectrum, the single-band approximation does describe the general behavior of the most prominent quasienergies.

When $\lambda_s = 0$ the quasienergy spectrum is simply the real energy spectrum repeated with periodicity ω_s . However, only one representation of each quasienergy is present in Fig. 4.3a, since all values of $\Gamma_{j_0}(k)$ with $j_0 \neq 0$ are zero. This is due to the absence of photons with frequency ω_s , which are necessary for such transitions. As λ_s is increased, these repetitions become accessible, and in addition they begin to interact and develop avoided level crossings. This effect modulates and splinters the flat and continuous dispersion curve predicted by the single-band model; it broadens the collapsed band, producing a suppression in the bandwidth.

Using the calculated quasienergies and their corresponding matrix elements, we generated spectral distributions to compare with the experimental data. Rabi oscillations are known to govern the transition probabilities between bands and have been characterized in this system [5]. In order to calculate the survival probability for the first band as a function of ω , we used the approximation Eq. (4.26) and neglected the diagonal terms in Eqs. (4.24) (the weak probe drives transitions between bands but does not change their shape or position). The results shown in the right panels of Fig. 4.3 were obtained by assuming that the first band was uniformly populated. In addition, the spectra were averaged to account for the finite Gaussian bandwidth of the weak probe used in the experiment. There were two additional experimental effects that had to be accounted for in order to compare the spectral distributions. The

first effect, mentioned previously, was a baseline shift due to a constant loss of atoms from the optical lattice. The second was a systematic underestimate of the survival probability due to non-uniform detection of our atomic sample. The spectra were scaled and the baselines shifted to compensate for these effects. The absolute position and shape of the resonances, which are the most important features, are independent of these effects. The agreement between the measured and calculated spectra is good, indicating that the approximation in Eq. (4.26) is valid and that Fig. 4.3 is a faithful representation not only of the quasienergies but also of their respective coupling strength with the lowest band.

Chapter 5

Bloch oscillations and the Wannier-Stark Ladder

In this chapter we consider the behavior of atoms in a weakly accelerating optical lattice. Since the velocity of the optical lattice is given by the frequency difference $\Delta\nu$ of the two constituent beams,

$$v = \frac{\lambda}{2}\Delta\nu, \quad (5.1)$$

a constant acceleration is achieved by linearly ramping this difference. The resulting Hamiltonian for a general time-dependent frequency difference is

$$H(x, p, t) = \frac{p^2}{2M} + V_0 \cos(2k_L[x - \alpha(t)]), \quad (5.2)$$

where α is proportional to the total accumulated phase

$$\alpha(t) = \frac{1}{2k_L} \int_0^t 2\pi\Delta\nu(t) dt. \quad (5.3)$$

This Hamiltonian is related by a unitary transformation (see Section A.2) to two other forms that will be used in this chapter,

$$H(x, p, t) = \frac{p^2}{2M} + V_0 \cos(2k_L x) + xaM \quad (5.4)$$

and

$$H(x, p, t) = \frac{(p - Mv)^2}{2M} + V_0 \cos(2k_L x), \quad (5.5)$$

where the acceleration $a = \ddot{\alpha}$ and velocity $v = \dot{\alpha}$ of the standing wave are controlled through this frequency difference. We will sometimes refer to the abbreviated form

$$H = H_0 - Fx \quad (5.6)$$

where H_0 is the unperturbed periodic part and $F = -Ma$ is the inertial force experienced by the atom. The inertial force has a negative sign since it is not the atom but rather the reference frame which is accelerating. We note here that this Hamiltonian is equivalent to the one that describes the motion of an electron in a periodic electric potential with an external homogeneous electric field.

For small enough accelerations, an atom initially in the first band will remain there and accelerate with the lattice. In the frame of the potential, the atom becomes bounded, no longer Bloch tunneling into adjacent sites, because the acceleration breaks the translational symmetry. In this accelerating frame, the atom oscillates in velocity and space at the Bloch frequency and, as a result, each band becomes subdivided into a ladder of discrete states known as the *Wannier-Stark ladder*, where the ladder spacing is proportional to the Bloch frequency. In reality, the energies of the Wannier-Stark states are not perfectly discrete, but have a Lorentzian shape due to their finite lifetime. Therefore, the atoms will not indefinitely accelerate with the lattice, but will decay out of the bound states and become free particles. This tunneling phenomenon is the subject of Chapter 6.

5.1 Bloch oscillations

As was discussed in Section 3.5.2, Bloch considered the response of an electron in a lattice to the application of an external, uniform electric field, and he showed that the effect of the external field is to produce a translation

in the quasimomentum k with constant velocity. This prediction was confirmed by the analysis of Jones and Zener, who proved the result for a general periodic potential, given that transitions to higher bands are negligible (see Section 3.5.2). Specifically, the result is that each Bloch state retains its time-independent form, but the quasimomentum evolves *as if* the particle were free and $\hbar k = p$:

$$\hbar \dot{k} = F. \quad (5.7)$$

However, $\hbar k \neq p$ and F is not the total force, but only the force due to the external field. A striking consequence of this result is that particles are predicted to *oscillate* in space rather than accelerate uniformly in response to the external field. Since E_k is periodic in k over the first Brillouin zone, the average velocity, which is given by

$$\langle v_n(k) \rangle = \frac{1}{\hbar} \frac{\partial E_k}{\partial k}, \quad (5.8)$$

is also periodic. Therefore, a constant translation of k produces a time-dependent oscillation of the velocity with period

$$\tau_B = h/|F|d, \quad (5.9)$$

where d is the lattice period previously defined as a (a is now reserved for the acceleration of the optical lattice). As a result, the position will also oscillate with a peak-to-peak excursion of

$$\delta x = \Delta/|F|, \quad (5.10)$$

where Δ is the band width. If we express this excursion in lattice periods d , we have

$$\delta x = \frac{\Delta}{h\nu_B} d. \quad (5.11)$$

The picture of Bloch oscillations in reciprocal space is illustrated in Fig. 5.1. In the case of Bloch oscillations, the acceleration is small enough

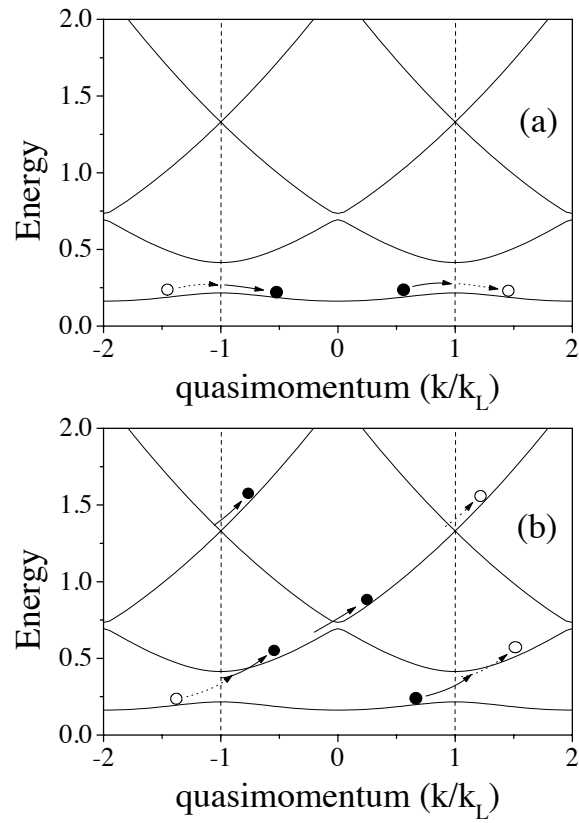


Figure 5.1: Illustration of a particle's motion through reciprocal space when a force is applied to the lattice. In case (a), the acceleration producing the motion in k is sufficiently weak that the particle reflects from the Bragg plane at k_L and emerges on the opposite side of the first Brillouin zone at $-k_L$. In case (b), the acceleration is so large that the particle crosses the first band gap non-adiabatically and emerges on the opposite side of the first Brillouin zone it in the second band. Since the successive band gaps are much smaller than the first, the particle crosses these gaps as well, and climbs up the dispersion curve, accelerating as a free particle would.

that the particle reflects when it reaches the Bragg plane at k_L . It will then emerge on the opposite side of the Brillouin zone in the same band as before. If the acceleration is too large compared to the potential coupling these two states, then the particle will traverse the gap as if it were a free particle and emerge in the second band. This tunneling process is the subject of Chapter 6.

5.1.1 The adiabatic approximation: a sufficiently weak acceleration

This result, that for a sufficiently weak field the Bloch states retain their time-independent form but have a time-dependent quasimomentum, can be deduced from the adiabatic theorem [65]. To this end, the adiabaticity criterion gives us an indication of what is a sufficiently weak field. This condition, that the force not induce interband transitions, is

$$\left| \left\langle \psi_{n,k} \left| \frac{\partial}{\partial t} \right| \psi_{n',k} \right\rangle \right| \ll |E_n(k) - E_{n'}(k)|/\hbar, \quad (5.12)$$

where $n \neq n'$. This condition reduces to

$$\left| \left\langle u_{n,k} \left| \frac{\partial}{\partial t} \right| u_{n',k} \right\rangle \right| \ll |E_n(k) - E_{n'}(k)|/\hbar, \quad (5.13)$$

where we are using the form of the unperturbed Bloch states,

$$\psi_{n,k} = e^{ikx} u_{n,k}(x). \quad (5.14)$$

Using the chain rule, we can replace the time derivative with a derivative with respect to k and we get

$$\left| \left\langle u_{n,k} \left| \frac{\partial}{\partial k} \right| u_{n',k} \right\rangle \right| F \ll |E_n(k) - E_{n'}(k)|. \quad (5.15)$$

By differentiating the Schrödinger equation with respect to k , it is easy to show that

$$\left\langle u_{n,k} \left| \frac{\partial}{\partial k} \right| u_{n',k} \right\rangle = \frac{1}{E_{n'}(k) - E_n(k)} \left[\left(\frac{\hbar^2 k}{M} - \frac{\partial E_n}{\partial k} \right) \delta_{n,n'} + \left\langle u_{n,k} \left| \frac{\hbar p}{M} \right| u_{n',k} \right\rangle \right]. \quad (5.16)$$

Using this result when $n' \neq n$ and the fact that $F = ma$ we finally have that

$$|a| \ll \frac{[E_n(k) - E_{n'}(k)]^2}{\hbar \langle u_{n,k} | p | u_{n',k} \rangle}. \quad (5.17)$$

In the shallow well limit, the right hand side will be smallest at the band edges, where $E_n(k_L) - E_{n'}(k_L) \approx V_0^m$ and m denotes the m^{th} band gap (see Section 3.7.1). We see that the condition for an adiabatic acceleration becomes very stringent for higher gaps that scale like V_0^{2m} . At the band edge, we can approximate the two wave functions as nearly degenerate plane waves, and the condition for the acceleration to be adiabatic for first band gap is

$$|a| \ll \frac{V_0^2}{\hbar^2 k_L}. \quad (5.18)$$

We can express this condition in terms of the Bloch frequency

$$\nu_B = \frac{1}{\tau_B} = |F|d/h, \quad (5.19)$$

where $d = \pi/k_L$ is the lattice periodicity. We have that

$$\nu_B \ll \frac{V_0^2}{4\hbar^2 \omega_r}, \quad (5.20)$$

where the recoil frequency ω_r is defined in Chapter 3. Using the scaling also defined in that chapter, we have that

$$\nu_B \ll (V'_0)^2 \cdot 400 \text{ kHz}, \quad (5.21)$$

where $V'_0 = V_0/E_u$ is the scaled well depth.

It is worth mentioning here that for our Wannier-Stark experimental data, our scaled well depths were typically 0.4, making accelerations below 950 m/s^2 adiabatic (assuming “ \ll ” is satisfied by a factor of 10). Despite this condition, we successfully measured Wannier-Stark resonances, the spectral signature of Bloch oscillations, at accelerations as high as 3000 m/s^2 .

5.2 The Wannier Stark ladder

Although Bloch oscillations had been predicted, the problem of particle motion in a periodic potential under the influence of an applied field was still an open question. In 1960, some 32 years after Bloch's seminal paper, Wannier pointed out that for a three dimensional crystal, if the field were directed along a lattice axis then the periodic motion in k produces an energy quantization, a Stark ladder of states [50].

The simplest way to argue this point is for the case of one-dimension. First, we assume that there exists a solution ψ with energy E :

$$H\psi = (H_0 - Fx)\psi = E\psi. \quad (5.22)$$

Now, we act on this with the lattice translation operator n times,

$$(T_d)^n(H\psi) = (T_d)^n(E\psi), \quad (5.23)$$

and using $[T_d, H_0] = 0$, we have that

$$H\psi(x + nd) = (E + ndF)\psi(x + nd). \quad (5.24)$$

So we see that if $\psi(x)$ is a solution then there is exists a whole ladder of states $\psi(x + nd)$ with energies shifted from E by an integer times the Bloch energy corresponding to the Bloch frequency, Eq. (5.19):

$$\Delta E = ndF = nh\nu_B. \quad (5.25)$$

Following the proposal by Wannier, there was a flurry of activity in support of these predictions, and simultaneously a debate began regarding the methods employed. A review of this debate is given by Krieger and Iafrate in a paper where they offer an alternate approach to the problem [66]. Here we provide a short list of the main objections.

Most of the criticisms came from Zak and Rabinovitch who rejected the proposals of Bloch oscillations and the Wannier-Stark ladder because they were based on unfounded assumptions (neglecting interband coupling terms) and methods (the use of extended, periodic basis functions). The first criticism addresses the argument presented above. Zak showed that the spectrum of E is *continuous* despite the fact that if E is an eigenvalue then so is $E+ndF$. Hence, one should not expect a discrete ladder of states. Secondly, it was argued that Houston functions and the crystal momentum representation, which both employ Bloch functions, are invalid for solving finite crystals with nonperiodic scalar potentials, since these functions are periodic at the boundaries but the actual solution may not be. Finally, it was argued that for an infinite crystal the operator x acting on the wave function diverges and therefore cannot be represented by Bloch states. The decade of debate was finally settled when Koss and Lambert reported an experimental observation of the Wannier-Stark ladder in gallium arsenide [17]. A review of this subject and the experimental work that has been done in superlattices is provided by Mendez and Bastard [19].

Krieger and Iafrate provide an alternate approach that avoids the above difficulties by considering a finite crystal (avoiding the third point), employing a gauge transformation of H to include the field as translational symmetry preserving vector potential instead of the scalar potential (avoiding the second criticism), and refraining from making any assumptions about the nature of the spectrum (avoiding the first issue raised by Zak). In this form, H is still periodic, and therefore the use of Houston functions (Bloch functions) is acceptable. In addition, by considering the time-dependent instead of the time-independent problem they avoid the issues of solving for energy eigenvalues. Essentially, there are no eigenstates, but only metastable resonances that eventually decay.

Although their results are equivalent to those derived by Houston and others, their analysis cleanly avoids the above difficulties, and because we will use it both for the interpretation of the Wannier-Stark data as well as for the estimation of the tunneling lifetimes of the accelerated states, we provide here a sketch of the derivation in the language of our optical potential. We begin with the transformed Hamiltonian, Eq. (5.5), which is analogous to the form where the electric field is described by a vector potential in lieu of a scalar potential (see Section A.2). In order to solve for the evolution of a state Ψ , we will expand it in the basis of “instantaneous solutions” of the time-dependent Schrödinger equation,

$$H\phi'_i = \left[\frac{(p - G)^2}{2M} + V(x) \right] \phi'_i = \epsilon_i \phi'_i = i\hbar \frac{\partial \phi'_i}{\partial t}, \quad (5.26)$$

where $G = M\dot{\alpha}$. If we make the substitution

$$\phi'_i = e^{iGx/\hbar} \phi_i, \quad (5.27)$$

then Eq. (5.26) reduces to the unperturbed Schrödinger equation

$$\left[\frac{p^2}{2M} + V(x) \right] \phi_i = \epsilon_i \phi_i, \quad (5.28)$$

with the usual Bloch solutions. We make the identifications

$$\phi_i = \psi_{n,k}(x) = e^{ikx} u_{n,k}(x) \quad (5.29)$$

and

$$\epsilon_i = \epsilon_n(k). \quad (5.30)$$

Now, because the lattice translational invariance is preserved with this choice of H , we can, with impunity, impose periodic boundary conditions at the edges of the crystal on the solutions ϕ'_i ,

$$\phi'_i(x, t) = \phi'_i(x + Nd, t), \quad (5.31)$$

where we let the length L of our crystal be N lattice periods: $L = Nd$. Using this condition, the form of ϕ_i , and Eq. (5.27), we get the condition

$$\frac{G}{\hbar} + k = n \frac{2\pi}{Nd}, \quad (5.32)$$

where n is some integer. Now we differentiate this equation and arrive at the semiclassical equation of motion

$$\dot{k} = \dot{G}/\hbar = F/\hbar \quad (5.33)$$

$$k = k_0 + Ft/\hbar. \quad (5.34)$$

So, the instantaneous solutions are

$$\phi'_i = e^{iGx/\hbar} \phi_{n,k(t)}(x), \quad (5.35)$$

where the functions $\phi_{n,k(t)}(x)$ are accelerated Bloch states or Houston functions [12]. Now, we expand an arbitrary state Ψ in terms of these solutions

$$\Psi(x, t) = \sum_i c_i(t) \phi'_i(x, t), \quad (5.36)$$

and plug this into the Schrödinger equation

$$i\hbar \frac{\partial}{\partial t} \sum_i c_i(t) \phi'_i(x, t) = \sum_i \epsilon_i c_i(t) \phi'_i(x, t). \quad (5.37)$$

After multiplying both sides by $e^{-iGx/\hbar} \phi_{n',k'}^*$ and integrating over all space, we get

$$\epsilon_{n,k} c_{n,k} = i\hbar \frac{\partial c_{n,k}}{\partial t} - iF \sum_m c_{m,k} W_{nm}(k), \quad (5.38)$$

where

$$W_{nm}(k) = \int_{-\infty}^{\infty} u_{n,k}^* \frac{\partial u_{m,k}}{\partial k} dx. \quad (5.39)$$

Using the substitution

$$c_{n,k(t)} = c_n(t) e^{-\frac{i}{\hbar} \int_0^t \epsilon_n(k(\tau)) d\tau}, \quad (5.40)$$

we have finally that

$$\dot{c}_n(t) = \frac{F(t)}{\hbar} \sum_m c_m(t) W_{n,m} e^{\frac{i}{\hbar} \int_0^t [\epsilon_n(k(\tau)) - \epsilon_m(k(\tau))] d\tau}, \quad (5.41)$$

where again $F(t)$ is an arbitrary time-dependent inertial force experienced by the atoms in a moving optical lattice. If initially the particles are in the lowest band $n = 0$ at quasimomentum $k = k_0$, then for sufficiently short times we can approximate Eq. (5.41) with just one term in the sum. Integrating this equation for the second band amplitude $n = 1$ gives

$$c_1(t) = \int_0^t \frac{F(t')}{i\hbar} W_{01}(k(t')) \exp \left[\frac{i}{\hbar} \int_0^{t'} [\epsilon_0(k(t'')) - \epsilon_1(k(t''))] dt'' \right] dt'. \quad (5.42)$$

If we assume that the force is constant,

$$k(t) = k_0 + \frac{Ft}{\hbar}, \quad (5.43)$$

and we evaluate the integral for N traversals of the Brillouin zone $[-K/2, K/2]$, where for an optical lattice $K/2 = \hbar k_L$, using the fact that both W and ϵ are periodic over $2k_L$, we have that

$$|c_1(N\tau_B)|^2 = |U|^2 \frac{\sin^2(N\beta)}{\sin^2(\beta)}, \quad (5.44)$$

where

$$\beta = \frac{1}{2F} \int_{-k_L}^{k_L} [\epsilon_0(k) - \epsilon_1(k)] dk \quad (5.45)$$

and

$$U = \int_{-k_L}^{k_L} W_{01}(k) \exp \left[\frac{i}{F} \int_0^k [\epsilon_0(k') - \epsilon_1(k')] dk' \right] dk. \quad (5.46)$$

If an oscillatory term $\cos(\omega t)$ is added to F as a probe of the spectral features, a result very similar to Eq. (5.44) is obtained. Treating the oscillatory term as a perturbation and assuming the constant term in F is small so that transitions due to tunneling are negligible, Krieger and Iafrate obtain the result

$$|c_1(N\tau_B)|^2 \approx |U'|^2 \frac{\sin^2(N\beta')}{\sin^2(\beta')} \quad (5.47)$$

where now

$$\beta' = \frac{1}{2F} \int_{-k_L}^{k_L} [\epsilon_0(k) - \epsilon_1(k) \pm \hbar\omega] dk \quad (5.48)$$

and

$$U' = \int_{-k_L}^{k_L} p_{01}(k) \exp \left[\frac{i}{F} \int_0^k [\epsilon_0(k') - \epsilon_1(k') \pm \hbar\omega] dk' \right] dk, \quad (5.49)$$

where the matrix element W of $\frac{\partial}{\partial k}$ has been replaced with the matrix element of $p = -i\hbar \frac{\partial}{\partial x}$.

5.2.1 Wave interference: the spectral ladder and tunneling resonances

The form of Eqs. (5.44) and (5.47) is analogous to the optical interference pattern generated by N coherent sources or by N slits illuminated by a plane wave [67]. In fact, the analogy is exact when one considers the problem in one dimension. The interpretation is that each crossing of the Brillouin zone acts as a temporal slit that contributes to the transmission amplitude $|c_1(t)|$ in the same way as do multiple spatial slits in the case of optical interference. Using L'Hospital's rule, we see that this wave interference produces maxima in the transmission probability,

$$\left. \frac{\sin^2(N\beta)}{\sin^2(\beta)} \right|_{\beta=n\pi} = N^2, \quad (5.50)$$

when β is an integer multiple of π . We define the average band gap as

$$\bar{\epsilon}_g = \frac{1}{2k_L} \int_{-k_L}^{k_L} [\epsilon_0(k) - \epsilon_1(k)] dk, \quad (5.51)$$

so that $\beta = 2k_L \bar{\epsilon}_g / 2F$. Using the definition of the Bloch frequency, the resonant condition with no oscillatory drive is

$$\bar{\epsilon}_g / h = n\nu_B, \quad (5.52)$$

and the condition with the drive is

$$\bar{\epsilon}_g/h \pm \nu = n\nu_B. \quad (5.53)$$

These two resonant conditions contain the essence of the Wannier-Stark ladder. This second condition when solved for the probe frequency,

$$|\nu| = \bar{\epsilon}_g/h + n\nu_B, \quad (5.54)$$

shows that there exist spectral resonances in the $1 \rightarrow 2$ transition that are spaced by integer multiples of the Bloch frequency and centered at a frequency corresponding to the average band gap. Our interpretation is that there exists a centered ladder for each band. The weak spectral probe ν couples these states, driving transitions when on resonance. This situation is depicted in Fig. 5.2.

The first condition, Eq. (5.52), describes resonances in the tunneling rate, the rate of interband transitions induced by the acceleration itself. These resonances occur when an integer n times the Bloch frequency equals the average band gap. The interpretation here is that at this value for the acceleration and well depth, the bound Wannier-Stark states in the first band are *degenerate* in energy with states in the second band n lattice sites over. Since the tunneling rate is proportional to the density of final states evaluated at the energy of the bound state, when this degeneracy occurs, the density of final states is very large and therefore the rate is enhanced. This subject is discussed in more detail in Section 6.4.

5.3 Observation of the Wannier-Stark ladder

In order to observe the spectral resonances generated in an accelerating optical lattice, we introduced a weak time-dependent modulation (frequency ν_p) of the standing wave position which could induce these interband transitions as indicated by the arrows in Fig. 5.2. The full potential in the lab frame has the form

$$V_0 \cos[2k_L(x - \alpha(t))], \quad (5.55)$$

where

$$\alpha(t) = \frac{1}{2}at^2 + \frac{\delta}{2k_L} \cos(2\pi\nu_p t). \quad (5.56)$$

As was mentioned earlier, this potential expressed in the accelerating frame (the transformations are outlined in the Appendix, Section A.2) is

$$V_0 \cos(2k_L x) + xaM + Mx \frac{\delta(2\pi\nu_p)^2}{2k_L} \cos(2\pi\nu_p t). \quad (5.57)$$

The well depth was chosen such that the tunneling rate out of the first band for the accelerations considered was negligible over the time scale of the experiment, but the rate from the second to the third band was quite high. Under these conditions, once an atom makes a transition out of the trapped band, it quickly tunnels out of the second band and effectively becomes a free particle, no longer accelerating with the potential. For each run we measured the survival probability for a given probe frequency, and we observed the resonances spaced by the Bloch frequency that constitute the atomic Wannier-Stark ladder [68].

A complimentary study of Bloch oscillations, the time-dependent dual of the Wannier-Stark ladder, was performed almost simultaneously by Christophe Salomon's group in Paris at the ENS [22]. In this experiment, a stimulated-Raman-cooled sample of cesium atoms was trapped in an accelerating optical lattice, and the ensemble velocity was measured as a function of time. The

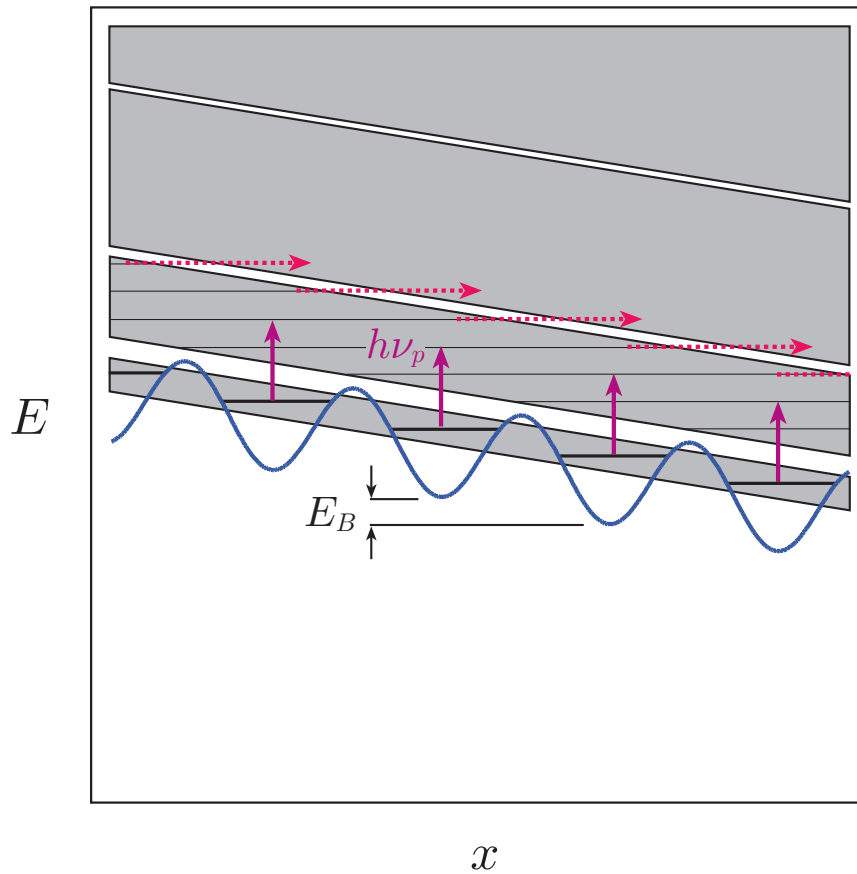


Figure 5.2: Schematic of the centered Wannier-Stark ladders superimposed on each band. The weak spectral probe ν_p couples these states, driving transitions when on resonance. After the particle makes the transition out of the first band, it easily crosses the successive band gaps, becoming essentially a free particle. $E_B = h\nu_B$

velocity evolution clearly showed Bloch oscillations superimposed on the linear acceleration experienced by the atoms in the first band. For this experiment, it was crucial that a sub-recoil distribution well localized in k was used, since each Houston state in the band starts with a different phase. Without state-selective velocity detection, an average over many values of k in the first Brillouin zone would have smeared out the oscillations. By a careful measurement of the velocity evolution, they were able to reconstruct the dispersion curve for the fundamental and second bands.

In Section 5.2.1 we saw that the resonance condition for the probe drive is

$$|\nu_p| = \bar{\epsilon}_g/h + n\nu_B, \quad (5.58)$$

where $\bar{\epsilon}_g$ is the average band gap and the Bloch frequency is given by

$$\nu_B = \frac{F}{2\hbar k_L} = \frac{a}{2v_r}, \quad (5.59)$$

where $2v_r = 0.0589$ m/s is twice the recoil velocity. From this condition, it is clear that the absolute position of these resonances is tied to the band gap, which is proportional to V_0 at these low well depths (see Section 3.7.1). For this reason, any change of the well depth – spatial or temporal – experienced by the atoms will lead to a shift in frequency of the resonances. In order to obtain a spectrum, we average over many experimental runs, each with a slightly different well depth; therefore, the measured peaks were broadened by the variation of the well depth about its mean value. For most of these experiments the average band gap was on the order of 100 kHz, so a variation of the well depth of 10 % would result in a 10 kHz shift. The smallest spacing measured was 10 kHz for an acceleration of 600 m/s².

Although we monitored the power in each constituent beam of the standing wave during the experiment and we discriminated the data to remove shot-to-shot variations greater than 1%, we did not discriminate variations

during each run to better than 5%. Another known systematic variation in the well depth was due to atomic motion transverse to the standing-wave axis. The transverse Gaussian profile of the laser beams produces a position-dependent well depth, and consequently any radial motion produces a time-dependent variation in the well depth. This effect is small, but not completely negligible, since our interaction times are on the order of 1ms and an atom moving at $2\sigma_v = 10$ recoils = .3 m/s (where σ_v is determined by the temperature of the MOT) will travel almost 300 μm . For a beam size of $\sigma = 2$ mm, this motion would result in a 1% variation in the well depth. One method we employed to reduce the systematic error associated with this effect was to count only those atoms that were cold in the transverse direction. By choosing a narrow horizontal window aligned along the standing wave axis for the two dimensional images acquired by the CCD camera, we included only those atoms which were relatively cold in the transverse direction in the image plane. This method did not exclude hot atoms in the dimension perpendicular to the image plane, but nonetheless reduced the widths of the measured resonances. The well depth variation across the initial MOT distribution was negligible since it was a spatial Gaussian with a width of $\sigma_x = 0.12$ mm.

Another source of broadening is phase noise in the standing wave due to mirror vibrations and electronic noise in our AO drivers. This phase noise can be viewed as a broadening mechanism for the acceleration or for the probe modulation. This noise was measured by heterodyne detection to have a spectral width of approximately 10 kHz.

In Fig. 5.3, a measured Wannier-Stark spectrum is shown for an acceleration of 1100 m/s^2 and $V_0 = 0.461$. The peak spacing is approximately 18.6 kHz, corresponding to the Bloch frequency at this acceleration. A series of experimental runs were all done at a well depth of $V_0 = 0.458$, each with a different acceleration. The peak locations were determined in each case and

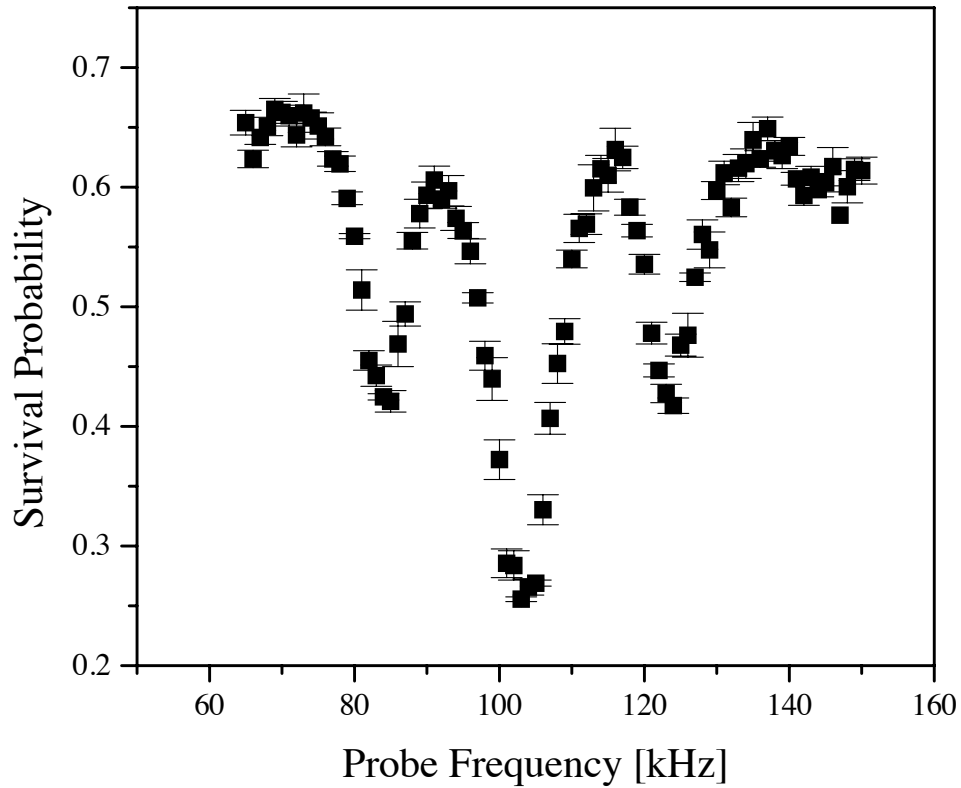


Figure 5.3: Wannier-Stark ladder resonances for a well depth of $V_0 = 0.461$ and an acceleration of $a = 1100 \text{ m/s}^2$. The Bloch frequency for this acceleration is 18.6 kHz. The center peak corresponds to the average band gap between the first and second band. For the well depth determined by beam measurements, $\bar{\epsilon}_g = 0.521$, which corresponds to a frequency of 104.2 kHz and is in good agreement with the central peak.

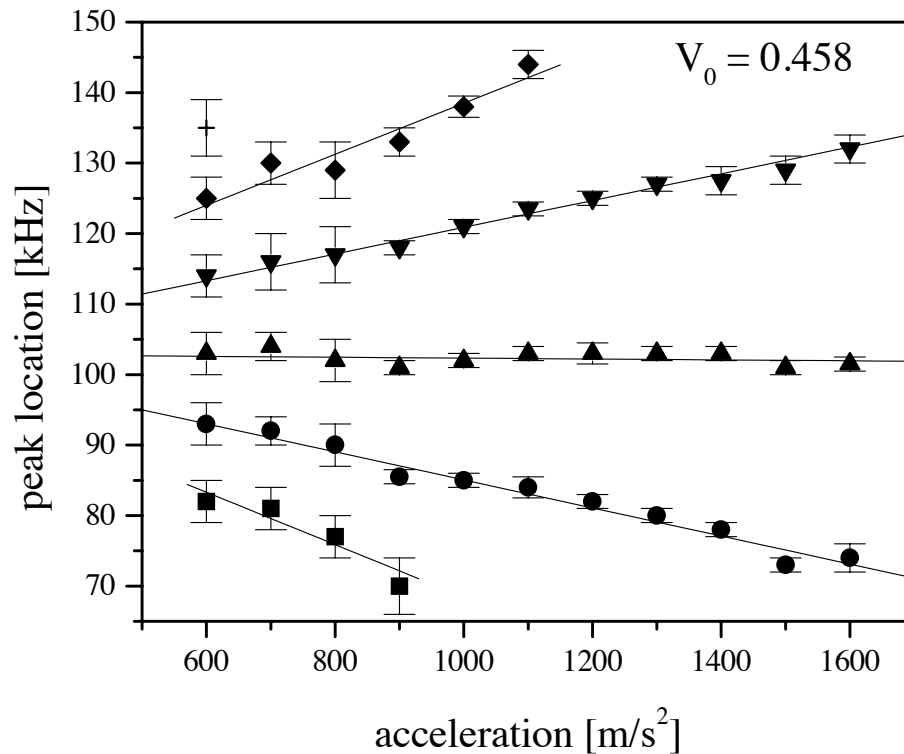


Figure 5.4: The fan of Wannier-Stark resonances for a well depth of $V_0 = 0.458$. The position of the center state is independent of acceleration and corresponds to the average band gap, which is $\bar{\epsilon}_g = 0.519 \leftrightarrow 104$ kHz for this choice of V_0 .

are shown in Fig. 5.4 by what is typically referred to as a “fan” chart of the Wannier-Stark resonances. As predicted by Eq. (5.58), there is one resonance at a frequency corresponding to the average band gap, and this resonance does not move as the acceleration is varied. The well depth calculated from our detuning, power, and beam diameter measurements was $V_0 = 0.458$. For this well depth, the average band gap (calculated numerically) is $\bar{\epsilon}_g = 0.519$, which corresponds to a frequency of 104 kHz. This value for the center state agrees well with our experimentally measured resonance. All of the other states move out with a slope given by an integer times the Bloch frequency.

5.4 Observation of the fractional Wannier-Stark ladder

If a strong AC modulation of frequency ω_s is added to the acceleration and the weak AC probe, then the Wannier-Stark spectrum is predicted to develop additional resonances [68]. In particular, if ω_s matches the Bloch frequency by a fractional factor q/p , the spectrum will become a fractional ladder with a spacing p times smaller.

For this experiment, the potential in the lab frame has the form

$$V_0 \cos[2k_L(x - \alpha(t))], \quad (5.60)$$

where

$$\alpha(t) = \frac{1}{2}at^2 + \frac{\delta}{2k_L} \cos(2\pi\nu_p t) + \frac{\Delta}{2k_L} \cos(2\pi\nu_s t). \quad (5.61)$$

Fig 5.5 shows a series of three spectra taken at three different values for the strong modulation frequency $\nu_s = (0, \frac{1}{2}, \frac{2}{3}) \cdot \nu_B$. The fractional resonances were difficult to resolve, for various reasons. Perhaps the most problematic issue was variation of the well depth during each run. Since the fractional peaks are on the order of a few kilohertz wide and spaced by $(\frac{1}{2}, \frac{1}{3}) \cdot 17$ kHz, a change of 1% of V_0 will shift them by more than half their width. The best results were obtained by choosing an acceleration of 1000 m/s² (for which the peaks were relatively far apart) and a well depth of $V_0 = 0.4$. The probe strength was the same as that used to detect the normal ladder ($\delta = 0.05$), and the strong AC drive amplitude found to produce the best results was $\Delta \approx 2.5$. When a larger Δ was used, the peaks washed out. When Δ was made smaller, the fractional peaks disappeared. We also noticed a sensitivity to the exact frequency matching. When ν_s was tuned 2% away from the rational fraction of ν_B , the fractional peaks would disappear into the baseline.

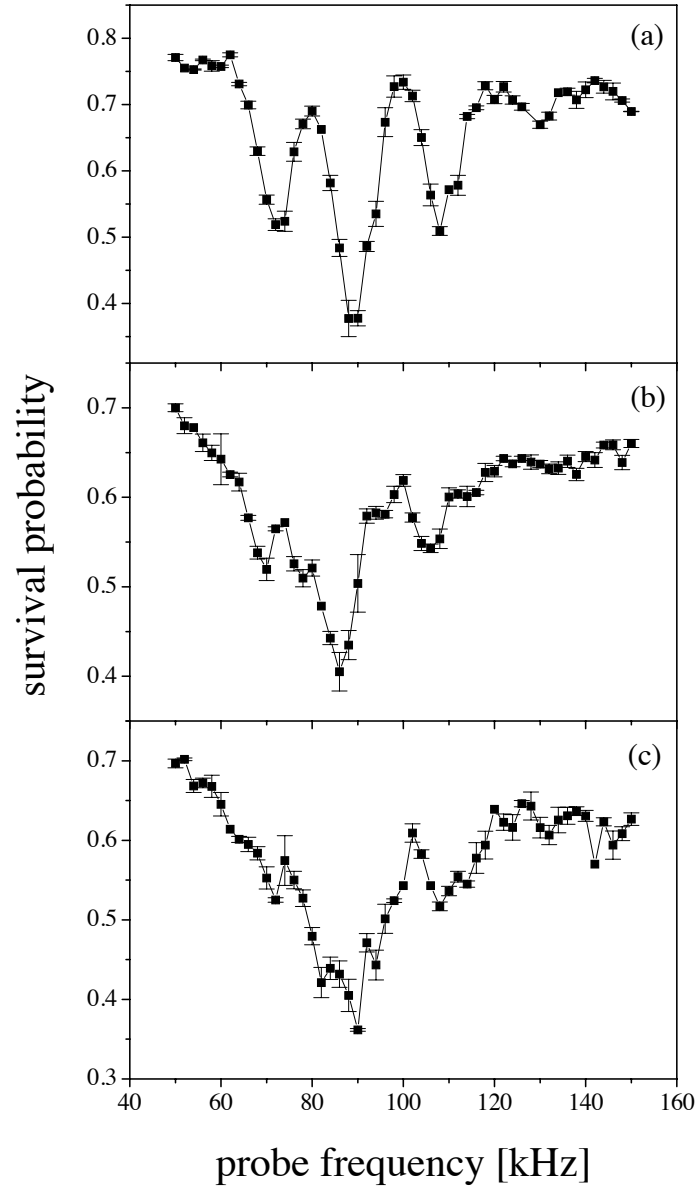


Figure 5.5: Fractional Wannier-Stark ladders for a well depth of $V_0 = 0.4$, an acceleration of $a = 1000 \text{ m/s}^2$, and three values of ν_s : (a) $\nu_s = 0$, (b) $\nu_s = \frac{1}{2}\nu_B$, and (c) $\nu_s = \frac{2}{3}\nu_B$ where the Bloch frequency is approximately 17 kHz. Evidence of peaks developing between the normal Wannier-Stark resonances at a spacing of $\frac{1}{2}, \frac{1}{3} \times \nu_B$ can be seen by comparing plots (b) and (c) with (a).

Chapter 6

Quantum tunneling

In this chapter we consider the time-dependent behavior of atoms in an accelerating optical lattice. In contrast to Chapter 5, where we were interested in the time-independent spectral distributions of the quasi-eigenstates resulting from small accelerations, we are interested here in the behavior of the system when the acceleration is not small. In this limit, the lifetime of the Wannier-Stark states becomes short enough to measure, providing a simple experimental tool for the study of quantum tunneling. The center of mass tunneling of an atom from an accelerating optical lattice is identical to the phenomenon of Landau-Zener tunneling of an electron between, say, the valence and conduction bands due to the application of a homogeneous electric field. This interband tunneling is distinct from the Bloch tunneling discussed in Section 3.5.2. In the latter case, a spatially localized state “decays” to a delocalized superposition; however, neither the quasimomentum nor the band index change.

6.1 Introduction: an atom accelerator

Our initial impetus for developing an atom accelerator was the realization of an atom interferometer with very slow beams. Unlike previous interferometers that used fast atomic beams emerging from ovens or supersonic nozzles at up to a thousand meters per second [52, 69, 70], we hoped to implement

the techniques of laser cooling to produce a very bright and slow moving source that has several distinct advantages over the former type. Perhaps the primary advantage is that the interaction times, which set an ultimate limit on the interferometer's resolution, achievable with a slow beam can be orders of magnitude longer than for the fast beam. Moreover, a slow beam can have a much larger opening angle in the case of a Mach-Zehnder interferometer, facilitating the isolation of the two paths. Another advantage is that laser cooling reduces the size and velocity in all three dimensions, thus eliminating the need to pre-select atoms entering the interferometer region. Of course, what matters is not the brightness but the throughput of the interferometer, which can be made larger at the expense of size and simplicity.

In order not to spoil the brightness of the laser-cooled source, we needed a method to launch the beam without dissipation or heating. This requirement precluded the use of spontaneous emission methods like a pushing beam of resonant light. Our solution was to trap the atoms in the lowest band of a one-dimensional optical lattice and then accelerate the lattice adiabatically by imposing a linear chirp in the frequency difference of the two constituent beams $\nu_1 - \nu_2$. The velocity of the standing wave is

$$v = \frac{\lambda}{2}(\nu_1 - \nu_2), \quad (6.1)$$

where λ is the wavelength of the light. This method not only avoids the transverse heating incurred with spontaneous emission processes but, in addition, perfectly preserves the initial longitudinal velocity profile of the sample, given that the lattice is turned on adiabatically [37].

6.1.1 The classical limit for this atom accelerator

In order to determine the limitations of such an atom accelerator, we begin with a classical analysis. An atom accelerating with the lattice experiences a

potential of the form

$$V(x) = V_0 \cos(2k_L x) - xaM, \quad (6.2)$$

where the linear term is due to the inertial force. In order for an atom to be accelerated, the force due to the cosine must always exceed or at least equal the inertial force. The forces acting on the atom are given by

$$F(x) = -\frac{\partial V(x)}{\partial x} = -2k_L V_0 \sin(2k_L x) + Ma, \quad (6.3)$$

and we see the maximum acceleration that can be sustained is

$$a_{cl} = \frac{2k_L V_0}{M}. \quad (6.4)$$

As long as this acceleration is not exceeded, there exist local minima in the potential and therefore classical turning points. This situation is depicted in Fig. 6.1. Although there exist bound orbits for accelerations less than a_{cl} , the effective well depth decreases monotonically with a . We define the effective well depth as half the energy difference between a local minimum and the nearest maximum. The critical points in the potential are given by

$$x_n = \frac{1}{2k_L} \left[\sin^{-1} \left(\frac{a}{a_{cl}} \right) + 2n\pi \right], \quad (6.5)$$

where n is an integer. Being careful to take the nearest minimum and maximum, the effective well depth is found to be

$$V_{\text{eff}}(a) = V_0 \left| \sqrt{1 - \left(\frac{a}{a_{cl}} \right)^2} - \frac{a}{a_{cl}} \left(\cos^{-1} \left(\frac{a}{a_{cl}} \right) \right) \right|, \quad (6.6)$$

where $a \leq a_{cl}$. Clearly, when a is equal to a_{cl} there are no more minima and the effective well depth is zero. Although the volume of trapped states decreases with a in this way, for a fixed acceleration, a particle in a trapped state will remain there, accelerating with the potential for an indefinite period of time. This is in stark contrast with the phenomenon of tunneling predicted

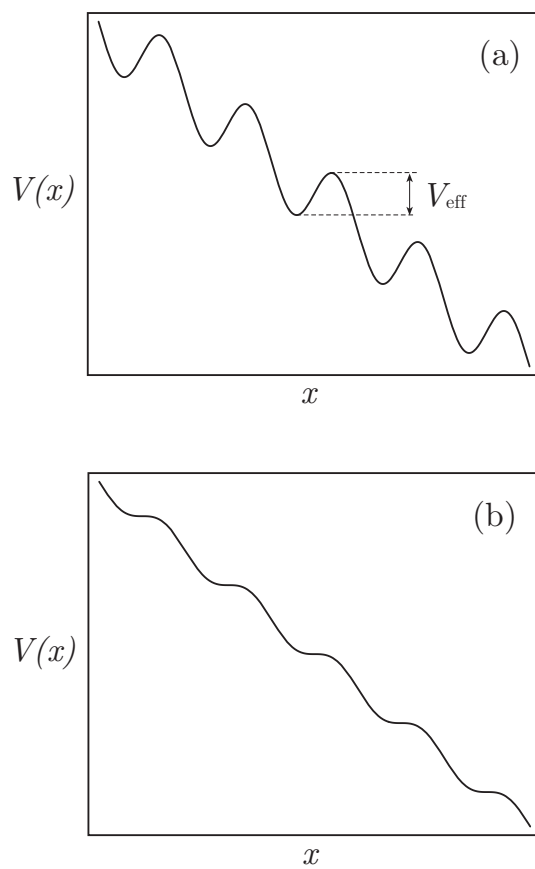


Figure 6.1: The tilted potential plotted at two different accelerations: (a) $a < a_{\text{cl}}$ and (b) $a = a_{\text{cl}}$.

by quantum mechanics, in which the particle *always* has a non-zero probability of escaping from the potential, and so it will inevitably cease to be accelerated after some time. The ultimate limit of this coherent, atom accelerator is therefore set by the tunneling rate, which will be calculated in Sections 6.3.1 and 6.3.2.

6.2 Observation of quantum tunneling: is the observed loss really due to tunneling?

Before proceeding with the analysis of tunneling rates for this atom accelerator, I would like to present our observation of atomic tunneling and discuss a few important experimental issues. In Fig. 6.2, the survival probability of the first band is plotted on a logarithmic scale versus the duration of the acceleration, and the evolution is described well by an exponential decay law. However, in order to be sure that the loss of atoms was due to tunneling, it was necessary to rule out other loss mechanisms that would also produce an exponential decay.

The loss mechanisms for the optical potential other than tunneling include amplitude and phase noise of the constituent beams, abrupt switching between different accelerations, and spontaneous scattering. The phase noise of the potential was characterized by an optical homodyne measurement, as described in Chapter 2. It was found that the frequency and amplitude of the phase noise in this experiment was far below that required to drive a measurable number of atoms out of the first band, as was done in the Wannier-Stark ladder experiments of Chapter 5. The amplitude of the standing wave was monitored in real time with fast photodiodes, and traces with significant amplitude variations were rejected.

Since the population of the first band is prepared by imposing a small

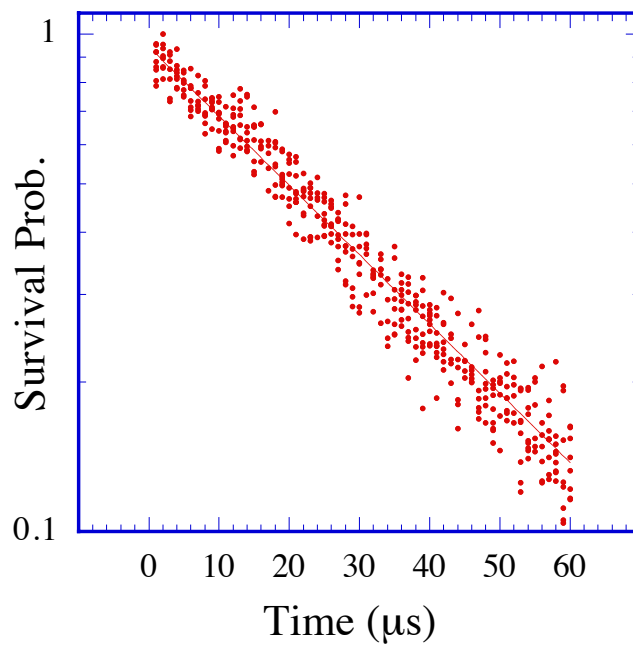


Figure 6.2: Survival probability as a function of the duration of the tunneling acceleration. Here $V_0 = 0.25$ and $a_{\text{tunnel}} = 4500 \text{ m/s}^2$. Note that the vertical axis is logarithmic.

acceleration prior to the large tunneling-acceleration, there was some concern that the transition, which contains high acceleration components, could possibly induce a loss. Naïvely, this loss would be incurred twice, once at each acceleration switch (see Fig. 2.13), and it would constitute a constant loss independent of the acceleration duration. For this reason, it was expected that it would simply shift the overall decay curve down by some amount. We attempted to study this loss process by smoothing the velocity profile. However, the losses, if indeed there were any, due to these effects were below our detection ability.

The final loss mechanism considered is due to the spontaneous scattering of a photon. The net atomic recoil projected along the standing-wave axis is in the range $[0, 2\hbar k_L]$ corresponding to a kinetic energy imparted to the atom of up to $4\omega_r = \frac{1}{2}E_u$ (see Section 3.1 for the definition of the scaled units). Since the first band gap is on the order of $V_0 = 0.275E_u$, we see that the probability of escaping the first band due to a single spontaneous scattering event is significant. The presence of even $1 \mu\text{W}/\text{cm}^2$ of the resonant MOT light would produce on the order of a spontaneous scattering event every 5 ms, and so a MOT inhibit channel was added to the experiment, which disconnected the AOM oscillator from the crystal during the interaction to prevent any light leakage through the 1st diffraction order to the chamber. A second source of spontaneous scattering is the far detuned lattice itself. In principle, this effect can be made negligibly small by simply detuning farther away and then compensating by increasing the amplitude of the constituent beams. For the experiment presented here, the spontaneous scattering probability was estimated to be 10% per millisecond. Since the period of large acceleration was at most $200 \mu\text{s}$, the probability for a spontaneous event was negligible. One easy systematic check exploits the fact that the spontaneous rate, and therefore (for low accelerations) the corresponding loss, is independent of acceleration.

Since there was no appreciable loss during the transport accelerations, and since our measured values of the decay rates were in good agreement with the predictions for tunneling (in the absence of this dissipative effect), we were confident that it was not a problem.

6.3 Theoretical analysis of interband tunneling

6.3.1 Zener breakdown

The phenomenon of tunneling in this system can be visualized in two equivalent ways: one corresponding to the position, and the other the momentum representation of the dynamics. The first picture was employed by Zener in his analysis of the electrical breakdown of dielectrics [16]. There are two phenomena responsible for dielectric breakdown, Zener breakdown and avalanche breakdown. The latter occurs when electrons are excited out of the lower-lying valence bands via collisions with energetic conduction band electrons. Zener breakdown is more analogous to the auto-ionization of a free gas, in which an electron tunnels from a bound state to the continuum because of a large applied electric field.

We begin by considering that an atom accelerating with the lattice experiences, in addition to the sinusoidal part, a linear term due to the inertial force $F = Ma$. The wave equation for this situation is

$$\left[\frac{p^2}{2M} - V_0 \cos(x) + (E - xaM) \right] |\psi(x)\rangle = 0. \quad (6.7)$$

Following Zener's analysis, we assume that the linear term changes only slightly over a lattice period and so the band structure is preserved. The tilted potential with the allowed bands is shown in Fig. 6.3. An atom in the lowest band can be thought of as occupying a state with some energy E bound to the left by the potential and to the right by the first band gap. By penetrating the barrier presented by this gap, the atom can escape the first band into the second,

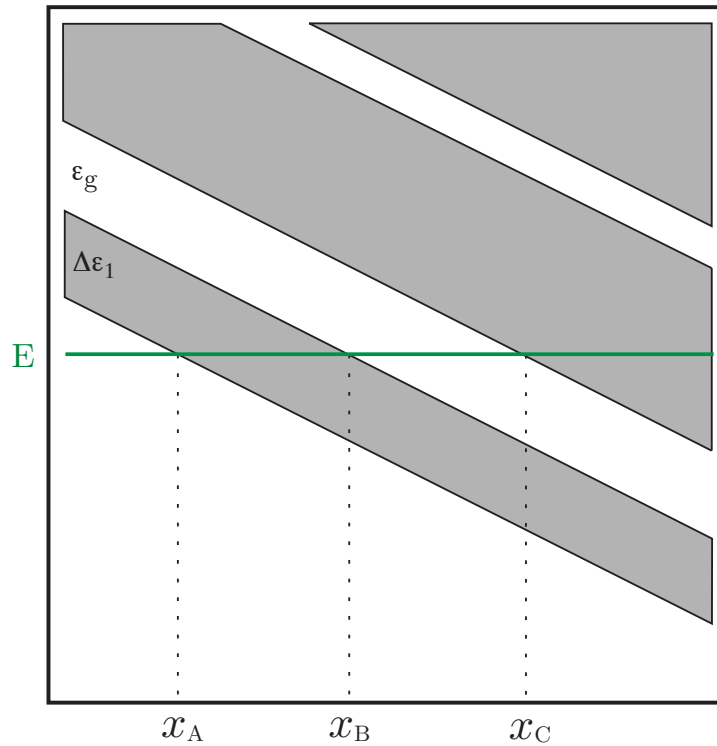


Figure 6.3: Schematic of tilted bands. The points x_A and x_B are the classical turning points for a particle bound in the lowest band. It accelerates up to the band edge x_B , where it is Bragg reflected. It then climbs the plane to x_A where it turns around to complete the Bloch oscillation. By penetrating the forbidden region (plotted in white), the particle can tunnel to the second band and emerge at x_C .

and then into the third, and so on. As was shown in Chapter 5, the velocity of the particle oscillates at the Bloch frequency and therefore periodically reflects from the band gap each time with some probability p of penetration. The probability per unit time is then the product $p \cdot \nu_B$. where p is given by

$$p = \left| \frac{\psi(x_C)}{\psi(x_B)} \right|^2. \quad (6.8)$$

In order to estimate p , Zener takes as a solution to the wave equation a Bloch function with a spatially dependent quasimomentum and energy,

$$|\psi(x)\rangle = e^{i \int k(x') dx'} u_{k(x)}(x), \quad (6.9)$$

where the quasimomentum k is real only for certain values of x . In the range $[x_A, x_B]$ E lies in the first band, and therefore k is real; however, in the band gap $[x_B, x_C]$, k will be complex, and $\psi(x)$ will decrease exponentially. After solving for the complex part η of k and approximating

$$\left| \frac{\psi(x_C)}{\psi(x_B)} \right|^2 \approx e^{-2 \int_{x_B}^{x_C} \eta dx}, \quad (6.10)$$

Zener concludes that the tunneling rate is

$$\gamma = \nu_B \exp\left(-\frac{\pi^2 M d \epsilon_g^2}{h^2 F}\right), \quad (6.11)$$

where d is the lattice periodicity, and ϵ_g is the width of the gap. Making the substitutions for the case of atoms in an optical lattice, $F = Ma$ and $d = \pi/k_L$, Eq. (6.11) becomes

$$\gamma = \nu_B e^{-a_c/a} \quad (6.12)$$

where

$$a_c = \frac{2\pi(\frac{\epsilon_g}{2})^2}{2\hbar^2 k_L} \quad (6.13)$$

is the critical acceleration.

6.3.2 Landau-Zener theory of non-adiabatic transitions

The second picture of this tunneling process is viewed in reciprocal space. Making the same assumption as in the previous picture, that the band structure is preserved for small accelerations, we find that an atom in the lowest band with a quasimomentum k will simply translate at a constant “velocity” in k -space until it hits the band edge. At this point, the atom can either reflect from the band edge remaining in the same band or it can jump the band gap into the second band. As we saw in Chapter 3, the band gaps are actually avoided crossings of the free-particle energies. Therefore, at a sufficiently high acceleration, an atom will make a non-adiabatic transition through the gap and continue up the dispersion curve as if it were a free particle. In 1932, Clarence Zener considered the question of non-adiabatic crossings of energy levels and found that the transition probability after one pass through the avoided crossing is given by

$$P = \exp\left(-\frac{(2\pi)^2}{h}\epsilon_{12}^2 \left/ \left| \frac{d}{dt}(\epsilon_1 - \epsilon_2) \right| \right.\right), \quad (6.14)$$

where ϵ_{12} is the coupling strength and equal to half the energy difference between the two levels ϵ_1 and ϵ_2 [15]. For the case at hand, ϵ_{12} is half the band gap. We can approximate the two energy functions by the free particle curves

$$\epsilon_1 = \frac{p_1^2}{2M}, \text{ where } p_1 = taM \quad (6.15)$$

$$\epsilon_2 = \frac{p_2^2}{2M}, \text{ where } p_2 = 2\hbar k_L - taM, \quad (6.16)$$

which gives the following for the time derivative of their difference:

$$\left| \frac{d}{dt}(\epsilon_1 - \epsilon_2) \right| = (2\hbar k_L)a. \quad (6.17)$$

Substituting Eq. (6.17) into into Eq. (6.14) gives

$$P = e^{-a_c/a}, \quad (6.18)$$

where the critical acceleration was defined above as

$$a_c = 2\pi\left(\frac{\epsilon_{12}}{2}\right)^2/2\hbar k_L. \quad (6.19)$$

Since the atom is performing Bloch oscillations, it encounters the gap every Bloch period. Therefore the probability per unit time to make the interband transition is

$$\gamma = \nu_B e^{-a_c/a}, \quad (6.20)$$

which is precisely what was obtained in the previous section. Given this rate of decay, the survival probability as a function of time will be

$$P_{\text{surv}}(t) = e^{-\gamma t}. \quad (6.21)$$

6.4 Observation of deviations from the Landau-Zener prediction

In Chapter 5, the existence of the Wannier-Stark ladder was shown to produce absorption resonances, which were experimentally measured with a sinusoidal weak probe. The existence of these states also led to a resonantly enhanced tunneling rate between bands. These resonances occur when an integer n times the Bloch frequency equals the average band gap. The interpretation here is that at this value for the acceleration and well depth, the bound Wannier-Stark states in the first band are *degenerate* in energy with states in the second band n lattice sites over. This situation is depicted in Fig 6.4. Since the tunneling rate is proportional to the density of final states evaluated at the energy of the bound state, when this degeneracy occurs, the density of final states is very large and therefore the rate is enhanced. One would expect the lifetime at these special points to be shorter than Landau-Zener theory. Moreover, the Wannier-Stark resonances will be separated by voids in the continuum where the density of states is far less than the average density. This is a

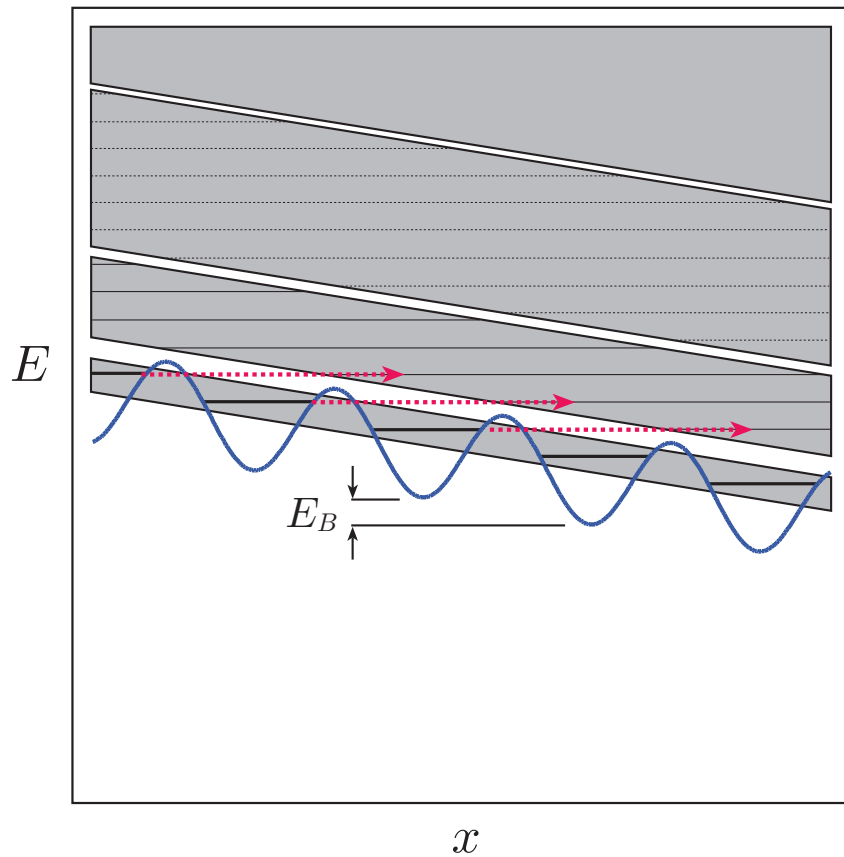


Figure 6.4: Schematic of the band structure and Wannier-Stark resonances for an acceleration matching the resonant tunneling condition. Because the continuum at the energy of the unstable state contains a Wannier-Stark resonance, the tunneling rate is enhanced, and the Landau-Zener prediction for the lifetime is unreliable.

consequence of the fact that the sum the matrix elements $W_{nm}(k)$ (defined by Eq. (5.39) of Section 5.2.1) over the entire band is conserved [71] (given that the bands are still a valid picture). At these points, one expects that the lifetime is much longer than predicted by Landau-Zener theory. Moreover, the width of the resonant condition is related to the width of the Wannier-Stark state. For this reason, the resonances become sharper and more pronounced for lower accelerations. Indeed, the lifetime shows such deviations from the L-Z prediction. In Fig. 6.5 the lifetimes are plotted as a function of acceleration, and the deviations from L-Z theory are in accord with the above discussion [3].

The resonance condition, derived in Section 5.2.1, is

$$\bar{\epsilon}_g/h = n\nu_B, \quad (6.22)$$

where n is an integer, $\bar{\epsilon}_g$ is the average band gap, and the Bloch frequency is

$$\nu_B = \frac{a}{2v_{\text{recoil}}} = \frac{a}{0.0589 \text{ m/s}}. \quad (6.23)$$

The resonance condition expressed for the acceleration is then

$$a = \frac{2v_{\text{recoil}}\epsilon_g}{nh}. \quad (6.24)$$

By measuring at lower accelerations than the experiment shown in Fig. 6.5, more resonances were resolved. Fig. 6.6 shows lifetime measurements taken at accelerations as low as 800 m/s^2 . The position of the resonances agree well with their predicted locations. Since the well depth was $V_0 = 0.228$, the average band gap was $\bar{\epsilon}_g = 0.356$ leading to resonance enhanced tunneling when the acceleration was $a \approx (4200\text{m/s}^2)/n$. For very large accelerations, the lifetime is seen to approach the Landau-Zener prediction. This is physically reasonable because the tunneling rate out of the second band dominates any coherent Bloch oscillations. At this point, the continuum is homogeneous, and no deviations are expected. This situation is depicted in Fig. 6.7.

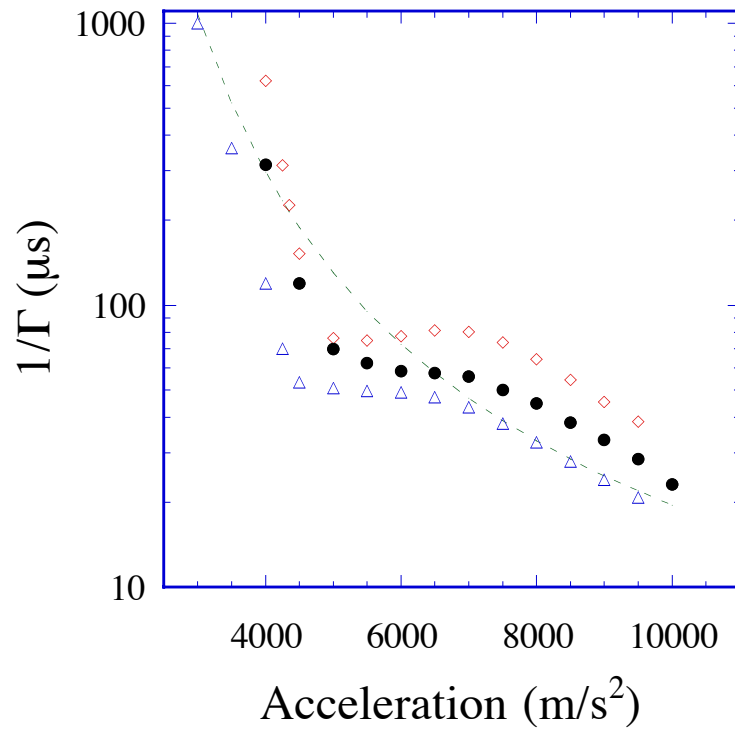


Figure 6.5: Tunneling lifetime versus acceleration. The experimental data are marked by solid dots. The uncertainty in the exponential fits that determine Γ are typically $\pm 2\%$, and the uncertainty in the acceleration for the range shown is $\pm 50 \text{ m/s}^2$. The dashed line is the prediction of Landau-Zener theory. The experimental well depth was $V_0 = 0.36$ with an uncertainty of $\pm 10\%$. The data are bracketed between quantum simulations for well depths of $V_0 = 0.30$ (empty triangles) and $V_0 = 0.36$ (empty diamonds), and the L-Z prediction is for an intermediate value of $V_0 = 0.33$. Only the first resonance is seen, which should occur at an acceleration of $5,290 \text{ m/s}^2$ and a well depth of $V_0 = .36$.

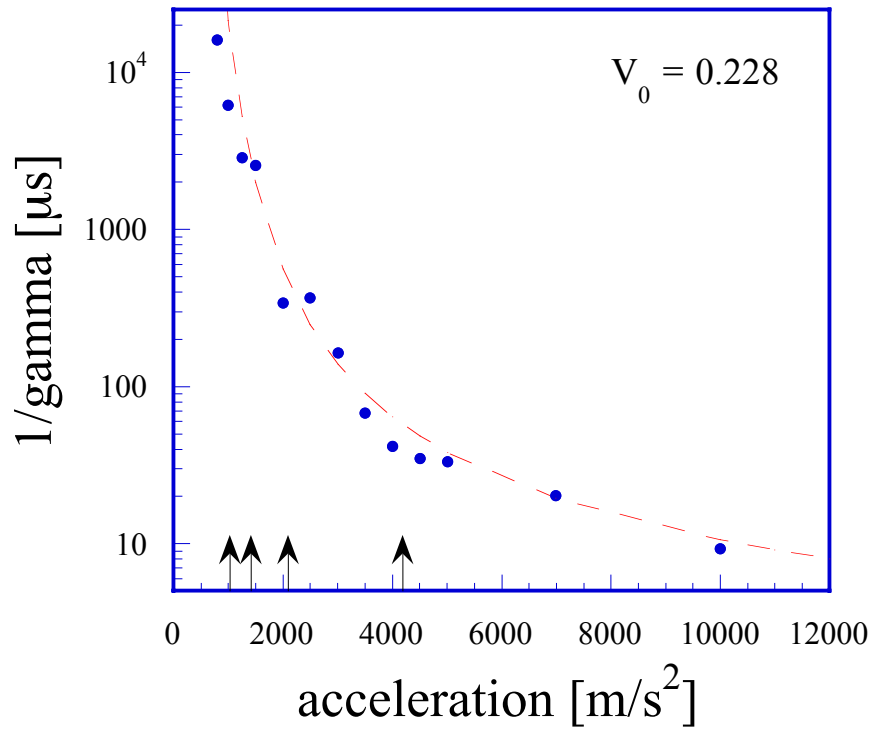


Figure 6.6: Tunneling lifetime versus acceleration for a well depth of $V_0 = 0.228$. The experimental data are marked by dots, and the Landau-Zener prediction for the lifetimes is indicated by the dashed line. In this plot, several tunneling resonances can be seen. The average band gap is $\bar{\epsilon}_g = 0.356$ leading to resonance-enhanced tunneling when the acceleration is $a \approx (4200\text{m/s}^2)/n$ where n is an integer. The predicted locations for the resonances are indicated by arrows, and the experimentally measured lifetimes indeed reflect these resonances.

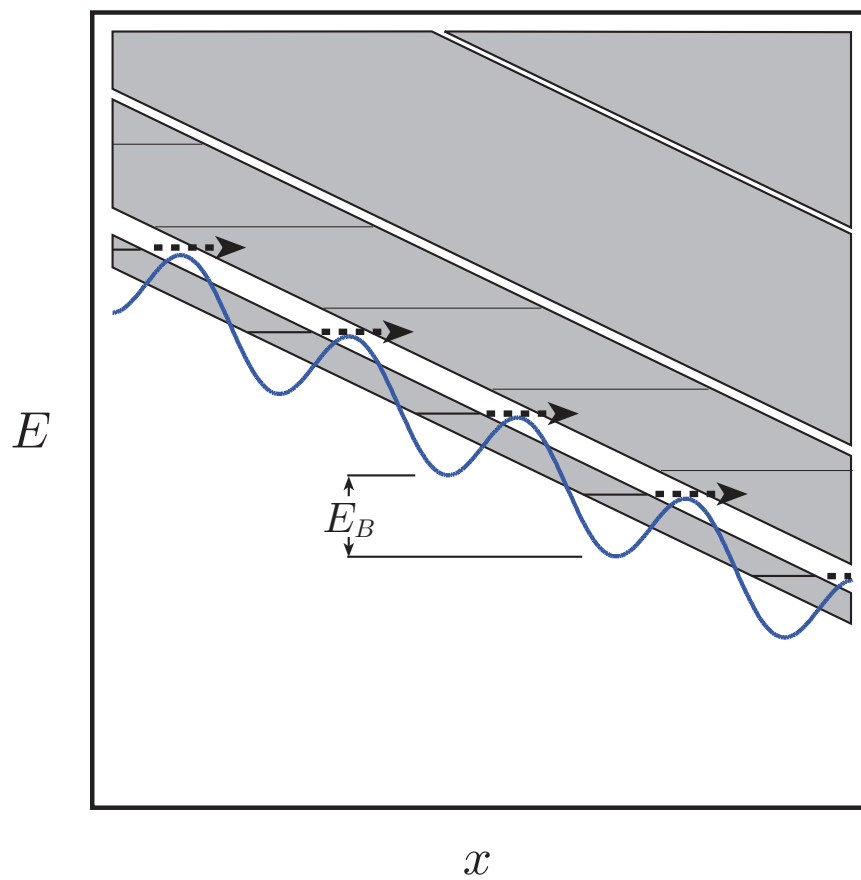


Figure 6.7: Schematic of the band structure and Wannier-Stark resonances for an acceleration exceeding the first resonant tunneling condition. Because the continuum at the energy of the unstable state has no distinct resonances, the Landau-Zener prediction for the lifetime is a good approximation.

6.5 Non-exponential decay

An exponential decay law is the universal hallmark of unstable systems and is observed in all fields of science. This law is not, however, fully consistent with quantum mechanics and deviations from exponential decay have been predicted for short as well as long times [72, 73, 74]. In 1957, Khalfin showed, given that H has a spectrum bounded from below, that the survival probability is not a pure exponential but rather of the form

$$\lim_{t \rightarrow \infty} P(t) \approx \exp(-ct^q) \quad q < 1, c > 0. \quad (6.25)$$

Then, in 1961, Winter showed that, for a simple barrier-penetration problem, the survival probability begins with a non-exponential, oscillatory behavior, evolves into an exponential, begins oscillating again so that there are recurrences, and then finally decays like an inverse power of the time [73]. This effect is related to the fact that the coupling between the decaying system and the reservoir is reversible for short enough times and the population transfer begins with a quadratic time dependence. Moreover, for these short times, the decayed and undecayed states are not yet resolvable, even in principle.

Perhaps the simplest demonstration that $P(t)$ is not strictly an exponential is for the case of short times. Given that the mean energy of the decaying state is finite, one can show that

$$\left. \frac{dP(t)}{dt} \right|_{t \rightarrow 0} = 0. \quad (6.26)$$

Therefore we will show, following Fonda, that the decay for small times is less than any exponential function [74]. To show this property, we will first define the survival probability P . We assume that the system is initially in the undecayed state $|\Psi_0\rangle$ at $t = 0$, and that the state evolves under the action of the Hamiltonian H ,

$$|\Psi(t)\rangle = e^{-i\hat{H}t}|\Psi_0\rangle, \quad (6.27)$$

so that the probability amplitude for being in the undecayed state at time t is

$$A(t) = \langle \Psi_0 | e^{-i\hat{H}t} | \Psi_0 \rangle, \quad (6.28)$$

and the survival probability is just

$$P(t) = |A(t)|^2. \quad (6.29)$$

Now, we consider a complete set of commuting observables denoted by (H, α) and common eigenstates $|\phi_{E,a}\rangle$ with discrete and/or continuous spectra. The completeness relation is

$$\int dE da |\phi_{E,a}\rangle \langle \phi_{E,a}| = \mathbf{I}, \quad (6.30)$$

and we can expand our state in terms of this basis set. Doing so, we have

$$A(t) = \int dE \omega(E) e^{-iEt}, \quad (6.31)$$

where

$$\omega(E) = \int da |\langle \phi_{E,a} | \Psi_0 \rangle|^2. \quad (6.32)$$

Now, we make the assumption that H has a spectrum that is bounded from below. This assumption is reasonable and necessary for a physical system. This allows us to place a limit on the integration in Eq. (6.31). We have now that

$$A(t) = \int_{E_{\min}}^{\infty} dE \omega(E) e^{-iEt}, \quad (6.33)$$

and moreover that Ψ is normalizable,

$$\begin{aligned} \int_{E_{\min}}^{\infty} dE \omega(E) &= \int_{E_{\min}}^{\infty} dE da |\langle \Psi | \phi_{E,a} \rangle \langle \phi_{E,a} | \Psi \rangle|^2 \\ &= \langle \Psi | \mathbf{I} | \Psi \rangle = 1. \end{aligned} \quad (6.34)$$

Since we have from Eq. (6.34) that

$$\int_{E_{\min}}^{\infty} dE |\omega(E)| < \infty, \quad (6.35)$$

the integral defining $A(t)$, Eq. (6.31), is uniformly convergent and therefore $A(t)$ is everywhere continuous. Since $\omega(E)$ is real, A has the additional property that

$$A^*(t) = A(-t). \quad (6.36)$$

Now, we make the second assumption that the mean energy in the state $|\Psi\rangle$ is finite:

$$\langle E \rangle = \langle \Psi | H | \Psi \rangle = \int dE \omega(E) E < \infty. \quad (6.37)$$

This assumption implies that the derivative of A is well defined and is continuous everywhere, since

$$\frac{dA(t)}{dt} = -i \int dE \omega(E) E e^{-iEt}. \quad (6.38)$$

Using Eq. (6.36), the survival probability can be rewritten as

$$P(t) = A^*(t)A(t) = A(-t)A(t). \quad (6.39)$$

Taking the derivative, we have, using the chain rule,

$$\frac{dP(t)}{dt} = \frac{dA(-t)}{dt}A(t) + A(-t)\frac{dA(t)}{dt}, \quad (6.40)$$

and since both A and its derivative are continuous we have immediately that

$$\left. \frac{dP(t)}{dt} \right|_{t=0^+} = 0. \quad (6.41)$$

This result is a general property independent of the details of the interaction. However, the time scale over which this deviation is apparent depends on the particular time scales of the decaying system. There are a number of time scales which seem relevant. The first time scale τ_e is given by the time that decay products take to leave the bound state region. This dynamical time scale is related to the characteristic motion within the bound state and determines the amount of time required to pass before the decayed and undecayed states

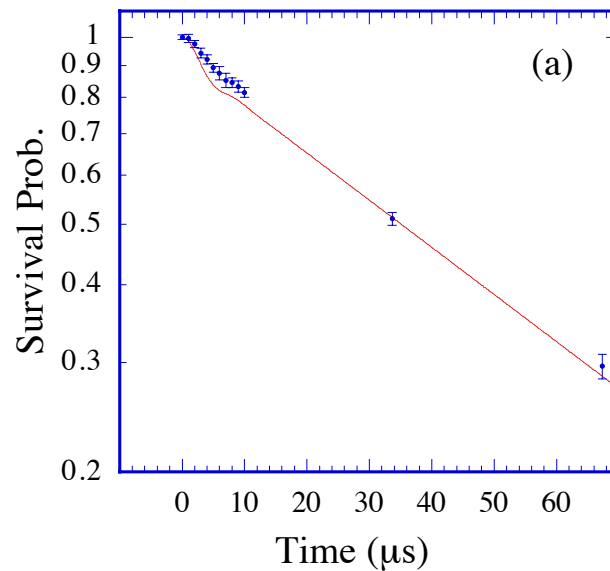


Figure 6.8: Survival probability as a function of duration of the acceleration a_{tunnel} . The solid line is the theoretical prediction. For these data the acceleration was 7000 m/s^2 , and the well depth was $V_0 = 0.425 \pm 10\%$. The theoretical calculation used the same acceleration, but the potential was taken as $V_0 = 0.37$.

can be resolved. The second time scale is related to the ΔE bandwidth of the continuum to which the state is coupled. Essentially $\tau_m = \hbar/\Delta E$ is the time over which the total decayed state contribution to the reformation of the undecayed state is no longer in phase. After this dephasing time, the coupling is essentially irreversible.

Although these predictions were made almost 40 years ago, no such deviations have hitherto been observed experimentally. The primary reason is that these characteristic time scales in most naturally occurring systems are extremely short. For the decay of a spontaneous photon, the time it takes a photon to traverse the bound state size is approximately an optical period, 10^{-15} s . For a nuclear decay this time scale is orders of magnitude shorter, about 10^{-21} s . By contrast, the dynamical time scale for an atom bound in

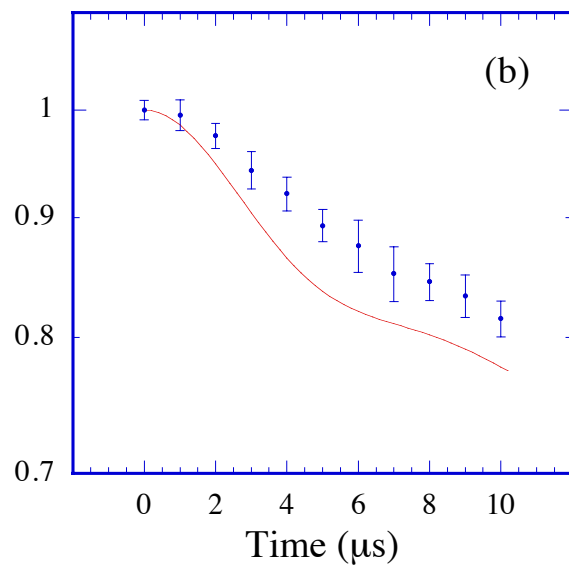


Figure 6.9: Survival probability as a function of duration of the acceleration a_{tunnel} . The solid line is the theoretical prediction. For these data the acceleration was 7000 m/s^2 , and the well depth was $V_0 = 0.425 \pm 10\%$. The theoretical calculation used the same acceleration, but the potential was taken as $V_0 = 0.37$.

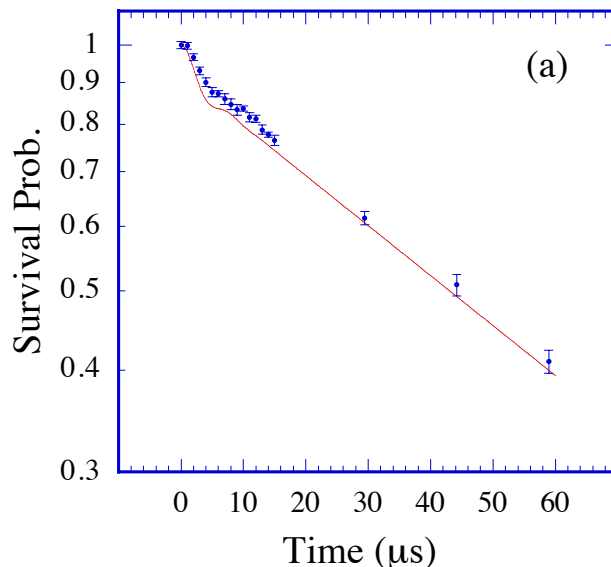


Figure 6.10: Survival probability as a function of duration of the acceleration a_{tunnel} . The solid line is the theoretical prediction. For these data the acceleration was 9000 m/s^2 , and the well depth was $V_0 = 0.45 \pm 10\%$. The theoretical calculation used the same acceleration, but the potential was taken as $V_0 = 0.46$.

an optical lattice is just the inverse band gap energy, which for a well depth of 0.4 is $12 \mu\text{s}$. The corresponding classical harmonic oscillator frequency for this well depth is 126 kHz with a period of $7.9 \mu\text{s}$.

In Figs. 6.8-6.11, the survival probability is plotted as a function of the duration of the tunneling acceleration. A plot of the optical lattice velocity profile for this experiment is provided in Fig. 2.13. In order to claim that we were observing the generic signature predicted by Eq. (6.41), we had to know that the horizontal axis was a true measure of the duration of the large acceleration a_{tunnel} . For this, we characterized the response of the AOM driver and found that the switching time between accelerations was 220 ns (see Chapter 2). Data were taken at intervals of $1 \mu\text{s}$ for the first $15 \mu\text{s}$ to obtain the highest resolution in short time. The long-time exponential behavior was

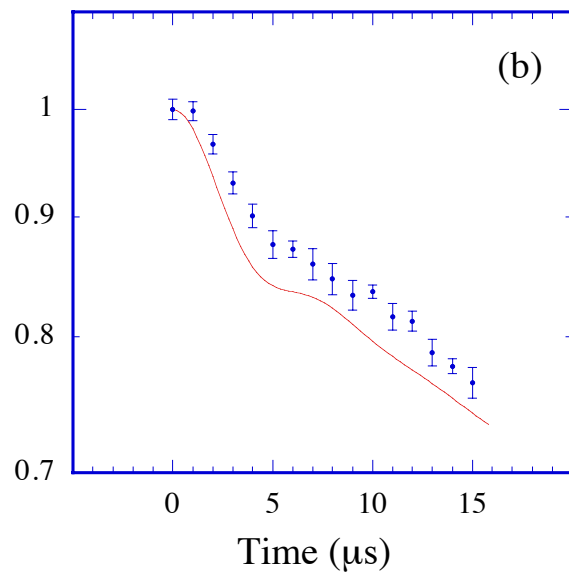


Figure 6.11: Survival probability as a function of duration of the acceleration a_{tunnel} . The solid line is the theoretical prediction. For these data the acceleration was 9000 m/s^2 , and the well depth was $V_0 = 0.45 \pm 10\%$. The theoretical calculation used the same acceleration, but the potential was taken as $V_0 = 0.46$.

extensively tested in earlier work [3], and the data shown here for times longer than $15 \mu\text{s}$ establish the exponents. Figures 6.9 and 6.11 show expanded-scale views of the short-time behavior. The focus of our attention is on time scales shorter than $15 \mu\text{s}$. The initial survival probability is flat, with a quadratic time dependence, owing to a reversible coupling to the bath. The intermediate stage is characterized by a damped oscillation. After $10 \mu\text{s}$ the coupling is irreversible and exponential decay sets in.

By considering a two-band model of this problem, it was shown by Niu and Raizen [75] that the oscillations occur at a frequency corresponding to the band gap and that they are damped out after a crossover time (expressed in scaled units) equal to

$$t_c = \frac{\epsilon_g}{a}. \quad (6.42)$$

This result for the crossover time from non-exponential to exponential decay is the same as the *tunneling time* for Zener breakdown found by Büttiker and Landauer [76].

After observing short-time deviations from exponential decay, we investigated the possibility of suppressing tunneling by repeated measurements during the non-exponential time. This phenomenon, known as the Quantum Zeno effect, was first predicted by Misra and Sudarshan, who argued that an unstable particle that is continuously observed will never be found to decay since each observation causes a collapse of the wave function back to the undecayed state [77]. Our hope was to simply suppress tunneling by making measurements on the first band population every microsecond before it had time to begin decaying exponentially and before the first dip from the oscillation. The measurement process to “reset the clock” back to $t = 0$ was the same process used to initially prepare the atoms. A low transport acceleration was imposed for which the tunneling rate out of the first band was negligible but the rate out of the higher bands was large. In this way, the unstable state

was separated from the decay products in velocity space, and the large acceleration could be imposed again, producing no losses for another microsecond. We performed several experiments, choosing the interruption acceleration and duration to separate the lowest band from the higher bands by several double photon recoils (or several Brillouin zones). The interruption produced a revival of the non-exponential behavior as expected, but the losses incurred by the measurement process, albeit small, were larger than those for the tunneling process. For this reason, we could not “break even” on losses, much less suppress them. Technical problems associated with the interferometric stability of the standing wave and problems associated with the finite resolution of our electronic drivers prevented us from achieving longer non-exponential times by reducing the well depth and the acceleration. This strategy, of reducing the acceleration and well depth, would also allow a greater flexibility in the study of the tunneling time [75].

Appendix

Appendix A

Unitary Transformations

A.1 The action of a unitary transformation on the Hamiltonian

Given some Hermitian operator A , we can define a unitary operator U such that

$$U = e^{iA}. \quad (\text{A.1})$$

A general state vector $|\psi\rangle$ will transform under U by the relation

$$|\tilde{\psi}\rangle = U|\psi\rangle, \quad (\text{A.2})$$

and a general operator B by the relation

$$\tilde{B} = UBU^\dagger. \quad (\text{A.3})$$

Unitary transformations preserve both the length of inner products between state vectors $\langle\tilde{\psi}_1|\tilde{\psi}_2\rangle = \langle\psi_1|\psi_2\rangle$ as well as the expectation values of time-independent operators $\langle\tilde{\psi}_1|\tilde{B}|\tilde{\psi}_2\rangle = \langle\psi_1|B|\psi_2\rangle$. However, not all unitary transformations will preserve the energy of the system, and therefore the Hamiltonian will not transform exactly according to Eq. (A.3). In order to deduce the correct form for the new Hamiltonian we require that the dynamics be unaffected by U . The untransformed Schrödinger equation is

$$i\hbar\frac{\partial}{\partial t}|\psi\rangle = H|\psi\rangle. \quad (\text{A.4})$$

Using Eq. (A.2) we can rewrite this as

$$i\hbar \frac{\partial}{\partial t} (U^\dagger |\tilde{\psi}\rangle) = H (U^\dagger |\tilde{\psi}\rangle). \quad (\text{A.5})$$

Differentiating, left multiplying by U and rearranging the terms gives

$$i\hbar \frac{\partial}{\partial t} |\tilde{\psi}\rangle = \left(U H U^\dagger - i\hbar U \frac{\partial U^\dagger}{\partial t} \right) |\tilde{\psi}\rangle. \quad (\text{A.6})$$

We identify the term in parenthesis as the new Hamiltonian governing the transformed state vector. Using one more relation,

$$\frac{\partial}{\partial t} (U U^\dagger) = 0 = \frac{\partial U}{\partial t} U^\dagger + U \frac{\partial U^\dagger}{\partial t}, \quad (\text{A.7})$$

we can write the transformed Hamiltonian \tilde{H} as

$$\boxed{\tilde{H} = U H U^\dagger + i\hbar U \frac{\partial U^\dagger}{\partial t}}. \quad (\text{A.8})$$

A.2 A general one-dimensional coordinate transformation

By varying the frequency difference $\Delta\omega$ between the two traveling-wave components of our standing wave, the position of the potential can be controlled in an arbitrary way. If $2k_L\alpha(t)$ is the total accumulated phase difference between the two components,

$$\alpha(t) = \frac{1}{2k_L} \int_0^t \Delta\omega(\tau) d\tau \quad (\text{A.9})$$

then the classical Hamiltonian in the lab frame has the following form:

$$H(x, p, t) = \frac{p^2}{2M} + V_0 \cos(2k_L [x - \alpha(t)]). \quad (\text{A.10})$$

Following the recipe outlined by Peik [37], we apply a unitary transformation that performs a translation of the position, momentum, and overall energy:

$$U(t) = e^{i\alpha(t)p/\hbar} e^{-i\beta(t)x/\hbar} e^{i\gamma(t)/\hbar}. \quad (\text{A.11})$$

U 's action on x and p is

$$U(t)xU^\dagger(t) = e^{i\alpha(t)p/\hbar}xe^{-i\alpha(t)p/\hbar} \quad (\text{A.12})$$

$$= x + \alpha(t) \quad (\text{A.13})$$

$$U(t)pU^\dagger(t) = e^{-i\beta(t)x/\hbar}pe^{i\beta(t)x/\hbar} \quad (\text{A.14})$$

$$= p + \beta(t). \quad (\text{A.15})$$

This can be verified using the relation

$$e^A B e^{-A} = B + [A, B] + \frac{1}{2!} [A, [A, B]] + \frac{1}{3!} [A, [A, [A, B]]] + \dots \quad (\text{A.16})$$

and the following commutation relations

$$[p, f(x)] = -i\hbar \frac{\partial f}{\partial x} \quad (\text{A.17})$$

$$[x, f(p)] = i\hbar \frac{\partial f}{\partial p}. \quad (\text{A.18})$$

Because the Hamiltonian is a function composed of algebraic operations involving c-numbers, x and p and contains no constant matrices, we see that

$$UH(x, p, t)U^\dagger = H(UxU^\dagger, UpU^\dagger, UtU^\dagger) \quad (\text{A.19})$$

To obtain the transformed Hamiltonian from Eq. (A.8) we need to compute the final term. Being careful with the order of noncommuting terms, we find that

$$i\hbar \frac{\partial U(t)}{\partial t} U^\dagger(t) = -\dot{\alpha}p + \dot{\beta}U(t)xU^\dagger(t) - \dot{\gamma} \quad (\text{A.20})$$

$$= -\dot{\alpha}p + \dot{\beta}(x + \alpha) - \dot{\gamma}. \quad (\text{A.21})$$

We now use our freedom to choose γ to tidy up the transformation of the Hamiltonian by absorbing all terms that are only time dependent. Shifting the overall energy in this way is an operation that does not affect the dynamics.

With $\dot{\gamma}$ given by

$$\dot{\gamma} = \frac{\beta^2}{2M} + \dot{\beta}\alpha, \quad (\text{A.22})$$

and using Eq. (A.8), the Hamiltonian of Eq. (A.10) becomes

$$H(x, p, t) = \frac{p^2}{2M} + V_0 \cos(2k_L x) + x\dot{\beta} + p \left(\frac{\beta}{M} - \dot{\alpha} \right) \quad (\text{A.23})$$

Now, we are free to choose β as we like. If we let

$$\beta = M\dot{\alpha}, \quad (\text{A.24})$$

then we are left with

$$H(x, p, t) = \frac{p^2}{2M} + V_0 \cos(2k_L x) + xaM \quad (\text{A.25})$$

where we identify the acceleration $a = \ddot{\alpha}$. If, on the other hand, we choose $\beta = 0$, then we get

$$H(x, p, t) = \frac{(p - Mv)^2}{2M} + V_0 \cos(2k_L x) \quad (\text{A.26})$$

where we have identified the instantaneous velocity $v = \dot{\alpha}$. We note here that these last two Hamiltonians are analogous to the pair related by a gauge transformation of the electromagnetic field for the case of an electron.

A.3 Canonical Transformations

In this section, the equivalent (classical) canonical transformation to the general unitary transformation detailed in Section A.1 is shown.

A.3.1 Transformation for a general time dependent phase: from lab frame to potential frame

By varying the frequency difference $\Delta\omega$ between the two traveling-wave components of our standing wave, the position of the potential can be controlled in an arbitrary way. If $2k_{\text{L}}f(t)$ is the total accumulated phase difference between the two components,

$$f(t) = \frac{1}{2k_{\text{L}}} \int_0^t \Delta\omega(\tau) d\tau \quad (\text{A.27})$$

then the classical Hamiltonian in the lab frame has the following form:

$$H(x, p, t) = \frac{p^2}{2M} + V_0 \cos\left(2k_{\text{L}}[x + f(t)]\right). \quad (\text{A.28})$$

Our new coordinates, x' and p' , in the time dependent frame are

$$x' = x + f(t) \quad (\text{A.29})$$

$$p' = M \frac{dx'}{dt} = p + M \frac{df}{dt}. \quad (\text{A.30})$$

Following the recipe detailed by Goldstein [78], we seek a new Hamiltonian, H' that is a function of x' and p' and that must satisfy Hamilton's principle if x' and p' are to be canonical coordinates. For the old coordinates in the lab frame we had,

$$\delta \int_{t_1}^{t_2} (p\dot{x} - H(p, x, t)) dt = 0, \quad (\text{A.31})$$

and for the new set we have,

$$\delta \int_{t_1}^{t_2} (p'\dot{x}' - H'(p', x', t)) dt = 0. \quad (\text{A.32})$$

This condition results in a relation between the integrands,

$$p\dot{x} - H = p'\dot{x}' - H' + \frac{dF}{dt}, \quad (\text{A.33})$$

where F , the *generating function*, specifies the form of the transformation.

Now, we let

$$F = F_2(x, p', t) - x'p'. \quad (\text{A.34})$$

Substituting (A.34) into (A.33) we get after some algebra

$$p\dot{x} - H = -\dot{p}'x' - H' + \frac{\partial F_2}{\partial t} + \frac{\partial F_2}{\partial x}\dot{x} + \frac{\partial F_2}{\partial p'}\dot{p}'. \quad (\text{A.35})$$

Since x and p' are independent their coefficients must each vanish. As a result, the new Hamiltonian is related to the original one by

$$H' = H + \frac{\partial F_2}{\partial t}, \quad (\text{A.36})$$

and we have the following relations for F_2

$$p = \frac{\partial F_2}{\partial x} \quad (\text{A.37})$$

$$x' = \frac{\partial F_2}{\partial p'}. \quad (\text{A.38})$$

After rewriting these two expressions in terms of x and p' , we can determine $F_2(x, p', t)$ up to some function only of time, $g(t)$, to be determined shortly.

We have then

$$F_2(x, p', t) = p'x - Mx\frac{df}{dt} + p'f(t) + g(t), \quad (\text{A.39})$$

and therefore we obtain

$$\frac{\partial F_2}{\partial t} = -Mx\frac{d^2f}{dt^2} + p'\frac{df}{dt} + \frac{dg}{dt}. \quad (\text{A.40})$$

Since f and g are functions only of time, the partial derivative with respect to time is equivalent to a full derivative. Substituting (A.40) into (A.36) and writing everything in terms of the new coordinates, x' and p' , we get

$$H'(x', p', t) = \frac{p'^2}{2M} + V_0 \cos(2k_L x') - Mx'\frac{d^2f}{dt^2} + \frac{dg}{dt} + Mf(t)\frac{d^2f}{dt^2} + \frac{M}{2}\left(\frac{df}{dt}\right)^2. \quad (\text{A.41})$$

We choose $g(t)$ so that the last three terms, which depend only on t , vanish.

This leaves us with

$$\boxed{H'(x', p', t) = \frac{p'^2}{2M} + V_0 \cos(2k_L x') - Mx' \frac{d^2 f}{dt^2}} \quad (\text{A.42})$$

and

$$\boxed{\frac{dg}{dt} = - \left[Mf(t) \frac{d^2 f}{dt^2} + \frac{M}{2} \left(\frac{df}{dt} \right)^2 \right]} \quad (\text{A.43})$$

A.3.2 Example I: An accelerating and modulating phase

The potential used to study Wannier Stark ladders is realized by quadratically ramping the phase in time while simultaneously modulating it weakly to probe the ladder states. The potential in the lab frame is of the form

$$V_0 \cos \left[2k_L \left(x + v_0 t + \frac{at^2}{2} \right) + \lambda \sin \omega_p t \right], \quad (\text{A.44})$$

where v_0 is the velocity, a is the acceleration of the standing-wave, and λ is the modulation modulation index of the weak probe. The function $f(t)$ of Equation (A.29) and its derivatives are

$$f(t) = v_0 t + \frac{at^2}{2} + \frac{\lambda}{2k_L} \sin \omega_p t \quad (\text{A.45})$$

$$f'(t) = v_0 + at + \frac{\lambda \omega_p}{2k_L} \cos \omega_p t \quad (\text{A.46})$$

$$f''(t) = a - \frac{\lambda \omega_p^2}{2k_L} \sin \omega_p t. \quad (\text{A.47})$$

The Hamiltonian in the potential's reference frame is

$$H'(x', p', t) = \frac{p'^2}{2M} + V_0 \cos(2k_L x') - Max' + \frac{M\lambda\omega_p^2}{2k_L} x' \sin \omega_p t. \quad (\text{A.48})$$

We see then that the acceleration produces an inertial term that acts like a static, homogeneous electric field, and the phase modulation produces a term that is equivalent to a dipole coupled to an external AC field.

Bibliography

- [1] J. C. Robinson, C. F. Bharucha, K. W. Madison, F. L. Moore, Bala Sundaram, S. R. Wilkinson, and M. G. Raizen, “Can a single-pulse standing wave induce chaos in atomic motion?” *Phys. Rev. Lett.* **76**, 3304 (1996).
- [2] S. R. Wilkinson, C. F. Bharucha, K. W. Madison, Qian Niu, and M. G. Raizen, “Observation of atomic Wannier-Stark ladders in an accelerating optical potential,” *Phys. Rev. Lett.* **76**, 4512 (1996).
- [3] C. F. Bharucha, K. W. Madison, P. R. Morrow, S. R. Wilkinson, Bala Sundaram, and M. G. Raizen, “Observation of atomic tunneling from an accelerating optical potential,” *Phys. Rev. A* **55**, R857 (1997).
- [4] S. R. Wilkinson, C. F. Bharucha, M. C. Fischer, K. W. Madison, P. R. Morrow, Qian Niu, Bala Sundaram, and M. G. Raizen, “Experimental evidence for non-exponential decay in quantum tunneling,” *Nature* **387**, 575 (June 1997).
- [5] M. C. Fischer, K. W. Madison, Qian Niu, and M. G. Raizen, “Observation of Rabi oscillations between Bloch bands in an optical potential,” *Phys. Rev. A Rapid Commun., in press* (1998).
- [6] K. W. Madison, M. C. Fischer, R. B. Diener, Qian Niu, and Mark G. Raizen, “Dynamical Bloch band suppression in an optical lattice,” *submitted to Phys. Rev. Lett.* (1998).

- [7] Claude Cohen-Tannoudji, Jacques Dupont-Roc, and Gilbert Grynberg, *Atom-Photon Interactions* (Wiley and Sons, New York, 1992).
- [8] R. Graham, M. Schlautmann, and P. Zoller, “Dynamical localization of atomic-beam deflection by a modulated standing light-wave,” *Phys. Rev. A* **45**, R19 (1992).
- [9] Pierre Meystre and Murray Sargent III, *Elements of Quantum Optics* (Springer-Verlag, Berlin, 1991), 2nd ed.
- [10] Peter W. Milonni and Joseph H. Eberly, *Lasers* (Wiley and Sons, New York, 1988).
- [11] Felix Bloch, “Über die Quantenmechanik der Elektronen in Kristallgittern,” *Z. Phys.* **52**, 555 (1928).
- [12] W. V. Houston, “Acceleration of electrons in a crystal lattice,” *Phys. Rev.* **57**, 184 (1940).
- [13] H. Jones and C. Zener, “A general proof of certain fundamental equations in the theory of metallic conduction,” *Proc. R. Soc. London A* **144**, 101 (1934).
- [14] Gregory H. Wannier, “Wave functions and effective hamiltonian for Bloch electrons in an electric field,” *Phys. Rev.* **117**, 432–655 (1960).
- [15] Clarence Zener, “Non-adiabatic crossing of energy levels,” *Proc. R. Soc. London A* **137**, 696 (1932).
- [16] C. Zener, “A theory of the electrical breakdown of solid dielectrics,” *Proc. R. Soc. London A* **145**, 523 (1934).

- [17] Robert W. Koss and L. M. Lambert, “Experimental observation of Wannier levels in semi-insulating Gallium Arsenide,” *Phys. Rev. B* **5**, 1479 (1972).
- [18] E. E. Mendez, F. Agulló-Rueda, and J. M. Hong, “Stark localization in GaAs-GaAlAs superlattices under an electric field,” *Phys. Rev. Lett.* **60**, 2426 (1988).
- [19] Emilio E. Mendez and Gérald Bastard, “Wannier-Stark ladders and Bloch oscillations in superlattices,” *Physics Today*, June 1993, p. 34.
- [20] P. Voisin, J. Bleuse, C. Bouche, S. Gaillard, C. Alibert, and A. Regreny, “Observation of the Wannier-Stark quantization in a semiconductor superlattice,” *Phys. Rev. Lett.* **61**, 1639 (1988).
- [21] Steven Chu, “Laser manipulation of atoms and particles,” *Science* **253**, 861 (1991).
- [22] Maxime Ben Dahan, Ekkehard Peik, Jakob Reichel, Yvan Castin, and Christophe Salomon, “Bloch oscillations of atoms in an optical potential,” *Phys. Rev. Lett.* **76**, 4508 (1996).
- [23] K. W. Madison, C. F. Bharucha, P. R. Morrow, S. R. Wilkinson, Qian Niu, Bala Sundaram, and M. G. Raizen, “Quantum transport of ultracold atoms in an accelerating optical potential,” *Appl. Phys. B* **65**, 693 (1997).
- [24] M. G. Raizen, Christophe Salomon, and Qian Niu, “New light on quantum transport,” *Physics Today*, July 1997, p. 30.
- [25] G. Raithel, G. Birkl, A. Kastberg, W. D. Phillips, and S. L. Rolston, “Cooling and localization dynamics in optical lattices,” *Phys. Rev. Lett.* **78**, 630 (1997).

- [26] G. Raithel, G. Birkl, W. D. Phillips, and S. L. Rolston, “Compression and parametric driving of atoms in optical lattices,” *Phys. Rev. Lett.* **78**, 2928 (1997).
- [27] Qian Niu, “Quantized density response in insulators,” *Phys. Rev. B* **49**, 13554 (1994).
- [28] Jing-Tzyh Alan Chiang and Qian Niu, “Quantum adiabatic particle transport in optical lattices,” *Phys. Rev. A* **57**, R2278 (1998).
- [29] K. Drese and M. Holthaus, “Ultracold atoms in modulated standing light waves,” *Journal of Chemical Physics* **217**, 201 (1997).
- [30] Georgios Andreas Georgakis, *Exploring Condensed Matter Problems Using Optical Lattices*, Ph.D. thesis, The University of Texas at Austin (1996).
- [31] E. Raab, M. Prentiss, A. Cable, S. Chu, and D. Pritchard, “Trapping of neutral sodium atoms with radiation pressure,” *Phys. Rev. Lett.* **59**, 2631 (1987).
- [32] Daniel A. Steck, “Cesium D_2 line data,” (August 1998). Unpublished.
- [33] P. D. Lett, W. D. Phillips, S. L. Rolston, C. E. Tanner, R. N. Watts, and C. I. Westbrook, “Optical molasses,” *J. Opt. Soc. Am. B* **6**, 2084 (1989).
- [34] Martin Christian Fischer, *Design and Performance of a Ring Dye Laser*, Master’s thesis, The University of Texas at Austin (1993).
- [35] T. W. Hänsch and B. Couillaud, “Laser frequency stabilization by polarization spectroscopy of a reflecting reference cavity,” *Optics Comm.* **35**, 441 (1980).

- [36] Rodney Loudon, *The quantum theory of light* (Clarendon, Oxford, 1983), 2nd ed.
- [37] Ekkehard Peik, Maxime Ben Dahan, Isabelle Bouchoule, Yvan Castin, and Christophe Salomon, “Bloch oscillations of atoms, adiabatic rapid passage and monokinetic atomic beams,” *Phys. Rev. A* **55**, 2989 (1997).
- [38] J.-Y. Courtois, G. Grynberg, B. Lounis, and P. Verkerk, “Recoil-induced resonances in cesium: An atomic analog to the free-electron laser,” *Phys. Rev. Lett.* **72**, 3017 (1994).
- [39] Cyrus Bharucha, *Numerical simulation of a two-level atom in a modulated standing wave*, Master’s thesis, The University of Texas at Austin (1994).
- [40] John Charles Robinson, *Atom Optics: A New Testing Ground for Quantum Chaos*, Ph.D. thesis, The University of Texas at Austin (1995).
- [41] Cyrus Farrokh Bharucha, *Experiments in Dynamical Localization of Ultra-Cold Sodium Atoms Using Time-Dependent Optical Potentials*, Ph.D. thesis, The University of Texas at Austin (1997).
- [42] M. G. Raizen, F. L. Moore, J. C. Robinson, C. F. Bharucha, and Bala Sundaram, “An experimental realization of the quantum δ -kicked rotor,” *Quantum Semiclass. Opt.* **8**, 687–692 (1996).
- [43] Milton Abramowitz and Irene A. Stegun, eds., *Handbook of Mathematical Functions* (Dover, New York, 1965).
- [44] Stephen Wolfram, *Mathematica* (Wolfram Research, 1994).
- [45] F. L. Moore, J. C. Robinson, C. Bharucha, Bala Sundaram, and M. G. Raizen, “Atom optics realization of the quantum δ -kicked rotor,” *Phys. Rev. Lett.* **75**, 4598 (1995).

- [46] E. T. Whittaker and G. N. Watson, *A course of Modern Analysis* (Cambridge University Press, New York, 1927), 4th ed.
- [47] Neil W. Ashcroft and N. David Mermin, *Solid State Physics* (Saunders College, Philadelphia, 1976).
- [48] Eugen Merzbacher, *Quantum Mechanics* (John Wiley and Sons, New York, 1970), 2nd ed.
- [49] A. Görlitz, M. Weidemüller, T. W. Hänsch, and A. Hemmerich, “Observing the position spread of atomic wave packets,” *Phys. Rev. Lett.* **78**, 2096 (1997).
- [50] G. H. Wannier, “Dynamics of band electrons in electric and magnetic fields,” *Reviews of Modern Physics* **34**, 645–655 (1962).
- [51] Peter John Martin, *Momentum transfer to atoms moving through a standing wave of light*, Ph.D. thesis, Massachusetts Institute of Technology (1987).
- [52] David M. Giltner, Roger W. McGowan, and Siu Au Lee, “Atom interferometer based on Bragg scattering from standing light waves,” *Phys. Rev. Lett.* **75**, 2638 (1995).
- [53] F. L. Moore, J. C. Robinson, C. Bharucha, P. E. Williams, and M. G. Raizen, “Observation of dynamical localization in atomic momentum transfer: A new testing ground for quantum chaos,” *Phys. Rev. Lett.* **73**, 2974 (1994).
- [54] J. C. Robinson, C. Bharucha, F. L. Moore, R. Jahnke, G. A. Georgakis, Q. Niu, M. G. Raizen, and Bala Sundaram, “Study of quantum dynamics in the transition from classical stability to chaos,” *Phys. Rev. Lett.* **74**, 3963 (1995).

- [55] Graham P. Collins, “Sodium atoms kicked by standing waves provide a new probe of quantum chaos,” *Physics Today*, June 1995, pp. 18–21.
- [56] Bruce G. Klappauf, Windell H. Oskay, Daniel A. Steck, and Mark G. Raizen, “Observation of noise and dissipation effects on dynamical localization,” *Phys. Rev. Lett.* **81**, 1203 (1998).
- [57] M. Wilkens, E. Schumacher, and P. Meystre, “Band theory of a common model of atom optics,” *Phys. Rev. A* **44**, 3130 (1991).
- [58] Xian-Geng Zhao, G. A. Georgakis, and Qian Niu, “Rabi oscillations between Bloch bands,” *Phys. Rev. B* **54**, R5235 (1996).
- [59] D. H. Dunlap and V. M. Kenkre, “Dynamic localization of a charged particle moving under the influence of an electric field,” *Phys. Rev. B* **34**, 3625 (1986).
- [60] Martin Holthaus, “Collapse of minibands in far-infrared irradiated superlattices,” *Phys. Rev. Lett.* **69**, 351 (1992).
- [61] X.-G. Zhao, “The suppression of a Bloch band in a driving laser field,” *Journal of Physics* **6**, 2751 (1994).
- [62] K. Unterrainer, B. J. Keay, M. C. Wanke, S. J. Allen, D. Leonard, G. Medeiros-Ribeiro, U. Bhattacharya, and M. J. W. Rodwell, “Inverse Bloch oscillator: strong terahertz-photocurrent resonances at the Bloch frequency,” *Phys. Rev. Lett.* **76**, 2973 (1996).
- [63] A. A. Ignatov, E. Schomburg, K. F. Renk, W. Schatz, J. F. Palmier, and F. Molloy, “Response of a Bloch oscillator to a Thz-field,” *Ann. Physik* **3**, 137 (1994).

- [64] B. J. Keay, S. Zeuner, S. J. Allen, Jr, K. D. Maranowski, A. C. Gossard, U. Bhattacharya, and M. J. W. Rodwell, “Dynamic localization, absolute negative conductance, and stimulated, multiphoton emission in sequential resonant tunneling semiconductor superlattices,” *Phys. Rev. Lett.* **75**, 4102 (1995).
- [65] Albert Messiah, *Quantum Mechanics* (North-Holland, Amsterdam, 1962).
- [66] J. B. Krieger and G. J. Iafrate, “Time evolution of Bloch electrons in a homogeneous electric field,” *Phys. Rev. B* **33**, 5494 (1986).
- [67] Eugene Hecht, *Optics* (Addison-Wesley, Reading, 1998), 3rd ed.
- [68] Qian Niu, Xian-Geng Zhao, G. A. Georgakis, and M. G. Raizen, “Atomic Landau-Zener tunneling and Wannier-Stark ladders in optical potentials,” *Phys. Rev. Lett.* **76**, 4504 (1996).
- [69] Ernst M. Rasel, Markus K. Oberthaler, Herman Batelaan, Jörg Schmiedmayer, and Anton Zeilinger, “Atom wave interferometry with diffraction gratings of light,” *Phys. Rev. Lett.* **75**, 2633 (1995).
- [70] Alan Lenef, Troy D. Hammond, Edward T. Smith, Michael S. Chapman, Richard A. Rubenstein, and David E. Pritchard, “Rotation sensing with an atom interferometer,” *Phys. Rev. Lett.* **78**, 760 (1997).
- [71] Qian Niu. Private communication.
- [72] L. A. Khalfin, “Contribution to the decay theory of a quasi-stationary state,” *JETP* **6**, 1053 (1958).
- [73] R. G. Winter, “Evolution of a quasi-stationary state,” *Phys. Rev.* **123**, 1503 (1961).

- [74] L. Fonda, G. C. Ghirardi, and G. C. Rimini, “A decay theory of unstable quantum systems,” *Rep. Prog. Phys.* **41**, 587 (1978).
- [75] Qian Niu and M. G. Raizen, “How Landau-Zener tunneling takes time,” *Phys. Rev. Lett.* **80**, 3491 (1998).
- [76] Markus Büttiker and Rolf Landauer, “Traversal time for tunneling,” *Festkörperprobleme* **25**, 711 (1985).
- [77] B. Misra and E. C. G. Sudarshan, “The Zeno’s paradox in quantum theory,” *J. Math. Phys.* **18**, 756 (1977).
- [78] Herbert Goldstein, *Classical Mechanics* (Addison-Wesley, Reading, 1980), 2nd ed.

Vita

Kirk William Madison was born on October 28, 1969 to Mitzi and Ralph Madison in Dallas, Texas. After graduating from St. Martin's Episcopal School in Metairie, Louisiana, Kirk earned his Bachelor's degree in Electrical Engineering and Physics at Tulane University in 1992. In the summer of 1994, Kirk joined the research group of Mark G. Raizen at the University of Texas at Austin, and in the summer of 1995 began working on the study of quantum transport in optical lattices, presented here.

Permanent address: 1201 Park St. North
St. Petersburg, FL 33710
U.S.A.

This dissertation was typeset with \LaTeX^\ddagger by the author.

[‡] \LaTeX is a document preparation system developed by Leslie Lamport as a special version of Donald Knuth's \TeX Program.